Theoretical Optical Spectroscopy of Polynuclear Transition Metal and Lanthanoid Complexes

Zur Erlangung des akademischen Grades eines

DOKTORS DER NATURWISSENSCHAFTEN

(Dr. rer. nat.)

von der Fakultät für Chemie und Biowissenschaften

des Karlsruher Instituts für Technologie (KIT)

genehmigte

DISSERTATION

von

Jiří Chmela, M. Sc.

aus

Ostrava, Tschechien

KIT-Dekan:	Prof. Dr. W. Klopper
Referent:	Prof. Dr. W. Klopper
Korreferent:	PD Dr. F. Weigend

Tag der mündlichen Prüfung: 16. Dezember 2016

Contents

1. Introduction

Compounds that contain metal centers are chemically important for their properties that can be used in catalysis or in optical devices.[1–5] Many different experimental techniques can be used to study the optical and structural properties of metal containing complexes in the gas-phase including UV/Vis spectroscopy, mass spectroscopy, and ion mobility spectroscopy. Complexes with metal centers also represent challenging compounds for the electronic structure theory due to their unfilled d-shell (in the case of transition metals) and f-shell (in the case of lanthanides and actinides).

The main goals of this thesis, which focuses on the theoretical description of mono- and multi-nuclear complexes with transition metal and lanthanide centers, can be divided into three parts (cf. structure of this thesis at the end of this introduction). First is the definition and theoretical investigation of cooperativity in transition metal complexes. The cooperativity in metal complexes is the key topic of the Collaborative Research Center "Cooperative Effects in Homo- and Heterometallic Complexes (3MET)" which funded this PhD project. Even though the term cooperativity seems familiar it is often difficult to define what exactly is meant by that.[6] The many-body expansion, which is a general approach usually used for obtaining accurate energies of large systems,[7] is used in this thesis to define the cooperativity in complexes with metal centers.

The second goal is to carry out a detailed theoretical investigation and to understand how the molecular structures of complexes containing lanthanides influence the optical properties (most usually luminescence) that can take place either at the lanthanide center or in its close vicinity from one of the coordinating ligands. The investigations focus particularly on compounds containing one or several europium ions Eu^{3+}. Due to its unique optical properties europium (and also other lanthanide) compounds are used in various fields ranging from electroluminescence, optical fibers and quantum cutters to memory devices. For example Tb-tris-(acetylacetonate) was used as an emitting layer in organic light-emitting

diodes (OLEDs).[8] In another OLED with bright red electroluminescence a tris-(dibenzoylmethanato)-phenanthroline–Eu^{3+} complex served as an emitting material.[9] Other devices with specific luminescence properties were constructed as well.[10] Complexes of different lanthanide ions were also used in plastic optical fibers (POFs) as signal amplifiers[11] and a complex of Eu^{3+} was one of them.[12] Complexes of lanthanides can also be used in memory devices, e.g. OLED devices that exhibit two different conductivity states – the high-conductance (ON state) and the low-conductance state (OFF state). It is possible to switch between these states by applying different voltages; different complexes of Sm^{3+}, Eu^{3+}, and Gd^{3+} were employed in these devices.[13] Lanthanide compounds can also be used in photon conversion either in upconversion[14,15] where a device absorbs two photons of low energy and emits one photon of high energy or in quantum cutters that work in the opposite way.[16] This short list of applications illustrates the need for the understanding of the optical properties of lanthanide complexes on a very fundamental level.

The third goal of this thesis is to develop auxiliary basis sets for lanthanides that facilitate the use of high level *ab initio* calculations for mid-sized molecular systems containing lanthanides. More specifically, auxiliary basis sets are needed to employ the resolution-of-identity approximation (sometimes called density fitting) to second-order Møller-Plesset[17] and coupled-cluster methods. Auxiliary basis sets for a large portion of the periodic system have been around for a long time,[18] however the corresponding auxiliary basis sets for lanthanides were not available up till now.

This thesis is structured as follows: after this introductory chapter the most important methods of quantum chemistry that are used in this thesis are described shortly in chapter 2. The most important results are presented in chapters 3 – 6, which describe a new application of the differential many-body decomposition scheme to the optical properties of complexes with transition metal centers (chapter 3), the detailed theoretical investigation of Eu^{3+} luminescence in various gas-phase complexes (chapter 4), the study of the phosphorescence of organic ligand molecules in different complexes containing lanthanide ions (chapter 5), and the development of auxiliary basis sets for lanthanides, which can be used in efficient computations at high levels of theory (chapter 6), respectively. In the last chapter (chapter 7) the main conclusions of this thesis are summarized.

2. Theoretical Methods

This introductory chapter describes the methods used in quantum chemistry. It is of course impossible to describe all the methods one can use, all their advantages and disadvantages, and all the pitfalls one should avoid. This is also not the purpose of this chapter as in my work I was mainly concerned with applying these methods rather than with their development or implementation. There are many textbooks, some of which are proved with time, that describe the theoretical methods better and in more detail than I ever could [19–22] and there is no need to copy them here. Nevertheless, I will shortly present the key ideas and equations behind the methods I used in my computations. I will try to focus on things that were new to me during my PhD study in the hope that some of them may be new to the reader as well.

The main quantity one tries to compute in theoretical chemistry is the energy of the molecular system under study. The energy is one of the important quantities that helps us understand e.g. what is the equilibrium distribution of two conformers or which possible reaction product is more stable and therefore more possible to obtain. The derivative of the energy with respect to the nuclear coordinates gives us the gradient that we can follow to find important points on the potential energy surface (PES) – minima that correspond to the stable molecules and saddle points (of first order) that correspond to the transition states in chemical reactions. Geometry optimizations are arguably the most common use of computational chemistry. Optical properties can be typically modeled by calculation of excited states – the absorption spectrum can be predicted from energies of electronic excitations, we can obtain information about the phosphorescence spectrum of a molecule by calculating the properties of states of different electron multiplicity, the nuclear magnetic shielding constants in nuclear magnetic resonance (NMR) spectroscopy can be computed as second order derivatives of energy. All these examples show that a reliable method for the calculation of molecular energies is required.

2.1. Hartree-Fock Theory

The physical problem we try to solve is the stationary Schrödinger equation

$$\hat{H}\Psi_k = E_k\Psi_k, \tag{2.1}$$

which is a differential equation and its solution is the wave function Ψ_k that describes the properties of state k of the molecular system of interest. The wave function depends on the positions of all nuclei and electrons in the system. A major simplification is obtained by applying the Born-Oppenheimer approximation[23] that separates the motion of nuclei and electrons – instead of the molecular Schrödinger equation we only solve the electronic Schrödinger equation that takes into account the positions of nuclei only parametrically as they create a potential for electrons to move in. The electronic Schrödinger equation then reads

$$\hat{H}_{\mathrm{el}}\Psi_\alpha = E_\alpha\Psi_\alpha. \tag{2.2}$$

Ψ_α is the electronic wave function describing state α, E_α is the energy of this state and $\hat{H}_{\mathrm{el}}$ is the electronic Hamiltonian. The electronic Hamiltonian takes the form (in atomic units):

$$\hat{H}_{\mathrm{el}} = \hat{T}_{\mathrm{e}} + \hat{V}_{\mathrm{ne}} + \hat{V}_{\mathrm{ee}} = -\sum_i^N \frac{1}{2}\nabla_i^2 + \sum_i^N v(\mathbf{r}_i) + \sum_{i<j}^N \frac{1}{r_{ij}}, \tag{2.3}$$

where the first term is the kinetic energy of the electrons and the last term is the electron–electron repulsion. The second term is the external potential due to the nuclei $v(\mathbf{r}_i) = -\sum_A \frac{Z_A}{r_{Ai}}$ (A denotes all nuclei).

We are interested in the lowest energy solution of equation (2.2), which corresponds to the ground state of the system under study. We can therefore drop the subscript α and express the many-electron wave function $\Psi(1,2,\ldots n)$ as an anti-symmetrized product of one-electron wave functions φ_i called molecular orbitals (MOs; C is a normalization constant):

$$\Psi(1,2,\ldots n) = |\varphi_1\varphi_2\cdots\varphi_n\rangle = C\begin{vmatrix} \varphi_1(1) & \varphi_1(2) & \ldots & \varphi_1(n) \\ \varphi_2(1) & \varphi_2(2) & \ldots & \varphi_2(n) \\ \vdots & \vdots & \ddots & \vdots \\ \varphi_n(1) & \varphi_n(2) & \ldots & \varphi_n(n) \end{vmatrix}. \tag{2.4}$$

The anti-symmetry of the determinant is needed to fulfill the Pauli principle for fermions and this type of wave function is called Slater determinant. We then try to solve the electronic Schrödinger equation variationally and obtain in the process the so-called Fock equations:

$$\hat{F}\varphi_j = \epsilon_j \varphi_j, \tag{2.5}$$

where ϵ_j are orbital energies and the Fock operator $\hat{F}$ is given by

$$\hat{F} = \hat{h} + \hat{J} - \hat{K}, \tag{2.6}$$

where $h = \sum_i \hat{h}_i$ denotes the core Hamiltonian with $\hat{h}_i = -\frac{1}{2}\nabla_i^2 - \sum_A \frac{Z_A}{r_{iA}}$ (i is the electron index while A is the index of respective nucleus) and $\hat{J}$, $\hat{K}$ are Coulomb and exchange operators, respectively, constituting of $\hat{J} = \sum_i \hat{J}_i$, $\hat{K} = \sum_i \hat{K}_i$ that are defined by their action on an arbitrary function $f(1)$:

$$\hat{J}_i f(1) = \left[\int \frac{\varphi_i^*(2)\varphi_i(2)}{r_{12}} d\tau_2\right] f(1), \tag{2.7}$$

$$\hat{K}_i f(1) = \left[\int \frac{\varphi_i^*(2) f(2)}{r_{12}} d\tau_2\right] \varphi_i(1), \tag{2.8}$$

where r_{12} is the distance between electrons 1 and 2 and $d\tau_2$ stands for the increment in all variables of electron 2 (including spin). This just very briefly sketched approach is the Hartree-Fock (HF) method.

In practice the Fock equations are solved iteratively employing the self–consistent field (SCF) approach. We first express the MOs as a linear combination of spatial atomic orbitals (AOs) χ_p:

$$\varphi_i(\mathbf{r}) = \sum_{p=1}^{N} C_{pi}\chi_p(\mathbf{r}) \tag{2.9}$$

and then arrive at the Roothaan–Hall equation in its matrix form:

$$\boldsymbol{FC} = \boldsymbol{SC\epsilon}, \tag{2.10}$$

where $\boldsymbol{C}$ is the matrix of molecular orbital coefficients C_{ij}, $\boldsymbol{\epsilon}$ is the diagonal matrix of orbital energies and the matrix elements of the Fock matrix $\boldsymbol{F}$ and the overlap matrix $\boldsymbol{S}$

are given in the usual *bra-ket* notation by (see also Appendix A):

$$F_{pq} = \langle \chi_p | \hat{F} | \chi_q \rangle, \tag{2.11}$$

$$S_{pq} = \langle \chi_p | \chi_q \rangle. \tag{2.12}$$

Detailed derivations and discussions of the HF–SCF method are given by Refs. [20, 24]. The HF method and the methods based on it (so called post-HF methods) have been and still are used extensively. The main problem is that they suffer from relatively high computational demands (cf. section 2.4). Some of the post-HF methods are popular for their efficiency of retrieving the correlation energy (in case of MP2)[17] and overall accuracy (in case of CCSD(T)).[25] Their high computational demands are, however, somewhat limiting especially in applying them to large molecules. These methods will be briefly sketched in the following section.

2.1.1. Møller-Plesset Perturbation Theory

The above described HF method only takes into account the average field created by all electrons and the movement of electrons is not correlated any further. The HF results therefore cannot be exact even in a complete basis. It is common to denote the difference between the HF complete basis set limit and the exact solution of the (nonrelativistic) Schrödinger equation as the correlation energy E_{corr}. The post-HF methods use the HF wave function as starting point for their estimates of the correlation energy.
One of the simplest post-HF methods is Møller-Plesset (MP) perturbation theory[17] where the Hamiltonian $\hat{H}$ is obtained as a perturbation of the zeroth-order Hamiltonian:

$$\hat{H} = \hat{H}_0 + \lambda \hat{V}, \tag{2.13}$$

where $\hat{H}_0 = \sum_j \hat{F}(j)$, λ is the perturbation parameter, and $\hat{V}$ is the perturbation operator. The wave function and energy can be expanded into first-, second-, and higher orders of perturbation in the parameter λ. The first-order energy correction is zero (i.e. $E_{\mathrm{MP1}} = E_{\mathrm{HF}}$) so the first estimate of the correlation energy is obtained from second-order perturbation

theory (MP2 method; for the notation see Appendix A):[17,18,26,27]

$$E_{\mathrm{MP2}} = \frac{1}{4} \sum_{i,a,j,b} \frac{|\langle ij||ab\rangle|^2}{\epsilon_i + \epsilon_j - \epsilon_a - \epsilon_b}, \tag{2.14}$$

where i, j denote occupied orbitals while a, b denote unoccupied orbitals. MP2 is the most popular of the MP perturbation approaches but higher-order methods of MP kind exist as well.[26]

2.1.2. Coupled-Cluster Theory

Another way of computing correlation energies is provided by coupled-cluster (CC) theory.[28,29] The main idea is to express the coupled-cluster wave function $|\mathrm{CC}\rangle$ by applying the exponential of a cluster operator $\mathcal{T}$ on the HF wave function $|\mathrm{HF}\rangle$:[30]

$$|\mathrm{CC}\rangle = e^{\mathcal{T}}|\mathrm{HF}\rangle, \tag{2.15}$$

where the exponential of a cluster operator $\mathcal{T}$ is:

$$\mathcal{T} = \sum_{i=1}^{N_{\max}} \mathcal{T}_i = \sum_{i=1}^{N_{\max}} \sum_{\mu_i} t_{\mu_i} \tau_{\mu_i}, \tag{2.16}$$

where t_{μ_i} are so-called amplitudes and τ_{μ_i} are excitation operators for which $\tau_{\mu_i}|\mathrm{HF}\rangle = |\mu_i\rangle$. We need to solve the Schrödinger equation for the CC wave function:

$$\hat{H}|\mathrm{CC}\rangle = E_{\mathrm{CC}}|\mathrm{CC}\rangle. \tag{2.17}$$

This is usually solved by projecting on the reference determinant $\langle\mathrm{HF}|$ and its excited determinants to obtain the CC energy and so-called CC-equations:

$$E_{\mathrm{CC}} = \langle\mathrm{HF}|\hat{H}e^{\mathcal{T}}|\mathrm{HF}\rangle, \tag{2.18}$$

$$0 = \langle\mu_i|e^{-\mathcal{T}}\hat{H}e^{\mathcal{T}}|\mathrm{HF}\rangle. \tag{2.19}$$

Different methods can be obtained by truncating the cluster operator in equation (2.16), e.g. the coupled-cluster singles and doubles (CCSD) method[31] is obtained for $\mathcal{T} = \mathcal{T}_1 + \mathcal{T}_2$.

Very popular is the CCSD(T) method[25] where the triple excitations are included in a perturbative manner.

As already mentioned the main disadvantage of the post-HF methods is their high computational demand. There are however other cheaper methods that are referred to as density functional theory (DFT) which are described in the following section.

All MP2 and CC computations (as well as all other computations unless explicitly stated otherwise) were performed using the TURBOMOLE program package.[32–34]

2.2. Density Functional Theory

Density functional theory methods are nowadays the most popular approaches in the field of quantum chemistry[35] and in some sense they became synonymous to 'computational chemistry' for some people. The foundations of DFT, however, are derived in a different way than HF theory just described. DFT method will be described in more detail here since it is the main method used for geometry optimizations in this thesis.

The main idea of DFT is that the electronic energy can be expressed as functional of the electron density, i.e.

$$E = E[\rho(\mathbf{r}_1)], \tag{2.20}$$

where the electron density is given by

$$\rho(\mathbf{r}_1) = N \int |\Psi(\mathbf{x}_1, \mathbf{x}_2, \ldots \mathbf{x}_N)|^2 ds_1 d\mathbf{x}_2 \cdots d\mathbf{x}_N. \tag{2.21}$$

The integration of the N-electron wave function $\Psi(\mathbf{x}_1, \mathbf{x}_2, \ldots \mathbf{x}_N)$ is carried out over all space–spin coordinates of electrons other than 1 and over the spin coordinate of electron 1. It is clear that the wave function that depends on $4N$ variables (positions and spins of N electrons) is a more difficult object to handle than an electron density function depending on 3 variables (x, y, z). The theory should be therefore appealing for its simplicity.

An important advancement was made in the mid-1960s due to two so-called Hohenberg-Kohn theorems.[36] The first theorem states and proves that the electron density determines the external potential up to an additive constant. Since the density also trivially determines the number of electrons ($\int \rho(\mathbf{r}) d\mathbf{r} = N$) the whole Hamiltonian (cf. equation (2.3)) is

determined by the density and we can write the energy as:

$$E[\rho] = V_{\mathrm{ne}}[\rho] + T[\rho] + V_{\mathrm{ee}}[\rho] = \int \rho(\mathbf{r}) v(\mathbf{r}) d\mathbf{r} + F[\rho], \tag{2.22}$$

$$F[\rho] = T[\rho] + V_{\mathrm{ee}}[\rho] = \langle \Psi | \hat{T} + \hat{V}_{\mathrm{ee}} | \Psi \rangle, \tag{2.23}$$

where $T[\rho]$, $V_{\mathrm{ne}}[\rho]$, and $V_{\mathrm{ee}}[\rho]$ are kinetic, nuclear–electron attraction, and electron–electron repulsion energies, respectively, and $F[\rho]$ is a universal functional of ρ.
The second Hohenberg-Kohn theorem states that the problem of finding the correct electron density obeys the variational principle, i.e. for a trial electron density $\tilde{\rho}(\mathbf{r})$ and therefore trial wave function $\tilde{\Psi}$ we get

$$\langle \tilde{\Psi} | \hat{H} | \tilde{\Psi} \rangle = \int \tilde{\rho}(\mathbf{r}) v(\mathbf{r}) d(\mathbf{r}) + F[\tilde{\rho}] = E[\tilde{\rho}] \geq E[\rho]. \tag{2.24}$$

In equation (2.24) the lowest energy is obtained for the true density (and therefore the true wave function). To find the correct density one needs to minimize the energy with respect to density variations. One can make use of the minimization using Lagrange multipliers to obtain the Euler–Lagrange equation[37]

$$\mu = v(\mathbf{r}) + \frac{\delta F[\rho]}{\delta \rho(\mathbf{r})}, \tag{2.25}$$

where $\frac{\delta F[\rho]}{\delta \rho(\mathbf{r})}$ is a functional derivative of $F[\rho]$ and μ is the Lagrange multiplier identified as the chemical potential $\mu = \frac{\partial E}{\partial N}$.
The practical approach to solve the minimization problem is given by the Kohn–Sham (KS) ansatz.[38] The functional $F[\rho]$ is reformulated as

$$F[\rho] = T_{\mathrm{s}}[\rho] + J[\rho] + E_{\mathrm{XC}}[\rho], \tag{2.26}$$

where $J[\rho]$ is the Hartree (Coulomb) repulsion of the density with itself given by $J[\rho] = \frac{1}{2} \int \int \frac{\rho(\mathbf{r}_1)\rho(\mathbf{r}_2)}{r_{12}} d\mathbf{r}_1 d\mathbf{r}_2$ and $T_{\mathrm{s}}[\rho]$ is the kinetic energy of the *non-interacting* system of N particles with density ρ. Comparing equations (2.23) and (2.26) we can write

$$E_{\mathrm{XC}}[\rho] = T[\rho] - T_{\mathrm{s}}[\rho] + V_{\mathrm{ee}}[\rho] - J[\rho] \tag{2.27}$$

and we call $E_{\mathrm{XC}}[\rho]$ exchange–correlation energy. Inserting (2.26) into (2.22) and minimizing as before we obtain for the Lagrange multiplier

$$\mu = v_{\mathrm{eff}}(\mathbf{r}) + \frac{\delta T_{\mathrm{s}}[\rho]}{\delta\rho(\mathbf{r})}, \tag{2.28}$$

$$v_{\mathrm{eff}}(\mathbf{r}) = v(\mathbf{r}) + \frac{\delta J[\rho]}{\delta\rho(\mathbf{r})} + \frac{\delta E_{\mathrm{XC}}[\rho]}{\delta\rho(\mathbf{r})}. \tag{2.29}$$

Comparing equations (2.25) and (2.28) one can see the main advantage of the KS approach: the density of the interacting system with the external potential $v(\mathbf{r})$ is the same as the density of the non-interacting system with the external potential $v_{\mathrm{eff}}(\mathbf{r})$. We can make use of this and solve the problem for non-interacting electrons using a Slater determinant to obtain the desired electron density $\rho(\mathbf{r})$:

$$\left(-\frac{1}{2}\nabla^2 + v_{\mathrm{eff}}(\mathbf{r})\right)\varphi_i(\mathbf{r}) = \epsilon_i\varphi_i(\mathbf{r}), \tag{2.30}$$

$$\rho(\mathbf{r}) = \sum_i^N \varphi_i^2(\mathbf{r}). \tag{2.31}$$

With the expression for the kinetic energy of a non-interacting system

$$T_{\mathrm{s}}[\rho] = \sum_i^N \langle\varphi_i| -\frac{1}{2}\nabla^2|\varphi_i\rangle \tag{2.32}$$

we can insert the density into the energy expression

$$E = \int \rho(\mathbf{r})v(\mathbf{r})d(\mathbf{r}) + T_{\mathrm{s}}[\rho] + J[\rho] + E_{\mathrm{XC}}[\rho] \tag{2.33}$$

and obtain the final energy. The problem of this otherwise exact approach is the form of the exchange–correlation functional $E_{\mathrm{XC}}[\rho]$, which is unknown. Different approaches to model $E_{\mathrm{XC}}[\rho]$ exist, some of which will be described in the following paragraphs.
The derivation of DFT together with more detailed descriptions is covered well in many textbooks; see e.g. Refs. [21, 37, 39].

2.2.1. Approximations of the $E_{\mathrm{XC}}[\rho]$ Functional

There are many different approximations to the exchange-correlation functional $E_{\mathrm{XC}}[\rho]$ and it is common to sort them according to their complexity into a so-called Jacob's ladder.[40] The different rungs of the ladder include (going from less complicated to more complicated functionals):

- the local density approximation (LDA) functionals that depend only on the density – $E_{\mathrm{XC}} = \int G(\rho) d\mathbf{r}$,
- the generalized gradient approximation (GGA) functionals that depend on the density gradient as well – $E_{\mathrm{XC}} = \int G(\rho, \nabla\rho) d\mathbf{r}$,
- the meta GGA functionals that depend on higher order derivatives of the density – e.g. $E_{\mathrm{XC}} = \int G(\rho, \nabla\rho, \nabla^2\rho) d\mathbf{r}$,
- the hybrid functionals that combine GGAs with some portion of HF exchange – $E_{\mathrm{XC}} = \int G(\rho, \nabla\rho) d\mathbf{r} + \xi E_{\mathrm{X}}^0$,
- the double hybrid functionals that also depend on the virtual KS orbitals – $E_{\mathrm{XC}} = \int G(\rho, \nabla\rho, \psi_a) d\mathbf{r} + \xi E_{\mathrm{X}}^0$.

The detailed discussion of all different exchange-correlation functionals is well beyond the scope of this thesis (or even a specialized review article) so I will only focus on three functionals that were frequently used in the projects of this thesis.
Usually there are two separate parts in the exchange-correlation functional that correspond to the exchange (E_{X}) and correlation (E_{C}), respectively. It is also common (but not necessary) to name the functional after its author/inventor. If more authors were involved (e.g. for different parts of the exchange-correlation functional) a combination of names is used as we shall see.
The first functional used in this thesis is the Becke-Perdew (BP) functional which is of GGA type. For a general GGA functional the exchange part of the energy E_{X} depends on the dimensionless quantity $x(\mathbf{r}) = \frac{\nabla\rho(\mathbf{r})}{\rho^{4/3}(\mathbf{r})}$:

$$E_{\mathrm{X}}[\rho] = \int \rho^{4/3}(\mathbf{r}) f(x(\mathbf{r})) d\mathbf{r} \tag{2.34}$$

and Becke proposed the form of function f as[41]

$$f = C_{\mathrm{X}} + \beta x^2/(1 + 6\beta x \operatorname{arcsinh} x), \tag{2.35}$$

with $C_{\mathrm{X}} = 0.7386$ and β is the only adjustable parameter determined by a fit to atomic exchange energies of the noble gas atoms. The correlation part of the functional was given by Vosko, Wilk, and Nusair (VWN)[42] and Perdew.[43]

The second functional used in this thesis more often is the (arguably most famous and popular) hybrid functional called B3LYP.[44] The main idea behind hybrid functionals comes from the analysis known as *adiabatic connection*[44,45] where the interaction is turned on gradually when one moves from the non-interacting towards the fully interacting system. From this analysis it follows that a portion of exact exchange $E_{\mathrm{X}}^0 = -\frac{1}{4}\int\int \frac{\rho_1(\mathbf{r}_1,\mathbf{r}_2)}{r_{12}} d\mathbf{r}_1 d\mathbf{r}_2$ needs to be included in the exchange-correlation functional (where $\rho_1(\mathbf{r}_1, \mathbf{r}_2)$ is the one-particle density matrix).[37] The correlation part of the B3LYP functional comes from the work of Lee, Yang, and Parr[46] (LYP) and the explicit expression of the B3LYP exchange-correlation reads:

$$\mathrm{B3LYP} \equiv (1-A)E_{\mathrm{X}}^{\mathrm{Dirac}} + AE_{\mathrm{X}}^0 + B\Delta E_{\mathrm{X}}^{\mathrm{B}} + (1-C)E_{\mathrm{C}}^{\mathrm{VWN}} + CE_{\mathrm{C}}^{\mathrm{LYP}}, \tag{2.36}$$

with $E_{\mathrm{X}}^{\mathrm{Dirac}} = C_{\mathrm{X}} \int \rho^{4/3}(\mathbf{r}) d\mathbf{r}$ and A, B, and C are empirically fitted parameters.

The last important functional used in my thesis is the double-hybrid B2PLYP functional.[47] It calculates the correlation energy in the perturbative way much like it is done in the MP2 method but with KS orbitals instead of the HF ones. The expression for the exchange-correlation functional reads:

$$E_{\mathrm{XC}}^{\mathrm{B2PLYP}} \equiv (1-A)E_{\mathrm{X}}^{\mathrm{B}} + AE_{\mathrm{X}}^0 + (1-C)E_{\mathrm{C}}^{\mathrm{LYP}} + CE_{\mathrm{C}}^{\mathrm{PT2}} \tag{2.37}$$

with two parameters $A = 0.53$ and $C = 0.27$. The perturbative expression $E_{\mathrm{C}}^{\mathrm{PT2}}$ is the same as in the MP2 method (cf. equation(2.14)).

2.2.2. Dispersion Corrections to Density Functional Theory

One of the problems of HF and DFT is the description of weakly bounded systems, e.g. complexes that mainly interact via long range correlation (dispersion, London, or van der Waals) interactions that have the famous $1/R^6$ behavior. A special attention needs to be given to their treatment in the framework of DFT. There exist different methods to account for dispersion in DFT and probably the most straightforward and most popular is called DFT-D.[48] The current third generation[49] (denoted DFT-D3) computes the energy as

$$E_{\text{DFT-D3}} = E_{\text{DFT}} + E_{\text{disp}}, \tag{2.38}$$

where E_{DFT} is the energy obtained from a regular DFT computation and E_{disp} is a dispersion correction that consists of two- and three-body contributions:

$$E_{\text{disp}} = E^{(2)} + E^{(3)}. \tag{2.39}$$

The expressions for $E^{(2)}$ and $E^{(3)}$ include interatomic distances, atom pair specific dispersion coefficients, carefully calibrated damping functions, and cutoff radii.[49,50] A more detailed discussion of the method is beyond the scope of this thesis.
Since the D3 correction does not depend on the electronic structure itself but only on the molecular geometry (i.e. on the positions of the atoms), it is an inexpensive way to include dispersion interactions in a computation and it is therefore generally recommended for DFT.

2.2.3. Excitation energies: Time-Dependent Density Functional Theory

Density functional theory has been very successful in computing ground state energies of molecular systems. It is possible also to compute excitation energies using DFT (the so-called ΔSCF approach), where two "ground state" energies for the system are determined – these states need to be either of different multiplicity (e.g. S_0 vs. T_1 states) or, in symmetric molecular systems, they need to have different distribution of electrons in their respective irreducible representations. The ΔSCF approach is therefore somewhat limited. DFT also gives the framework for time-dependent density functional theory (TDDFT) which can

be used for the efficient computation of excitation energies without the restrictions of the ΔSCF approach. The TDDFT method will be described in this section.

The formal justification of TDDFT was given in the mid-1980s by the so-called Runge-Gross theorems,[51] which are the time-dependent analogs of the Hohenberg-Kohn theorems of DFT. The first Runge-Gross theorem proves that the time-dependent charge density and the initial wave function $\Psi_0 = \Psi(t = t_0)$ determine the time-dependent external potential and therefore time-dependent Hamiltonian up to an additive function of time:

$$(\rho(\mathbf{r}, t), \Psi_0) \rightarrow \hat{H}(t) + C(t). \tag{2.40}$$

In analogy to equation (2.30) we can write a *time-dependent* Kohn-Sham equation:[52]

$$\left(-\frac{1}{2}\nabla^2 + v_{\text{ext}}(\mathbf{r}, t) + \frac{\delta J[\rho((\mathbf{r}, t)]}{\delta\rho(\mathbf{r}, t)} + \frac{\delta E_{\text{XC}}[\rho(\mathbf{r}, t)]}{\delta\rho(\mathbf{r}, t)}\right)\psi(\mathbf{r}, t) = i\frac{\partial\psi(\mathbf{r}, t)}{\partial t}. \tag{2.41}$$

The exchange-correlation potential $v_{\text{XC}} = \frac{\delta E_{\text{XC}}}{\delta\rho}$ is usually approximated within the adiabatic approximation (i.e. assuming that the external potential changes only slowly in time) with the time-independent exchange-correlation potential:

$$v_{\text{XC}}[\rho(\mathbf{r}, t)] = v^0_{\text{XC}}[\rho_0(\mathbf{r})]\Big|_{\rho_0\rightarrow\rho(\mathbf{r},t)}. \tag{2.42}$$

In practice one does not solve the time-dependent KS equations but instead uses a linear response theory to get the excitation energies of the system. The external potential in the system $v(\mathbf{r}, t)$ is of the form

$$v_{\text{ext}}(\mathbf{r}, t) = v_0(\mathbf{r}) + v_1(\mathbf{r}, t), \tag{2.43}$$

where $v_1(\mathbf{r}, t)$ is some time-dependent perturbation that was turned on at some point t_0. The density-density response function for the system is defined as

$$\chi(\mathbf{r}, t, \mathbf{r}', t') = \frac{\delta\rho[v_{\text{ext}}](\mathbf{r}, t)}{\delta v_{\text{ext}}(\mathbf{r}', t')}\Big|_{v_{\text{ext}}[\rho_0]}, \tag{2.44}$$

which is needed for the linear density response function ρ_1:

$$\rho_1(\mathbf{r},t) = \int dt' \int d^3r' \chi(\mathbf{r},t,\mathbf{r}',t') v_1(\mathbf{r}',t'). \tag{2.45}$$

The density-density response function can also be written for the non-interacting system of electrons:

$$\chi_{\mathrm{KS}}(\mathbf{r},t,\mathbf{r}',t') = \left.\frac{\delta\rho[v_{\mathrm{KS}}](\mathbf{r},t)}{\delta v_{\mathrm{KS}}(\mathbf{r}',t')}\right|_{v_{\mathrm{KS}}[\rho_0]} \tag{2.46}$$

and an expression analogous to equation (2.45) for the linear response of the non-interacting system can be written. After a Fourier transform the linear response function depends on the frequency ω. The useful property of the linear response function is that it has poles at the frequencies corresponding to the excitation energies of the unperturbed system (i.e. the ground state system of interest). The positions of the poles can be calculated (much like in the case of DFT) by first calculating the poles of the non-interacting system. The shift between poles of the real and non-interacting system can be calculated using the so-called time-dependent exchange-correlation kernel f_{XC}:[53]

$$f_{\mathrm{XC}}[\rho](\mathbf{r},t,\mathbf{r}',t') = \frac{\delta v_{\mathrm{XC}}(\mathbf{r},t)}{\delta\rho(\mathbf{r}',t')}. \tag{2.47}$$

Having derived the above equations the last step is to express the density-density response of the non-interacting system in terms of molecular orbitals and the problem of computing the spectrum of excitation energies ω transforms into a pseudo-eigenvalue problem also known as the Casida's equation:[52]

$$\begin{pmatrix} \mathbf{A} & \mathbf{B} \\ \mathbf{B}^* & \mathbf{A}^* \end{pmatrix} \begin{pmatrix} \vec{X} \\ \vec{Y} \end{pmatrix} = \omega \begin{pmatrix} \mathbf{1} & \mathbf{0} \\ \mathbf{0} & -\mathbf{1} \end{pmatrix} \begin{pmatrix} \vec{X} \\ \vec{Y} \end{pmatrix}, \tag{2.48}$$

$$A_{ai,bj} = \delta_{ij}\delta_{ab}(\epsilon_a - \epsilon_i) + (ai|jb) - a_{\mathrm{X}}(ab|ji) + (1-a_{\mathrm{X}})(ai|f_{\mathrm{XC}}|jb), \tag{2.49}$$

$$B_{ai,bj} = (ai|bj) - a_{\mathrm{X}}(aj|bi) + (1-a_{\mathrm{X}})(ai|f_{\mathrm{XC}}|bj). \tag{2.50}$$

As usually[20] indices $ij\ldots$ denote occupied orbitals while $ab\ldots$ denote virtual orbitals and $pq\ldots$ denote any general orbitals; a_{X} represents the amount of HF exchange ($a_{\mathrm{X}} = 1$ for

TDHF). The two-electron integrals are written here in Mulliken's notation which reads (see also Appendix A):

$$(\mu\nu|\kappa\lambda) = \int\int \psi_\mu^*(\mathbf{r}_1)\psi_\nu(\mathbf{r}_1)\frac{1}{\mathbf{r}_{12}}\psi_\kappa^*(\mathbf{r}_2)\psi_\lambda(\mathbf{r}_2)\,\mathrm{d}\mathbf{r}_1\,\mathrm{d}\mathbf{r}_2. \tag{2.51}$$

An interesting alternative to the TDDFT is the so-called Tamm-Dancoff approximation[54] (TDA) that follows directly from equation (2.48) by neglecting the **B** matrix and solving

$$\mathbf{A}\vec{X} = \omega\vec{X}. \tag{2.52}$$

The advantage of TDA over TDDFT lies in its reduced complexity as clearly a smaller problem needs to be solved. Note that in the TDHF case the TDA approach is equivalent to the configuration interaction singles (CIS) method.

TDDFT can provide good results but it has also some shortcomings: the dependence on the exchange-correlation functional used[55] (which is the problem it shares with classical DFT) or the difficulties with the description of charge transfer excitations.[56] The latter is somewhat improved by using hybrid functionals or functionals specially designed to treat charge transfer states.[57,58] In general TDDFT results agree with experimental excitations within few tenths of eV. More reliable but also more computationally demanding methods are based on coupled-cluster theory.[59]

Because of its efficiency TDDFT has become a method of choice for computing excitation energies and hence absorption spectra of large molecules.[52] The method, however, still scales as $\mathcal{O}(N^4)$, which makes it (while still being much more usable than more expensive wave function based methods) difficult to apply for calculating absorption spectra of very large molecules. For that reason a simplified method was developed first for the TDA method that is denoted sTDA (*simplified* TDA).[60] It introduces two new approximations. First the four-index two-electron integrals in equation (2.49) are replaced with a monopole type approximation:

$$(pq|rs) \approx \sum_A^N \sum_B^N q_{pq}^A q_{rs}^B\,\gamma(A,B), \tag{2.53}$$

where A, B are atom labels, q_{pq}^A is a transition density charge obtained from a Löwdin population analysis[61] $q_{pq}^A = \sum_{\mu\in A} C'_{\mu p}C'_{\mu q}$, and $\gamma(A,B)$ is a damped Coulomb law that

has a different form for Coulomb and exchange type integrals. The approximation (2.53) is quite severe but was shown to work quite well for the computation of absorption spectra in large molecules.[60] One can say it is a resolution-of-identity (RI) type of approximation (the RI approximation will be discussed in detail in section 2.4).

The second approximation made in the development of the sTDA method is the truncation of the excitation space. This is based on the assumption that the state of interest consists of so-called primary configuration state functions (P-CSF) and only interacts strongly with a small number of secondary configurations (S-CSF). The P-CSF are determined by an ordered set of single excitations with energy lower than a user defined energy $E_{\max}$. The set is ordered according to their diagonal Hamiltonian matrix elements. There is a different threshold of perturbative energy contributions to P-CSFs that defines which configurations will be included into S-CSF. The contribution of other configurations is taken into account in a perturbative way.[60]

From a practical point of view the converged KS orbitals, the information about the amount of HF exchange (a_{X}), and the energy threshold $E_{\max}$ are required to apply the sTDA method. An analogous approximation to the full TDDFT method called sTDDFT was developed as well.[62] In a typical application of an absorption spectrum of oligonuclear metal complex that is discussed in chapter 3 the computational time is reduced from ≈ 10 days (for TDDFT with B3LYP functional using 8 cores) to ≈ 15 minutes (for sTDDFT using only 1 core on the same compute server). The appeal of the sTDDFT/sTDA approach is not difficult to see.

All sTDA and sTDDFT computations were performed with a program called sTDA.[60]

2.3. Calculations of Metal Containing Molecules

The main focus of this thesis is on the computations of complexes that contain heavy metals – either one or more transition metals or one or more lanthanides. The electronic structure of metals is more complicated than the electronic structure of atoms that usually constitute organic molecules (say the first three rows of the periodic table) and therefore some special procedures are needed to perform computations on molecular systems containing metals. In this section I will describe two main tools that are used heavily in this thesis. The first are effective core potentials (ECPs) that are used to simplify the calculation of atoms with

many electrons. While they are certainly not limited to metal atoms and can be used for any atom, they are of great use especially in lanthanide complexes computed in this thesis and also for the basis set development described in chapter 6. The second tool is an effective ligand field Hamiltonian that is used to compute optical properties of lanthanide ions in complexes and plays a key role in chapter 4.

2.3.1. Effective Core Potentials

Up to this point we were always considering all electrons in our models. Valence electrons are the most important for chemical bonding while the core electrons are shielded and remain (almost) unchanged when the atom is part of a molecule. For this reason it would seem reasonable to take into account only the chemically relevant valence electrons. The core electrons provide mostly shielding of the nuclear charge, which affects the valence electrons: this is the main idea behind effective core potentials (ECPs).

The advantage of ECPs is twofold: firstly, the replacement of core electrons with a potential reduces the number of electrons that have to be described by our method making the computation less demanding and therefore faster, and secondly, ECPs provide the most efficient inclusion of relativistic effects for core electrons as the potentials are usually obtained by a fit to results obtained with a relativistic method. Relativistic effects can play an important role in (but not only) heavy elements such as lanthanides.[63,64]

To construct an ECP a valence-only Hamiltonian $\hat{H}_\mathrm{v}$ is constructed as[65]

$$\hat{H}_\mathrm{v} = -\frac{1}{2}\sum_{i}^{n_\mathrm{v}} \nabla_i^2 + \sum_{i<j}^{n_\mathrm{v}} \frac{1}{r_{ij}} + \sum_{i}^{n_\mathrm{v}} \sum_{\lambda}^{N} \left[-\frac{Q_\lambda}{r_{\lambda i}} + \Delta\hat{V}_\mathrm{cv}^\lambda(i) \right] + \hat{V}_\mathrm{cpp} + V_\mathrm{cc}, \tag{2.54}$$

where indices c and v denote core and valence electrons, respectively. The number of valence electrons n_v from the total number of electrons n is deduced by taking the difference between the nuclear charge Z_λ and core charge Q_λ for every core λ (in this part *nucleus* describes only the protons and neutrons in the atom while *core* is the nucleus together with the core electrons; total number of nuclei is N):[65]

$$n_\mathrm{v} = n - n_\mathrm{c} = n - \sum_{\lambda}^{N} (Z_\lambda - Q_\lambda). \tag{2.55}$$

The other terms in equation (2.54) represent the core-polarization potential $\hat{V}_\mathrm{cpp}$, the re-

pulsion between cores and nuclei of the system V_{cc} and atom-specific contributions to core-valence interactions $\Delta\hat{V}_{\mathrm{cv}}^{\lambda}(i)$.

The repulsion between cores and nuclei can be expressed via[65]

$$V_{\mathrm{cc}} = \sum_{\lambda<\mu}^{N} \left[\frac{Q_\lambda Q\mu}{r_{\lambda\mu}} + \Delta V_{\mathrm{cc}}^{\lambda\mu}(r_{\lambda\mu}) \right]. \tag{2.56}$$

The aim of ECPs is to model accurately the unknown quantities $\Delta\hat{V}_{\mathrm{cv}}^{\lambda}(i)$, $\Delta V_{\mathrm{cc}}^{\lambda\mu}$, and $\hat{V}_{\mathrm{cpp}}$. There are four main approximations used during the derivation of ECPs: first is the separation of the core and valence electrons, which can be done exactly for a mean-field model of particles (HF theory) but only approximately when electron correlation is taken into account. Second is the assumption that the cores remain unchanged regardless of the chemical environment in molecules, which corresponds to the frozen-core (FC) approximation in an atom. As a third approximation the contribution of core electrons to the all electron Hamiltonian is replaced by an ECP modeling the HF potential and finally the cores are assumed to interact with other cores only via the Coulomb interaction which may be problematic for some large core ECPs.[65]

The ECPs used in computations with lanthanide atoms, which are the most important for this thesis are discussed in detail in section 6.1.

2.3.2. Splitting of the f-shell Levels

In chapter 4 one of the main problems is to compute the splittings of Eu^{3+} ion levels in the presence of a ligand field. We will use this ion as an example to discuss the computation of energy level splittings in lanthanides. The electronic ground state configuration of Eu^{3+} is [Xe]$4f^6$. The 6 f-electrons can be distributed – fulfilling the Pauli exclusion principle – into the 7 f-orbitals (with $l_i = -3 \ldots 3$). Each configuration will have its own orbital angular momentum $M_L = \sum m_{l(i)}$ and its total spin angular number $M_S = \sum m_{s(i)}$. This gives rise to the so-called SL matrix and the corresponding states derived from this matrix are labeled ${}^{2S+1}L$.[66] These terms appear due to the Coulomb interaction between the f-electrons. Hund's rule can be applied to determine the ground state term – the ground state is the state with the greatest spin multiplicity; in case of a tie the one with largest L. For Eu^{3+} the ground state term is ${}^7F$ – the only septet.

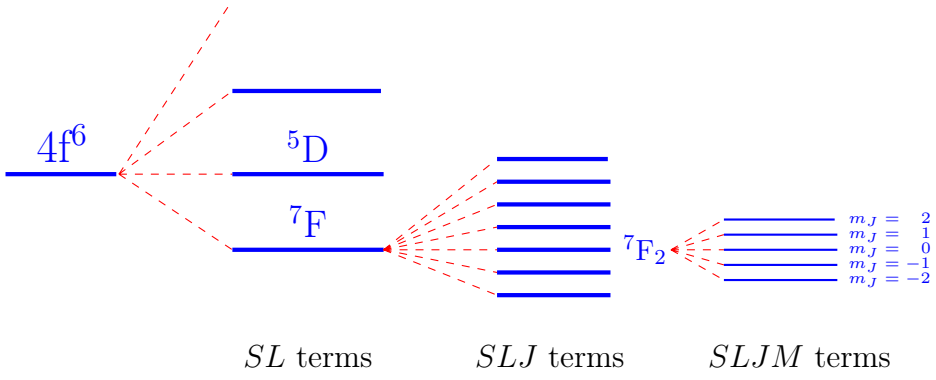

Figure 2.1: Schematic representation of splitting of Eu^{3+} energy levels into SL, SLJ, and $SLJM$ terms. Splitting is not in scale.

The second kind of interaction to be taken into account is the spin–orbit coupling that stems from the interaction between the magnetic moment of the electron with the magnetic field created by its motion. The spin–orbit interaction is especially important for heavy elements (like lanthanides) as its magnitude increases with the nuclear charge as Z^4.[67] The amount of splitting due to the spin–orbit interaction is comparable to the Coulomb splitting in the so-called intermediate coupling scheme which is usually appropriate for lanthanides (e.g. for light elements the Coulomb splitting is much larger than spin–orbit coupling). The SL terms split due to spin–orbit coupling to the so-called SLJ terms with $J = |L - S|, |L - S + 1|, \ldots, |L + S|$ which are labeled ${}^{2S+1}L_J$. In our example the ${}^7F$ ground state splits to (since $S = 3$, $L = 3$) ${}^7F_0$, ${}^7F_1$, ${}^7F_2$, ${}^7F_3$, ${}^7F_4$, ${}^7F_5$, and ${}^7F_6$ states.
When the lanthanide ion is put into a crystal or ligand field an additional (and energetically much smaller) splitting takes place. The splitting depends on the symmetry of the ligand field and in the case of very low symmetry (C_1) the splitting into $(2J+1)$ so-called $SLJM$ terms occur. The states are labeled with the corresponding value of $m_J = -J, -J+1, \ldots, J$, e.g. the ${}^7F_2$ state splits into five states with $m_J = -2 \ldots 2$. The total splitting of f-electron levels is shown schematically in Figure 2.1.
The final number of $SLJM$ states to be calculated depends on the number of f electrons n in the ion

$$N_{\text{states}} = \frac{14!}{n!(14-n)!} \tag{2.57}$$

i.e. for Eu^{3+} there are 3003 microstates. It is very demanding to calculate these energy levels that often differ only by about a hundred wave numbers within one multiplet even for small

molecules (see Ref. [68] and references therein) using relativistic configuration interaction (CI) methods. However, we need to do these computations routinely for relatively large molecules and we want to compare our results to the experiment. Therefore we need an efficient and reliable method to compute these states. Effective ligand field Hamiltonians were used for a long time for exactly these reasons so it is natural to use them. I describe a construction of an appropriate effective Hamiltonian in the next section.

2.3.3. Effective Ligand Field Hamiltonian

Generally speaking a *complete* Hamiltonian describes the molecular system perfectly and its spectrum consists of the true eigenstates of interest. In comparison the *effective* Hamiltonian tries to reproduce some part of the spectrum of eigenstates of the complete Hamiltonian, e.g. only a ground state or few lowest lying excitations, states without external magnetic and electric field and so on. Many different effective Hamiltonians exist that are applied to specific problems, e.g. the spin-Hamiltonian for NMR, the Hückel Hamiltonian for aromatic systems, or (in some sense) the HF Hamiltonian which describes electrons in a mean-field generated by other electrons. The disadvantage of effective Hamiltonians is their limited applicability; their advantage is their very much reduced complexity and computational demand compared to the complete Hamiltonian. In this section the effective Hamiltonian describing the multiplets of f-shell electrons will be described.
Following the discussion of state splittings in the previous section the effective Hamiltonian used for the f-splittings $\hat{H}_{\text{eff}}$ has three parts:

$$\hat{H}_{\text{eff}} = \hat{H}_{\text{C}} + \hat{H}_{\text{SO}} + \hat{H}_{\text{LF}}, \tag{2.58}$$

where $\hat{H}_{\text{C}}$, $\hat{H}_{\text{SO}}$, and $\hat{H}_{\text{LF}}$ correspond to Coulomb, spin–orbit, and ligand field interactions, respectively. This effective Hamiltonian needs to be diagonalized to which end one needs to compute the corresponding matrix elements. The corresponding theory of many electron spectra was first described by Racah.[69–73]
The Coulomb Hamilton operator is given as a sum of tensor operators $\hat{H}_{\text{C}} = \sum_{k=0,2,4,6} C_i^k C_j^k$ and the matrix elements for states with total spin angular momentum S and total orbital

angular momentum L are given by (for a general lanthanide ion Ln^{3+} with N electrons):

$$\begin{aligned}\langle 4f^N SL|C_i^k C_j^k|4f^N S'L'\rangle =&\delta_{SS'}\delta_{LL'}49(-1)^L \\ &\times \sum_{k=0,2,4,6} \begin{pmatrix} 3 & k & 3 \\ 0 & 0 & 0 \end{pmatrix}^2 \begin{Bmatrix} 3 & 3 & k \\ 3 & 3 & L \end{Bmatrix} F_k,\end{aligned} \tag{2.59}$$

where F_k are the Slater integrals and $\begin{pmatrix}\dots\end{pmatrix}$ and $\begin{Bmatrix}\dots\end{Bmatrix}$ represent Wigner 3-j and Wigner 6-j symbols, respectively.[70] The Slater integrals are material specific parameters and are obtained from fits to solid state experimental data. Two different notations for Slater integrals exist where:[66]

$$\begin{aligned}F_0 =&F^0, \\ F_2 =&F^2/225, \\ F_4 =&F^4/1089, \\ F_6 =&25F^6/184041.\end{aligned} \tag{2.60}$$

Matrix elements of equation (2.59) can then be tabulated in the form:[74]

$$\langle 4f^N SL|\hat{H}_C|4f^N S'L'\rangle = \sum_{k=0}^{3} e_k E^k, \tag{2.61}$$

where e_k are tabulated coefficients of fractional parentage and parameters E^k can be computed from Slater integrals via:[72]

$$\begin{aligned}E^0 =&F_0 - 10F_2 - 33F_4 - 286F_6, \\ E^1 =&(70F_2 + 231F_4 + 2002F_6)/9, \\ E^2 =&(F_2 - 3F_4 + 7F_6)/9, \\ E^3 =&(5F_2 + 6F_4 - 91F_6)/3.\end{aligned} \tag{2.62}$$

The F^0 Slater integral is usually omitted when relative energies of multiplets are to be computed (like it is in this thesis) as it only creates a uniform shift of all multiplets. The key message here is that we have three empirical parameters – F^2, F^4, and F^6 in our effective Hamiltonian.

The spin–orbit part of the effective Hamiltonian is given by:[66]

$$\langle 4f^N SLJ|\hat{H}_{\mathrm{SO}}|4f^N S'L'J'\rangle = \zeta(-1)^{J+L+S'}\sqrt{l(l+1)(2l+1)} \times \begin{Bmatrix} S & S' & 1 \\ L' & L & J \end{Bmatrix} \langle l^N SL||V^{(11)}||l^N S'L'\rangle, \tag{2.63}$$

where ζ is a spin–orbit coupling parameter and $\langle \cdots || \cdots || \cdots \rangle$ is a reduced matrix element that can be computed using the tabulated coefficients of fractional parentage.[66,74]

Last part of the effective Hamiltonian, the ligand field (or crystal field) Hamiltonian, is determined from the charge surrounding the rare earth ion of interest. It is responsible for the final splitting of the f-electron levels into $SLJM$ levels. The formalism was described by Stevens.[75]

The most important part for the discussion in this thesis is that the effective Hamiltonian has four adjustable parameters in total – the Slater integrals F^2, F^4, and F^6 and the spin–orbit coupling scaling parameter ζ. The computations with this effective Hamiltonian presented in this thesis were performed using the McPHASE program.[76]

2.4. Efficiency in Quantum Chemical Computations

One of the main limitations of quantum chemical computations is their computational demand, i.e. the demand on processing speed and memory of a computer. It is common to talk about *scaling* of quantum chemical methods to describe how much time (since the time is usually the main limitation) it takes to complete a calculation for a given system. The size of the system is denoted N and is related to the number of atoms (and therefore the size of the basis set used). The scaling in most cases is polynomial and is written as $\mathcal{O}(N^{\mathrm{X}})$ where X is some number. For example a quadratic scaling is denoted as $\mathcal{O}(N^2)$ and means that if it takes t_0 time to run a computation for a given molecule of size N_0 then it would take $2^2 t_0 = 4t_0$ to compute a molecule of size $2N_0$ (which could be realized approximately as a dimer of the original molecule). This seems already quite unfavorable and it gets only worse. The HF or DFT methods described at the beginning of this chapter have (in their straightforward formulation) a scaling of $\mathcal{O}(N^4)$, the cheapest post-HF method that recovers some part of electron correlation, the MP2 method, has a

scaling of $\mathcal{O}(N^5)$, and the famous highly accurate CCSD(T) method (notoriously referred to as *gold standard of computational chemistry*) has a scaling of $\mathcal{O}(N^7)$. To put this into perspective in chapter 5 computations at the CCSD(T)/def2-TZVPP level of theory are presented for the $[Lu(PLN)_2]^+$ molecule that took (for the triplet state, using 8 cores in parallel) about 73 days so roughly 2.5 months (on a compute node featuring two 10 core Intel(R) Xeon(R) E5-2687W v3 (3.10 GHz) processors, 768 GB DDR4 main memory, and eight striped 4TB SATA3 hard disks). If the same computations were to be performed e.g. on the $[Eu(PLN)_4Ca]^+$ molecule that is discussed in chapter 4, a molecule roughly twice the size of $[Lu(PLN)_2]^+$, it would have taken more than 25 years (which makes it way beyond the time-span of a typical PhD project). The problem of scaling is ubiquitous in quantum chemistry and different approaches were taken to tackle it.

Much research was done to develop methods with *reduced scaling*, ideally linear scaling approaches.[77–82] These methods include composite schemes where the molecule is partitioned into subparts and approaches that exploit the idea that electron correlation is a local property and only localized orbitals will contribute significantly. Thresholds are usually set up that define the distance to which the correlation will be computed. This reduces the scaling of the method at hand and also introduces an error that is (hopefully) small. Reduced scaling approaches are one of the 'hot topics' in the field of quantum chemistry and will be surely developed extensively in the near future.

Another way to tackle the scaling problem (up to a certain degree as the 'scaling wall' will always win) is the use of parallel computing. If more cores of a multi-core computer are used to run the computation the results are obtained faster. In an ideal case the computation is sped up N times (compared to the computation with one core) if N cores are used. In some favorable cases the speed-up can be even larger but usually it is lower. Special programs need to be developed to run a quantum chemical computation in parallel. Some parts of the code (such as, e.g. a direct SCF approach) can be parallelized very well while others are problematic. As an example the graph of speed-ups recorded for a typical computation at the DFT level of theory with the TURBOMOLE program package[32–34] is presented in Figure 2.2.

Yet another way to reduce the time that it takes to run a computation is the use of the so-called resolution-of-identity (RI) approximation that will be described in detail in the next section. Note that all computations presented in this thesis (DFT, HF, MP2, and CC) were

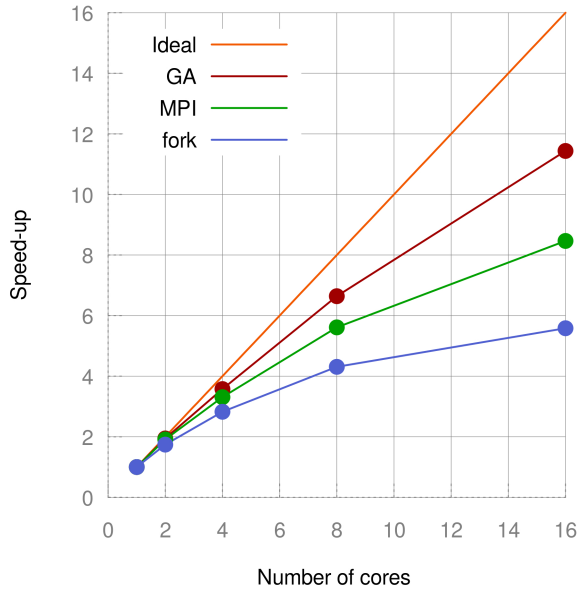

Figure 2.2: Speed-up with respect to the number of cores used measured for 20 iterations of a SCF cycle in the computation of a valinomycin molecule at the (RI)BP/def2-TZVPP level of theory ($\approx$ 3700 basis functions). Three different types of parallelization of the TURBOMOLE program package are presented. These benchmark computations were performed on a compute node featuring two 10 core Intel(R) Xeon(R) E5-2687W v3 (3.10 GHz) processors, 768 GB DDR4 main memory, and eight striped 4TB SATA3 hard disks.

performed using the RI approximation unless explicitly stated otherwise (cf. chapter 6).

2.4.1. Resolution of the Identity in Post-HF Calculations

The resolution-of-identity (RI) approximation[83] (sometimes also called density fitting) does usually not reduce the scaling of the computation but reduces the pre-factor in the scaling making it faster. The main idea behind the RI approximation is to express the four-center integrals $(\mu\nu|\kappa\lambda)$ in terms of three-center integrals:

$$(\mu\nu|\kappa\lambda) = \sum_{P,Q}(\mu\nu|P)(P|Q)^{-1}(Q|\kappa\lambda), \tag{2.64}$$

where P and Q are functions from some *auxiliary* basis set. Equation (2.64) is a formal insertion of the identity operator which gave this approximation its name. The advantage is that the number of three-center integrals is much lower than the number of four-center

integrals which can therefore speed up the computation (up to the factor of 10 for large basis sets). The RI approximation can be used (and is used) in various computational methods – HF, DFT, and post-HF but its advantages are seen best in the correlated post-HF computations where many integrals need to be evaluated. For example the MP2 energy can be expressed as (with respect to an unrestricted HF reference):[18]

$$E_{\mathrm{MP2}}^{\mathrm{UHF}} = \sum_{\sigma_1,\sigma_2} \sum_{i,a\in\sigma_1} \sum_{j,b\in\sigma_2} t_{ij}^{ab}(ia|jb), \tag{2.65}$$

where σ_1 and σ_2 represent the two spins and the amplitudes t_{ij}^{ab} are given by:

$$t_{ij}^{ab} = \begin{cases} \frac{(ia|jb)-(ib|ja)}{\epsilon_i+\epsilon_j-\epsilon_a-\epsilon_b} & \text{if } \sigma_1 = \sigma_2 \\ \frac{(ia|jb)}{\epsilon_i+\epsilon_j-\epsilon_a-\epsilon_b} & \text{if } \sigma_1 \neq \sigma_2. \end{cases} \tag{2.66}$$

As previously a, b refer to spin dependent virtual MOs and i, j denote the occupied MOs. We can apply the RI approximation to the four-center integrals $(ia|jb)$ to obtain:[18]

$$(ia|jb) \approx (ia|jb)_{\mathrm{RI}} = \sum_P {}^{\sigma_1}B_{ia}^P \, {}^{\sigma_2}B_{jb}^P, \tag{2.67}$$

where B_{ia}^P is defined as

$$B_{ia}^P = \sum_Q (ia|Q)(Q|P)^{-1/2}. \tag{2.68}$$

The energy of the new *approximate* method - RIMP2 is given by:

$$E_{\mathrm{RIMP2}}^{\mathrm{UHF}} = \sum_{\sigma_1,\sigma_2} \sum_{i,a\in\sigma_1} \sum_{j,b\in\sigma_2} (t_{ij}^{ab})_{\mathrm{RI}}(ia|jb)_{\mathrm{RI}}. \tag{2.69}$$

The method would be exact (e.g. the same as the *full* MP2 method) if the auxiliary basis set of functions P and Q in expansion (2.64) would span the same space as the direct product of the original basis set. In practice the auxiliary basis set is smaller and a small error is introduced making the RI approach approximate.

The accuracy of the RI approximation for RIMP2 is given naturally by the value ΔRI:

$$\Delta\mathrm{RI} = |E_{\mathrm{MP2}} - E_{\mathrm{RIMP2}}|, \tag{2.70}$$

where E_{MP2} and E_{RIMP2} stand for the full MP2 and approximate RIMP2 energies, respectively. The development of an auxiliary basis set for lanthanide atoms for computations at post-HF levels of theory is given in chapter 6.

2.5. Vibrational Spectroscopy: Franck-Condon Factors

There are different ways one can model broadening in electronic spectra theoretically. Since the computations provide us with a single energy for each excitation the easiest way to do it is to use broadening by an appropriate Gaussian for each excitation. A more rigorous treatment is obtained via the reflection principle.[84] In this approach the phase space of possible geometries for the studied molecule is sampled first (with molecular dynamics or Monte Carlo methods) and the excitation energies are then computed for many representative geometries. Another option is to use the so-called Franck-Condon principle.
In chapter 5 the phosphorescence spectra of the 4,8,12-trioxa-12cH-dibenzo[cd,mn]pyrene-12c-ylium molecule (from now abbreviated only as TOTA) and lanthanide complexes are discussed. The vibrational structures of the states involved need to be taken into account when computing these spectra. We can therefore make use of the Franck-Condon principle,[85,86] which states that the major contribution to the spectrum comes from the vibrational states involved that overlap the most with the initial state.
The Franck-Condon principle is based closely on the Born-Oppenheimer approximation and can be deduced from considerations about the transition dipole moment $\vec{\mu}$. If we denote the positions of electrons in a molecule with $\mathbf{r}_i$, the electron charge $-e$, and the nuclear positions and charges $\mathbf{R}_j$ and $Z_j e$, respectively, we can write the transition dipole moment as sum of its electronic and nuclear contributions:

$$\vec{\mu} = -e \sum_i \mathbf{r}_i + e \sum_j Z_j \mathbf{R}_j = \vec{\mu}_e + \vec{\mu}_N. \tag{2.71}$$

Since the vibronic state $|\varepsilon\nu\rangle$ is described (within the Born-Oppenheimer approximation) as a product of electronic and vibrational wave function $|\varepsilon\nu\rangle = \psi_e(\mathbf{r};\mathbf{R})\psi_v(\mathbf{R})$ (note the parametrical dependence of the electronic wave function on nuclear coordinates $\mathbf{R}$) we can

express the transition moment between two different states $|\varepsilon\nu\rangle$ and $|\varepsilon'\nu'\rangle$ as:[87]

$$\langle\varepsilon'\nu'|\vec{\mu}|\varepsilon\nu\rangle = \int \psi^*_{\nu'}(\mathbf{R}) \underbrace{\left[\int \psi^*_{\varepsilon'}(\mathbf{r};\mathbf{R})\vec{\mu}_e\psi_\varepsilon(\mathbf{r};\mathbf{R})\mathrm{d}\tau_e\right]}_{=\vec{\mu}_{\varepsilon'\varepsilon}} \psi_\nu(\mathbf{R})\mathrm{d}\tau_N + \int \psi^*_{\nu'}(\mathbf{R})\vec{\mu}_N \underbrace{\left[\int \psi^*_{\varepsilon'}(\mathbf{r};\mathbf{R})\psi_\varepsilon(\mathbf{r};\mathbf{R})\mathrm{d}\tau_e\right]}_{=0} \psi_\nu(\mathbf{R})\mathrm{d}\tau_N, \tag{2.72}$$

where the term in the first bracket can be replaced with a constant $\vec{\mu}_{\varepsilon'\varepsilon}$ that does not depend on the positions of nuclei, which represents an additional approximation. The term in the second bracket is zero due to the orthogonality of electronic states. The transition moment then can be rewritten as:

$$\langle\varepsilon'\nu'|\vec{\mu}|\varepsilon\nu\rangle = \vec{\mu}_{\varepsilon'\varepsilon}\int \psi^*_{\nu'}(\mathbf{R})\psi_\nu(\mathbf{R})\mathrm{d}\tau_N = \vec{\mu}_{\varepsilon'\varepsilon}\, FC(\nu',\nu), \tag{2.73}$$

where $FC(\nu',\nu)$ is the overlap integral between the vibrational wave functions, the so-called Franck-Condon factor. The intensities of vibronic transitions are proportional to $|FC(\nu',\nu)|^2$ and the vibrational wave functions are usually approximated as harmonic oscillators.

In this thesis the HOTFCHT program package[88] is used to compute the Franck-Condon factors and to simulate vibronic spectra.

2.6. Symmetry Measure

The last concept I would like to describe in this chapter is the symmetry characterization of molecules. It is very common in chemistry to describe the coordination sphere of an atom by comparison to an ideal coordination geometry. The basic description of coordination symmetries is an integral part of any introductory general chemistry course. For example we know that compounds of the form ML_4 (where M is a metal and L is ligand) are usually of either tetrahedral shape (e.g. $[MnO]_4^-$) or a square planar shape (e.g. $[PdCl_4]^{2-}$). The ideal 'polyhedra' for four coordinated structures are therefore a tetrahedron and a square. The notion of ideal polyhedra is very useful since it gives us pictures that we are used to work with facilitating our communication. It is however rather seldom that an actual structure

(either experimentally determined or computed) would have exactly the ideal symmetry. Sometimes the structure lies somewhere in between two ideal symmetric geometries and it would be useful to quantify this: e.g. 'how much octahedral' or 'how much prismatic' is the given coordination sphere. In my thesis I used the quantification by calculating the symmetry measure (or shape factor) S[89] that will be explained in the following.

For each possible ideal polyhedron P the value of shape measure $S(\mathrm{P})$ is evaluated as:[89]

$$S(\mathrm{P}) = S(\{A_i\},\{B_i\}) = \min\left[\sqrt{\frac{1}{m}\sum_{i=1}^{m}(A_i - B_i)^2}\right], \tag{2.74}$$

where m is the number of all possible edges in the polyhedron. A_i is the dihedral angle (i.e. angle between normals of adjacent faces) along the ith edge of the observed (experimental or computed) polyhedron and B_i is the dihedral angle along the same edge in the ideal polyhedron. In practice the minimization is carried out by trying all possible orientations for the given (experimental or computed) structure. The result of this procedure is a value of $S(\mathrm{P})$ (in degrees of arc). We can asses the degree of agreement with a given ideal geometry by comparing the calculated shape measures. For example, if we have an experimental geometry and want to compare it to two different ideal polyhedra P_1 and P_2 and calculate values $S(\mathrm{P}_1) = 5°$ and $S(\mathrm{P}_2) = 30°$ we can conclude that the experimental structure is closer to the ideal structure P_1.

The exact forms of the ideal polyhedra depend on the repulsive potential used to optimize them.[89,90] In computations presented in this thesis the shape factors for sixfold-coordinated and eightfold-coordinated atoms were calculated. The ideal polyhedra for sixfold-coordinated atoms were the octahedron (O_h) and the trigonal prism (D_{3h}), while for the eightfold-coordinated atoms the ideal shapes were those of the trigonal dodecahedron (D_{2d}), the square anti-prism (D_{4d}), and the bicapped trigonal prism (C_{2v}).[91]

3. Many-body Effects in Complexes Containing Transition Metals

The electronic structure of transition metals and lanthanides is much more complicated than the electronic structure of main group elements. The unfilled d- and/or f-shells enable the realization of different states for the atoms and also various coordination motives for complexes containing these atoms. This makes them both computationally challenging, as the open shells are much more difficult to model compared to closed shells, and rewarding, as the complex electron structure enables useful properties of these complexes in many applied fields like magnetism, optical devices and catalysis just to name a few.[92–94] Even more functionality can be achieved by incorporating more than one or two metal atoms into the system of interest. If the metal centers work together well better properties may be obtained in terms of higher performance catalysts or more efficient optical devices. The communication and synergy between several metal centers by means of *cooperativity* is the main topic of this chapter. In the first part the term *cooperativity* is defined; in the later parts this definition is used to quantify the effects of respective metal centers on optical properties.

3.1. Definition of Cooperativity

In a common sense cooperativity would manifest between two entities (molecules, processes, people *etc.*) if the final effect of the two entities is more than just the sum of the individual effects.

In chemistry a prominent example from a biochemistry textbook would be the allosteric effect in enzymes:[95,96] Enzyme E has two binding sites S_A and S_B. First substrate A would bind to S_A forming complex P_1 inducing structural changes of the substrate and the binding

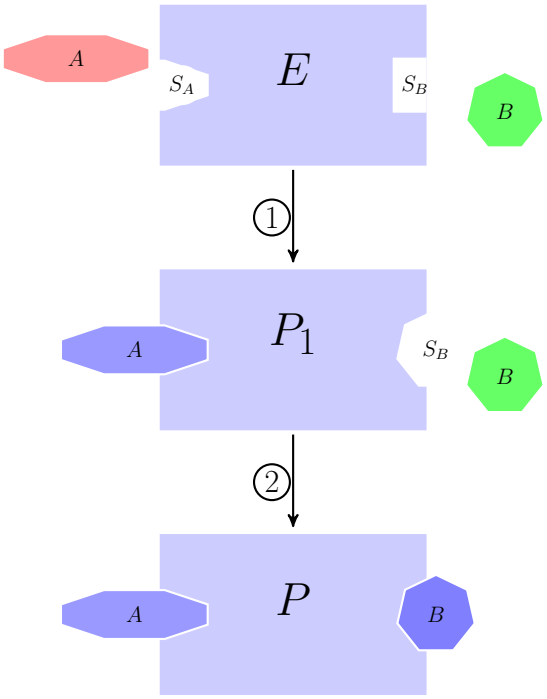

Figure 3.1: An example of cooperativity between substrates A and B in an allosteric catalyzed reaction of an enzyme. See the text for further explanation.

site S_B in particular. The second substrate B could then bind with P_1 forming the final product P. It is straightforward to see that the reaction would not occur if only substrate A or only substrate B would be present; the reaction shows therefore cooperativity between A and B (where the aforementioned sum of effects in this extreme case is zero as no reaction would occur). The whole mechanism is shown schematically in Figure 3.1. With this reasoning one can easily imagine catalysis in general being a highly cooperative process.

These natural definitions are however not always sufficient for our purposes especially if we would like to quantify these effects. It is therefore useful to have a mathematical definition of cooperativity. Let us have two systems – an initial system A and a target system B each of which consists of several subsystems A_i and B_j. We are interested in the cooperativity in system A (i.e. between different parts A_i); we want to see how much the properties differ when subparts of A are replaced by subparts of B which are chemically similar but not identical. Since we want to know how a part contributes to the whole system we make use of a differential many-body expansion:

$$\Delta O = \sum_k \Delta O_k + \sum_{k<l} \Delta O_{kl} + \sum_{k<l<m} \Delta O_{klm} + \cdots , \tag{3.1}$$

where ΔO is a difference in some property between systems A and B. This definition is general and O can stand for any property, e.g. energy, dipole moment, polarizability, or anything else. According to equation (3.1) we can expand this difference as a sum of one-body contributions ΔO_k, two-body contributions ΔO_{kl}, three-body contributions ΔO_{klm}, and higher-body contributions. The one-body contributions ΔO_k can be calculated from mixed systems where the kth subsystem of A is substituted by the kth subsystem of B (see also section 3.2). Two-body contributions stem from mixed complexes where the kth and the lth subsystems are substituted and so on. A detailed calculation of different n-body contributions to ΔO for a complex with three metal centers is shown in section 3.2.
Cooperativity is involved if a property of a system is determined by more than pairwise contributions[97] and is therefore expressed by the three- and higher-body contributions (cf. equation (3.1)). At this point it is useful to note that the many-body expansion is often used to reduce computational costs in partitioning schemes, i.e. higher order terms are calculated at lower level of theory.[98] This is, however, not the case here; we use the expansion only for a consistent definition of cooperativity.
With this definition at hand we can now turn to different metal containing complexes and try to analyze whether the metal centers act cooperatively or not.

3.2. Cooperativity in Complexes with Three Metal Centers

In this section two trinuclear metal complexes will be studied. To apply the differential many-body expansion to trinuclear metal complex we first define a *parent* complex XXX and a *target* complex YYY where X and Y denote different metals. One can obtain the target complex from the parent complex by replacing all X metal centers by Y metal centers. Of course one can also make a mixed complex with one X and two Y metals and vice versa. In general (i.e. unless the metals are equivalent due to symmetry) six mixed complexes can be made (XXY, XYX, YXX, XYY, YXY, YYX). We can now expand the difference

between parent and target complex in any given property ΔO according to (3.1) as:

$$\begin{aligned}\Delta O &= O(\mathrm{YYY}) - O(\mathrm{XXX}) \\ &= \sum_{k=1}^{3} \Delta O_k + \sum_{l=2}^{3} \sum_{k=1}^{l-1} \Delta O_{kl} + \Delta O_{123} \\ &= \Delta O_1 + \Delta O_2 + \Delta O_3 + \Delta O_{12} + \Delta O_{13} + \Delta O_{23} + \Delta O_{123}, \end{aligned} \tag{3.2}$$

where the one-body terms are given by:

$$\Delta O_1 = O(\mathrm{YXX}) - O(\mathrm{XXX}), \tag{3.3}$$

$$\Delta O_2 = O(\mathrm{XYX}) - O(\mathrm{XXX}), \tag{3.4}$$

$$\Delta O_3 = O(\mathrm{XXY}) - O(\mathrm{XXX}), \tag{3.5}$$

the two-body terms are given by:

$$\Delta O_{12} = O(\mathrm{YYX}) - O(\mathrm{XXX}) - \Delta O_1 - \Delta O_2, \tag{3.6}$$

$$\Delta O_{13} = O(\mathrm{YXY}) - O(\mathrm{XXX}) - \Delta O_1 - \Delta O_3, \tag{3.7}$$

$$\Delta O_{23} = O(\mathrm{XYY}) - O(\mathrm{XXX}) - \Delta O_2 - \Delta O_3, \tag{3.8}$$

and the three-body term is given by:

$$\begin{aligned}\Delta O_{123} &= \Delta O - \sum_{k=1}^{3} \Delta O_k - \sum_{l=2}^{3} \sum_{k=1}^{l-1} \Delta O_{kl} \\ &= O(\mathrm{YYY}) - O(\mathrm{XYY}) - O(\mathrm{YXY}) - O(\mathrm{YYX}) + \\ &\quad O(\mathrm{YXX}) + O(\mathrm{XYX}) + O(\mathrm{XXY}) - O(\mathrm{XXX}). \end{aligned} \tag{3.9}$$

Equation (3.9) allows us to calculate cooperativity in different trinuclear complexes. One just needs to calculate the property of interest (e.g. the energy) for the parent, the target, and all mixed complexes and evaluate ΔO_{123}. Its size then directly determines the extent of cooperativity between metal centers in the complex.

3.2.1. Cooperativity in a Pd/Pt Complex

First we apply this procedure to a homotrinuclear Pd complex $[Pd_3\{Si(mt^{Me})_3\}_2]$ where mt^{Me} is methimazole. This complex has D_3 symmetry and its photophysical properties in the ground and excited states have already been studied extensively both experimentally and theoretically.[99,100] The structure of the complex is shown in Figure 3.2. The cooperativity between the metal centers can be investigated by sequentially replacing the Pd atoms by Pt atoms (an element from the same group in the periodic table). We define the Pd_3 complex as the *parent* complex and the Pt_3 complex as the *target* complex.

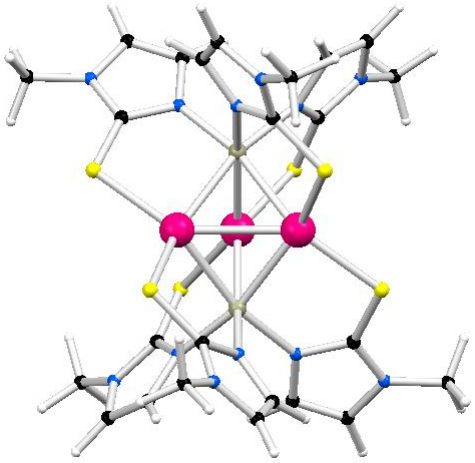

Figure 3.2: Structure of $[Pd_3\{Si(mt^{Me})_3\}_2]$ where mt^{Me} is methimazole calculated at the BP/def2-TZVPP level of theory: Pd – magenta, H – white, C – black, N – blue, S – yellow, Si – tan.

The structures of all necessary complexes were optimized using DFT with the BP functional[41] using the def2-TZVPP basis set[101,102] as implemented in the TURBOMOLE program package. The resolution-of-identity was used in all calculations and the convergence criteria were $10^{-8}\,E_h$ and $10^{-5}\,E_h/a_0$ for the SCF energy and Cartesian gradient respectively. After optimization a single point energy calculation at the B3LYP/def2-TZVP[44] level was performed.[103]

The properties of interest are the electronic energy, the UV/vis spectrum, and the transition

Table 3.1: Differential many-body decomposition of the energy of the Pd_3/Pt_3 complex. All geometry optimizations have been performed at the BP/def2-TZVPP level of theory. Energies are given in kJ/mol. Data taken from Ref. [103].

Method	Geometry	$\Delta O^{(1)}$	$\Delta O^{(2)}$	ΔO_{123}
BP/def2-TZVP	Optimized	67.1×10^3	6.2	0.9
B3LYP/def2-TZVP	Optimized	67.4×10^3	7.4	1.3
B3LYP/def2-TZVP	Fixed at Pt_3 geometry	67.4×10^3	6.8	0.1

density. For clarity one can define a sum of one-body and two-body terms of equation (3.1):

$$\Delta O^{(1)} = \sum_{k=1}^{3} \Delta O_k, \tag{3.10}$$

$$\Delta O^{(2)} = \sum_{l=2}^{3} \sum_{k=1}^{l-1} \Delta O_{kl}. \tag{3.11}$$

The results of the differential many-body decomposition of the electronic energy are summarized in Table 3.1. We investigated both the effect of method by comparing two functionals and the effect of geometry by taking the complexes either optimized in their respective minimal structure or fixed at the geometry of Pt_3 complex minimum. In all cases the one-body part dominates, i.e. the major difference in electron energy comes directly from the difference between electron energies of Pd and Pt – the difference of absolute electronic energies of Pd and Pt at the B3LYP/def2-TZVP level is about 22.6×10^3 kJ/mol. Given the fact that both two-body and three-body effects are very small, one can conclude that there is no cooperativity in terms of energy in these complexes. This is not surprising as the energy difference between electronic energies of different elements will always play the most important role. More chemically relevant information could be obtained from the decomposition of i.e. atomization energies.

The cooperative effects in the UV/Vis spectrum of the complex can also be studied. In order to simulate the absorption spectrum it is necessary to first calculate excited states of the molecule which can be done in different ways. For this relatively large molecule the simplified TDDFT method[62] was the best choice. One needs to keep in mind that we are primarily interested in *differences* between spectra of similar molecules and the agreement with experimental spectra (if they are available at all) is not the primary goal of these

computations. The pragmatic way of calculating the spectra at the same level of theory for all complexes was therefore the use of the B3LYP/def2-TZVP molecular orbitals as inputs for sTDDFT computation.

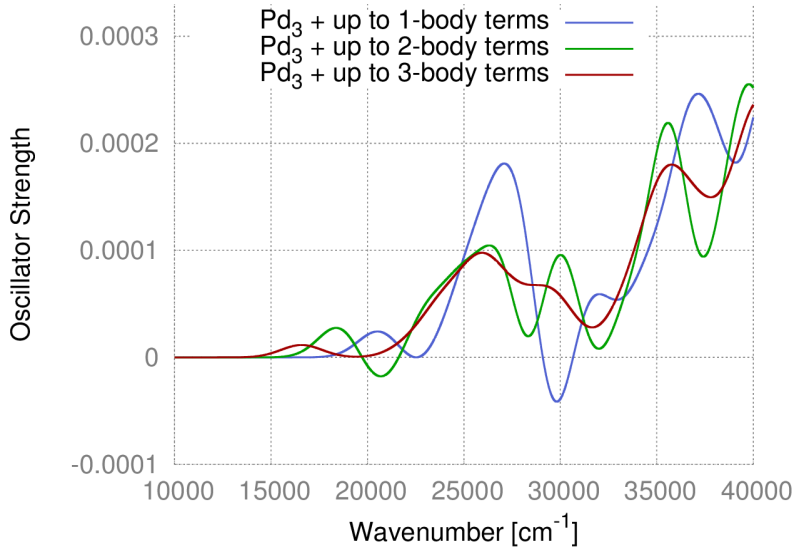

Figure 3.3: Computed UV/Vis spectrum of the Pt_3 complex (red curve) compared to when three-body terms (green curve) and two- and higher-body terms (blue curve) are omitted. The calculations were performed with the sTDDFT method using B3LYP/def2-TZVP molecular orbitals and orbital energies. Reprinted with permission from Ref. [103]. Copyright 2016 John Wiley and Sons.

Absorption spectra obtained from such computations are presented in Figure 3.3. It is possible to get the spectrum of the target complex (Pt_3, red curve) by adding the one-, two- and three-body terms to the spectrum of the parent complex (Pd_3). If three-body terms are omitted (green curve) the first absorption band around 25000 cm^{-1} is reproduced and so is the second band around 35000 cm^{-1} even though the intensity already differs. Furthermore, many additional features appear in the spectrum without three-body term making it qualitatively different from the full spectrum. If only one-body terms are taken into account (or from the opposite perspective also two-body terms are omitted) the spectrum differs even more (blue curve); the maxima are shifted and differences in the intensities are significant. As just concluded there is a substantial difference between the full spectrum and a spectrum omitting the three-body term. Hence the three-body term is also important and cooperativity between the metal centers plays a major role in the UV/Vis spectrum of the Pd_3/Pt_3

complexes. The metal atoms are quite close to each other – the distance between them in the computed structures is $\approx 2.8\,\text{Å}$ – and can therefore interact strongly.

3.2.2. Cooperativity in a Rh/Ir Complex

The second trimetallic complex that was studied is the tritopic triphenylene-based N-heterocyclic carbene with three Rh atoms (parent complex) or three Ir atoms (target complex). Its structure is depicted in Figure 3.4. The chlorine atoms can be either above or below the plane of the central condensed aromatic system and the *tert*-butyl groups on the nitrogen atoms prevent the cycloocta-1,5-diene groups from rotating. The structure is therefore fixed in the *up – up – down* configuration with respect to the chlorine atoms. The metals are much further away from each other ($\approx 13.5\,\text{Å}$) than in the case of the Pd/Pt complex and can only interact via the aromatic center of the molecule.

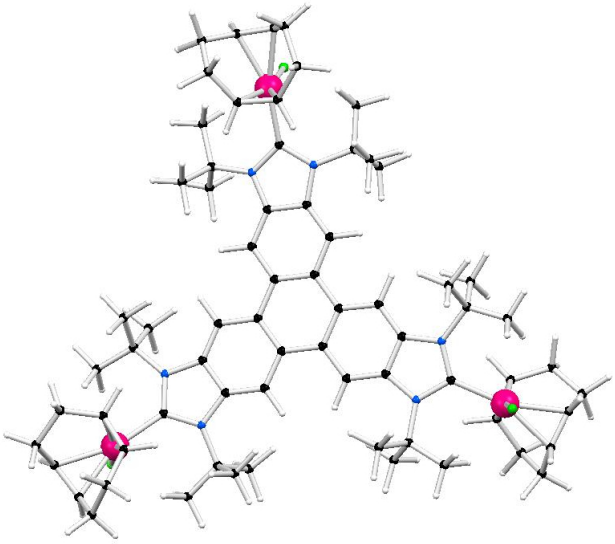

Figure 3.4: Structure of the tritopic triphenylene-based N-heterocyclic carbene with three Rh atoms obtained at the BP/def2-TZVPP level of theory: Rh – magenta, H – white, C – black, N – blue, Cl – green.

At first one can again apply the differential many-body expansion to the energy. The results, presented in Table 3.2, show again that the largest contribution to the electronic energy can be attributed to the one-body terms. Two- and higher-body terms are very small and negligible especially when the geometry is fixed at the target complex geometry. Comparing the results obtained for the electronic energies for Pd/Pt and Rh/Ir complexes

Table 3.2: Differential many-body decomposition of the Rh_3/Ir_3 complex. All geometry optimizations were performed at the BP/def2-TZVPP level of theory. Energies are given in kJ/mol. Data taken from Ref. [103].

Method	Geometry	$\Delta O^{(1)}$	$\Delta O^{(2)}$	ΔO_{123}
BP/def2-TZVP	Optimized	48.6×10^3	-0.24	0.05
B3LYP/def2-TZVP	Optimized	48.9×10^3	-0.21	0.04
B3LYP/def2-TZVP	Fixed at Ir_3 geometry	48.9×10^3	$< 0.5 \times 10^{-3}$	$< 0.5 \times 10^{-3}$

one may expect the latter to have smaller cooperativity than the former even in the UV/Vis spectra. This is in agreement with purely geometrical considerations – communication in the Rh/Ir complex is only possible via the central part of the ligand and not directly as in the Pd/Pt complex. Indeed, lower cooperativity in the spectra is observed in this case as one can see in Figure 3.5. In the case of the Rh/Ir complex even one-body terms are enough to capture the two main absorption bands the only difference being in intensity. If two-body terms are included the spectrum is reproduced almost perfectly. This shows then again that little to no cooperativity is found between the metal centers in the Rh/Ir complex.

This may also have some exploitable implications. If we are in a situation that we had already calculated the spectrum of the Rh_3 complex and wanted to calculate the spectrum of the Ir_3 complex we could only replace one metal atom in the (almost symmetric) structure, do the calculation and would have a very good estimate of the desired spectrum. The calculation with only one different metal could be arguably cheaper than a calculation of a fully substituted complex because the number of electrons involved would be lower.

The parent (Rh_3) and target (Ir_3) complexes were also synthesized and their spectra measured experimentally.[103] Figure 3.6 shows how the experimental spectra compare to the calculated ones. First one notes that in the experiment both peaks – the first at $\approx 27000\,\mathrm{cm}^{-1}$ and the second at $\approx 33000\,\mathrm{cm}^{-1}$ – are shifted to lower energies in the Ir_3 spectrum compared to the Rh_3 spectrum. The calculated spectra reproduce qualitatively the peak around $\approx 33000\,\mathrm{cm}^{-1}$ and in the case of Ir_3 even the lower energy peak. The earlier offset of the calculated spectrum of the Ir_3 complex with respect to the calculated spectrum of the Rh_3 complex is also in agreement with experiment. The agreement of the computations and experiment is not excellent, the main differences stemming from solvent effects (the exper-

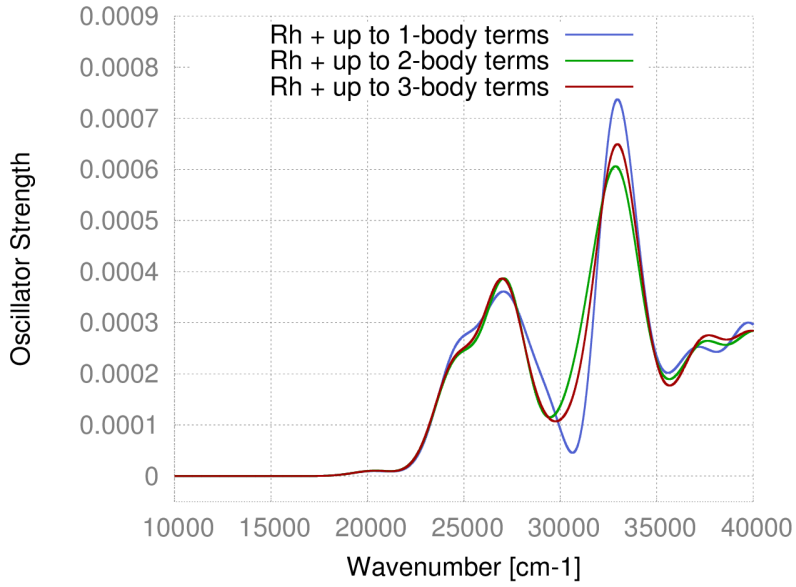

Figure 3.5: Computed UV/Vis spectrum of the Ir_3 complex (red curve) compared to when three-body terms (green curve) and two- and higher-body terms (blue curve) are omitted. The calculations were performed with the sTDDFT method using B3LYP/def2-TZVP molecular orbitals and orbital energies. Reprinted with permission from Ref. [103]. Copyright 2016 John Wiley and Sons.

imental spectrum was recorded in a solution, while the computations are performed on an isolated complex in the gas-phase), dynamical effects (only one conformer of the molecule is taken into account in the calculation) and, of course, the (rather severe) approximations made for the computation of excited states with the sTDDFT method itself. Nevertheless the accordance is satisfactory enough to justify the use of the many-body expansion computations for these systems.

Another interesting property one can look at is the transition density. For each excitation the natural transition orbitals (NTOs) can be determined and a transition density matrix $\boldsymbol{\rho}$ can be constructed:[103,104]

$$\boldsymbol{\rho} = \boldsymbol{V}\boldsymbol{N}^2\boldsymbol{V}^T - \boldsymbol{O}\boldsymbol{N}^2\boldsymbol{O}^T, \tag{3.12}$$

where $\boldsymbol{V}$ and $\boldsymbol{O}$ matrices contain the particle and hole NTOs, respectively, and, together with the diagonal matrix $\boldsymbol{N}$, they can be calculated via a singular-value decomposition of the excitation vector $\vec{X}$. I will look into the three lowest excitations in our complexes,

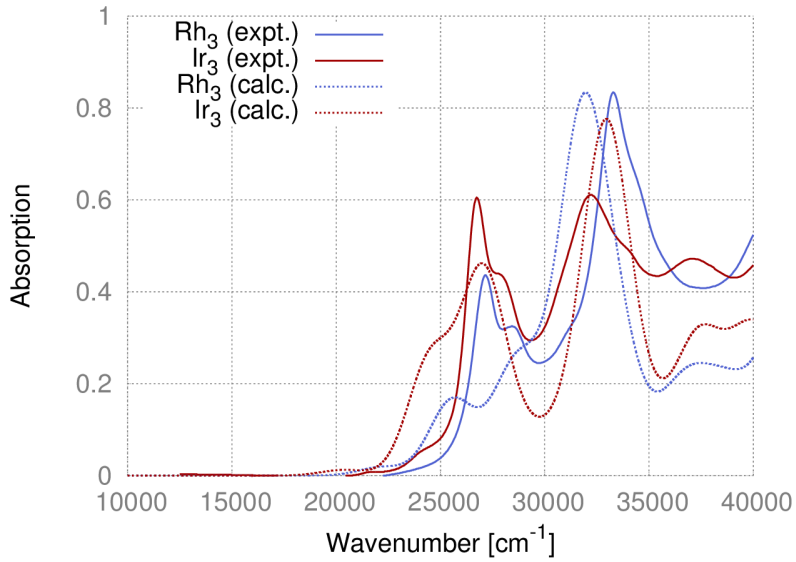

Figure 3.6: Experimental UV/Vis spectra of Rh_3 and Ir_3 complexes with the respective calculations. The calculations were performed with the sTDDFT method using B3LYP/def2-TZVP molecular orbitals and orbital energies. Calculated spectra are scaled in order for the highest peaks of experimental and calculated spectra of Rh_3 complex to have the same intensity. Reprinted with permission from Ref. [103]. Copyright 2016 John Wiley and Sons.

which yield the total transition density matrix $\boldsymbol{\rho}_{\text{total}}$:

$$\boldsymbol{\rho}_{\text{total}} = \sum_{i=1}^{3} \boldsymbol{\rho}(\omega_i). \tag{3.13}$$

Due to (3.13) it is possible to apply the differential many-body expansion to the difference of total transition densities for the Rh_3 and Ir_3 complexes using a grid representation of the density. The visualization of such a procedure is shown in Figure 3.7. Similarly to the case of the UV/Vis spectrum the total transition density is very well reproduced already by including the one-body terms and the error in this case is small (see Figure 3.7 center, note the two orders of magnitude difference of the displayed isovalue). The three-body term and therefore the cooperativity in this case is again very small.

In this chapter two pairs of complexes were studied. For the first time the differential many-body expansion was used to study trinuclear metal clusters. We saw one example of strongly interacting cooperative metals in the case of the Pd_3/Pt_3 complexes and one example of

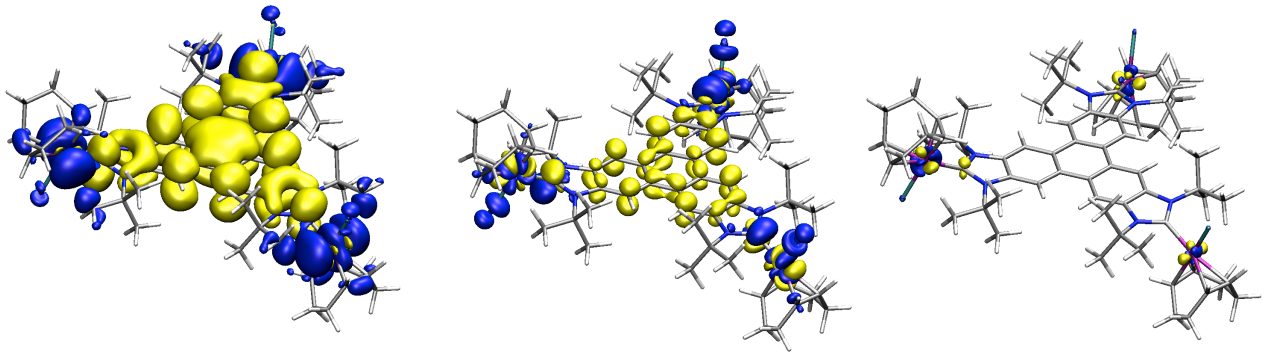

Figure 3.7: Transition densities of the Ir_3 complex obtained for the lowest three excitations using the sTDDFT method (B3LYP/def2-TZVP). Yellow corresponds to a gain and blue to a loss of electron density. The total transition density (left; isovalue $\pm 1 \times 10^{-3} a_0^{-3}$). Error in the total transition density when only one-body terms are taken into account (center; isovalue $\pm 1 \times 10^{-5} a_0^{-3}$). Three-body contribution to the total transition density (right; isovalue $\pm 5 \times 10^{-7} a_0^{-3}$). Reprinted with permission from Ref. [103]. Copyright 2016 John Wiley and Sons.

weakly interacting metals in the Rh_3/Ir_3 complexes with almost no cooperative effects. The difference between the two cooperativities was best seen in the UV/Vis absorption spectra calculated for the complexes. The reason for different cooperativities is the proximity or the remoteness of the metal atoms with respect to each other with closer Pd_3/Pt_3 atoms displaying much higher cooperativity.

4. Fluorescence of Complexes Containing Europium

The last chapter focused on a theoretical concept applied to a real complex to retrieve some highly abstract quantity such as cooperativity. The methods of theoretical chemistry can however also be used more directly, e.g. to estimate geometries, reaction or excitation energies, dipole moments, magnetic properties, and many other quantities. In the end of the day it is the combined effort of theory and experiment that helps us understand the world around us. Thus, one of the main ways theoretical chemistry can contribute is to help to interpret the results of experiments and it is important to bear in mind that both theory and experiment are of key importance here. They can both answer different questions, have different advantages and weaknesses and it is the combination of the two that shows the most complete picture. In this chapter I will show an example of such a combined effort in investigating a group of europium containing complexes. We will see how both theory and experiment contribute with interpretations and new suggestions to research.

As it was already mentioned in the introduction lanthanide ions in organic complexes can have very interesting and useful optical properties which make them suitable materials for optical devices. In the framework of cooperativity presented in the previous chapter an interesting device could be a quantum cutter – a device able to 'cut' an absorbed photon of high energy (in UV range) into two photons of lower energy (in Vis or IR range) that would be emitted. Such devices could be used in conventional lighting devices or photovoltaics.[16] The work presented in this chapter is concerned with molecular properties and studies in detail the structure, energy levels, energy transfer, and luminescence in complexes that contain europium. The experiment is performed in the gas-phase so that environment effects (such as stacking in crystals or solvent effects in solutions) are eliminated and the direct comparison to the computational results is facilitated. This work is also part of a

series of studies that deal with structurally different lanthanide complexes.[105]

4.1. Systems of Interest

This chapter is concerned with complex molecules that contain at least one europium atom and several 9-oxo-phenalen-1-one (PLN) ligands. The PLN ligand is a β-diketonate of phenalene, an aromatic hydrocarbon consisting of three condensed benzenes. The structure of PLN is shown in Figure 4.1. This ligand is chosen for structural and energetic reasons – the β-diketonates in general have the ability to bridge different metal centers which is important for the stability of the complex; the energetic reasons and its importance are apparent from the process that we want to describe.

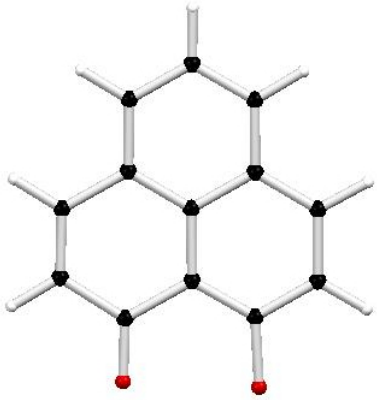

Figure 4.1: Illustrative structure of 9-oxo-phenalen-1-one (PLN).

The process itself may be summarized as follows:[105] first the ligand is excited to the singlet S_1 state by irradiation with UV light; then an intersystem crossing in the ligand takes place and the lowest lying triplet T_1 state is populated; then energy transfer occurs from the ligand to the europium center (i.e. the metal center) and the excited $^5D_0$ level of europium is populated; finally the luminescence from the $^5D_0$ state to the ^7F ground state manifold of europium is measured. Note that the f-shell of Eu^{3+} is localized due to the effective shielding by $5s$ and $5p$ electrons which allows the use of the atomic term symbols in the process description. The whole process is shown schematically in Figure 4.2. The experimental evidence of this process, which is measured, is the final luminescence of the europium atom. From this description it is obvious that the ligand needs to have suitable energetic properties namely the triplet state T_1 needs to lie just above the $^5D_0$ state of

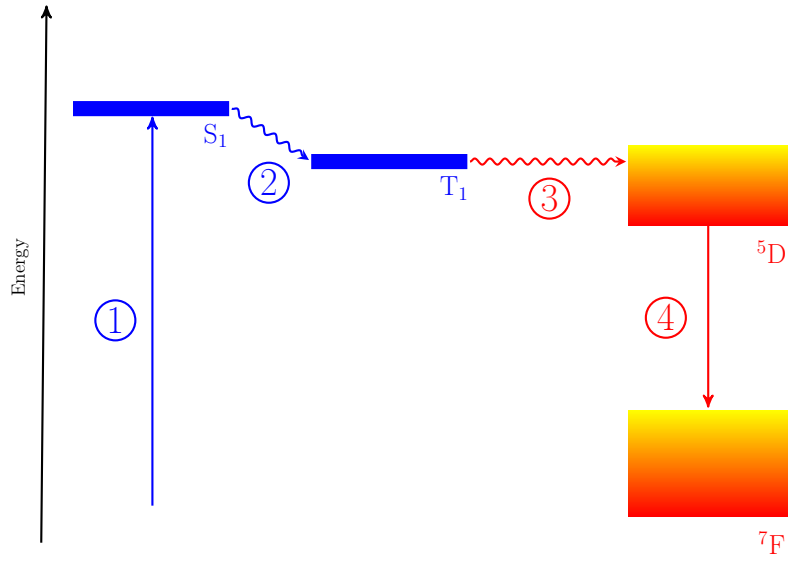

Figure 4.2: The sensitization of europium in the complexes studied. The process takes place partly in the ligand (blue) and partly in the europium ion (red). The steps include excitation (1), inter-system crossing (2), energy transfer from ligand to metal (3) and the experimentally measured and calculated luminescence (4). The Eu^{3+} f-shell is well localized due to the effective shielding by $5s$ and $5p$ electrons which allows the use of atomic term symbols in the graphic. The figure is illustrative and not in scale.

europium (which has an energy of about 17250 cm^{-1})[106] in order to allow efficient energy transfer to take place. Since PLN has both desired properties – it forms stable complexes with europium and its T_1 state is of favorable energy[107] – it is a suitable ligand for this kind of study. I will however also briefly discuss some other possible ligands in section 4.1.1. There are two types of complexes that we will be concerned with in this chapter. First is the nonanuclear complex $[Eu_9(PLN)_{16}(OH)_{10}]^{+}$[108] that is referred to simply as 'nonanuclear europium complex' in the following. The second type of complexes are adducts of europium, four PLN ligands and an alkaline earth metal AE: $[Eu(PLN)_4AE]^{+}$,[109] where AE = Mg, Ca, and Sr. I will call this series of structures 'four ligand systems'. The motivations for studying these two systems are a bit different and will be explained later. At this point let us only stress that the general sensitization and luminescence process as described in this section is the same for both of them.

4.1.1. Alternative Ligands

Apart from the PLN molecules I also performed a screening of other possible ligands. I focused on computing S_0–T_1 energy differences for these molecules by different methods including CIS and ΔSCF (i.e. computation of the two states of different multiplicity and making a difference of the energies) of DFT states with the BP and B3LYP functionals. None of the methods I tried provided, however, reliable data for the S_0–T_1 energy difference which, together with the lack of experimental data, proved to be limiting for drawing conclusions and suggesting ligands for our application other than PLN.

I tested a set of 36 molecules – 17 of them were derivates of PLN and 8 were derivates of anthracene or its heterocyclic analogs. The rest of the set studied were smaller aromatic organic molecules usually containing two benzene rings. In the desired application in the europium centered complex the ligands should be negatively charged to compensate for the positive charge of the Eu^{3+} ion. In most cases, the suggested molecules create anions upon loosing the acidic hydrogen of the alcohol OH group. The complete list of molecules tested is given in Appendix B.

An ideal ligand for our application would have the S_0–T_1 gap slightly larger than PLN (which is also ligand labeled 1 in this set of molecules) as the efficient energy transfer to the europium center would still be possible. Additionally such a ligand could also be used in complexes with different lanthanides, e.g. Tb^{3+}. The results for the ΔSCF computation at the B3LYP/def2-TZVPP level of theory are presented in Figure 4.3. As one can see many ligands have excitation energies close to those of PLN which is especially true for derivates of PLN and only a few ligands have higher excitation energies. For example tropolone (ligand 19) would be a good candidate, the synthesis of the corresponding complex was however not attempted.

Additionally the simplified TDA method[60] was compared with the full TDA approach in the computation of the first excitation energies of the possible ligands. Both singlet excitation and triplet excitation were computed. The results presented in Figure 4.4 show that the sTDA method always underestimates the singlet excitation by $\approx 0.2\,\text{eV}$. The triplet excitations however are overestimated and generally the agreement between the two methods is worse. We can conclude that even though the sTDA/sTDDFT method was primarily developed to compute absorption spectra of large molecules the individual

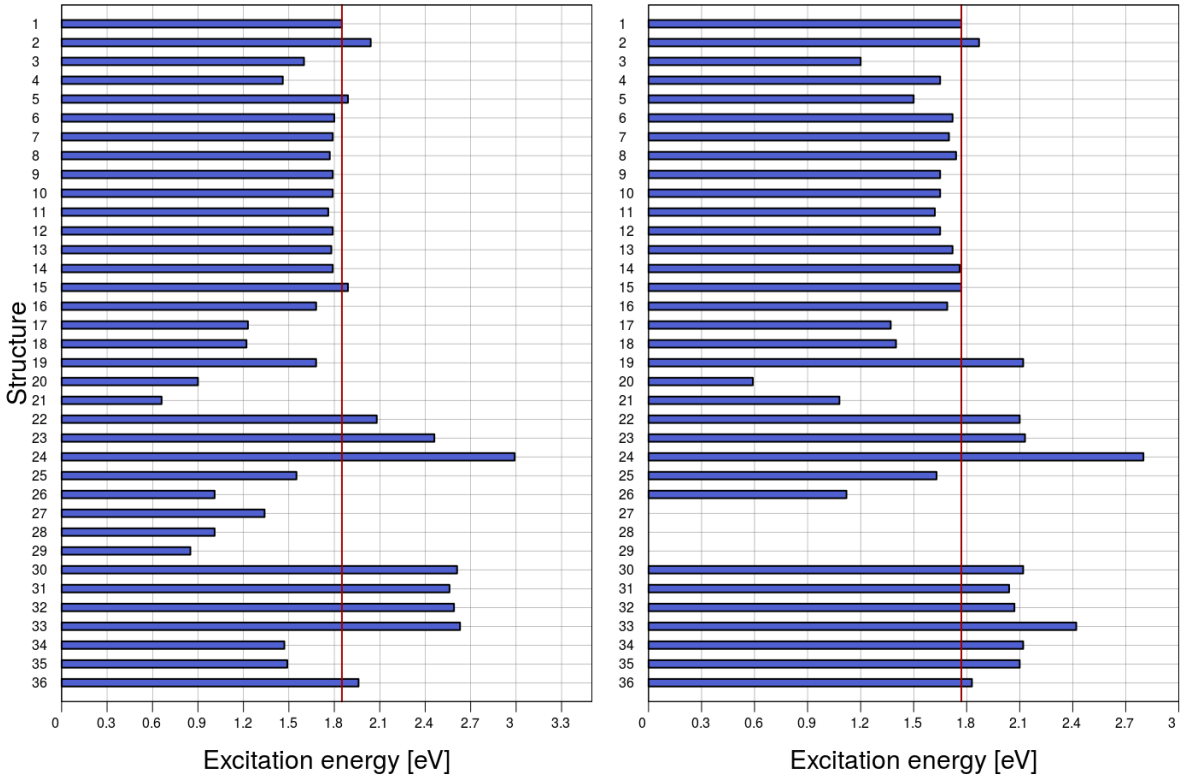

Figure 4.3: Excitation energies in possible ligand molecules calculated as a difference of the S_0–T_1 states using the B3LYP/def2-TZVPP method computed at the T_1 equilibrium geometry. The results for neutral structures (left) and anions (right) are presented. The values for PLN (structure 1) are highlighted with the red line. The list of structures is given in Appendix B. Note that no suitable anion structures were found for structures 27, 28, and 29.

excitations also agree reasonably well with the full TDA computation especially in the case of singlet excitations.

Given the lack of experimental data and the general uncertainties in computations of DFT excitations we concluded the best option is to use the original PLN ligand. Having mentioned possible alternatives to PLN in europium complexes we turn our attention now to how we can describe the luminescence of such complexes theoretically.

4.2. Computational Protocol

The procedure that was used to calculate the energies of transitions in europium containing complexes can be divided into two main blocks that are described in the following

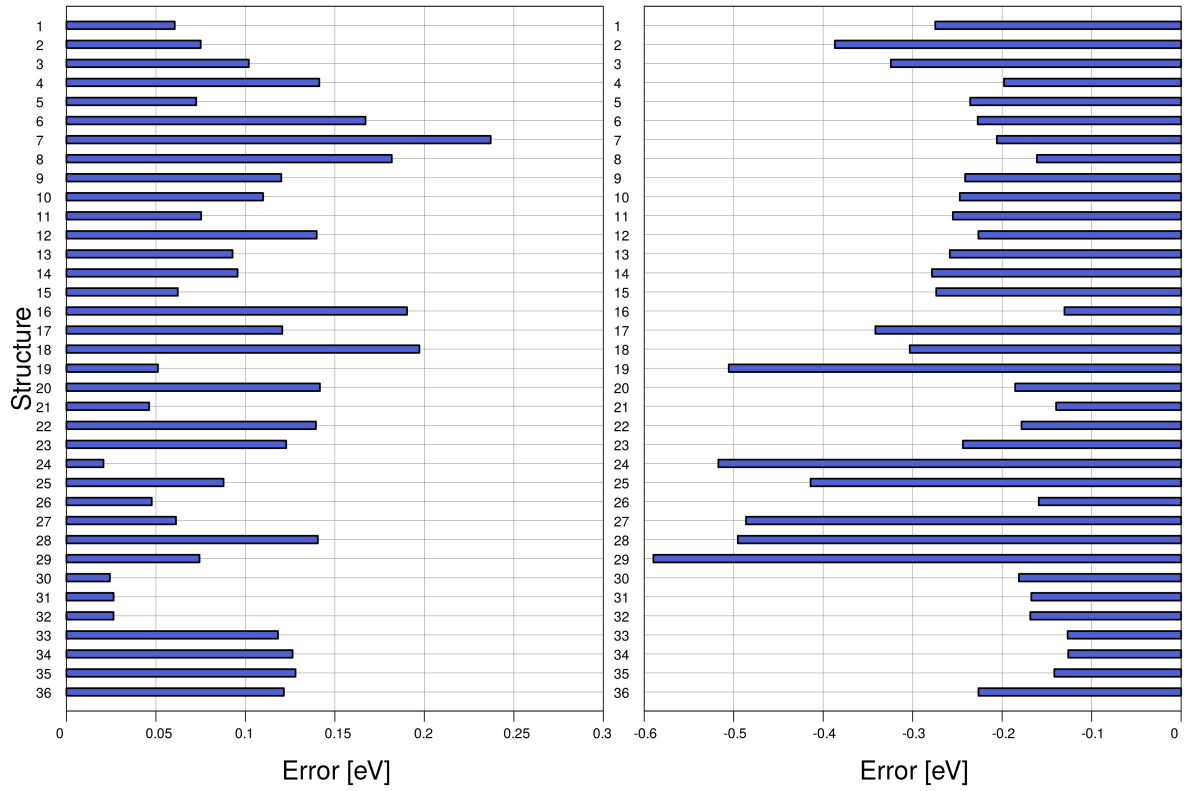

Figure 4.4: The error $\Delta E = E_{\mathrm{TDA}} - E_{\mathrm{sTDA}}$ for the neutral structure of alternative ligands computed at the B3LYP/def2-TZVPP level of theory for the first singlet S_1 (left) and triplet T_1 (right) excited states. Note that the singlet excitation energies are underestimated while the triplet excitation energies are overestimated by the sTDA method. The list of structures is given in Appendix B.

subsections.

4.2.1. Geometry Optimization

In order to calculate the splitting of f-electron energy levels in Eu^{3+} in a given complex the geometry of the complex needs to be determined first. The complexes of interest are quite large with 381 and 90 atoms for the nonanuclear europium complex and the four ligand system, respectively, which translates to $\approx$ 10300 and 2400 valence basis functions, respectively (with a def2-TZVPP basis set). The geometry optimization with DFT is therefore the only viable option in this case. In principle one should optimize the excited molecule where europium is in the emitting ^{5}D state. It was shown however that the latter state has a strong multi-reference character; moreover the difference in geometry between

the ^{5}D state and the ^{7}F ground state is quite small.[105] Since the ground state can be described well with a single determinant the geometry optimizations were carried out in the ground state.

Following the experience from the study of adducts of the form $[Eu(PLN)_3A]^+$, where A = Li, Na, K, Rb, or Cs[105] ('three ligand systems') the initial structures were obtained using the PM6-SPARKLE method.[110] These were subsequently optimized in TURBOMOLE using the BP functional first with the def2-SVP and then with the def2-TZVPP basis set. The energy thresholds were set to $10^{-8}\,E_\mathrm{h}$ and $10^{-5}\,E_\mathrm{h}/a_0$ for the SCF energy and Cartesian gradient respectively. The resolution-of-identity approximation was used in all computations. In all cases the harmonic frequencies were calculated using the `aoforce` module of TURBOMOLE to check if the geometries are true (local) minima (and not saddle points) on the potential energy surface. The parallel implementations of TURBOMOLE were used heavily for these calculations (the MPI[111] and fork[112] parallelizations).

4.2.2. Ligand Field Splitting Computations

With the geometries at hand we can now calculate the splitting of the $4f^6$ levels of europium. This is done using the effective Hamiltonian $\hat{H}_\mathrm{eff}$ implemented in the McPHASE program,[76] which was already described in detail in section 2.3.3. Here I only remind that the effective Hamiltonian consists of three parts:

$$\hat{H}_\mathrm{eff} = \hat{H}_\mathrm{C} + \hat{H}_\mathrm{SO} + \hat{H}_\mathrm{LF}, \tag{4.1}$$

where $\hat{H}_\mathrm{C}$, $\hat{H}_\mathrm{SO}$, and $\hat{H}_\mathrm{LF}$ represent Coulomb, spin–orbit, and ligand field interactions, respectively.

The charge distribution in the complex is needed for setting up the ligand field Hamiltonian. A standard procedure to determine the charge distribution in a molecule is to do a population analysis that yields the distribution of electrons among atoms. There are several ways how the population analysis can be done and none of them is the best for all purposes.[113] After some testing the natural population analysis (NPA)[114] was chosen. The obtained charges on europium were adjusted to 3+ and (in case of the four ligand systems) the charges on the alkaline earth metals were adjusted to 2+. Then I scaled the charges on the oxygen atoms so that the total charge of the molecule (i.e. 1+) was retained.

The effective Hamiltonian also contains four adjustable parameters that were obtained by fitting to experimental results – three Slater integrals F^2, F^4, and F^6 as well as a spin–orbit scaling factor ζ. These parameters will be of interest in the next section.

4.3. Nonanuclear Europium Complex and Parameter Fit

The emission spectrum for the nonanuclear europium complex was measured experimentally and is shown in Figure 4.5. The transitions are well resolved and this therefore seems to be a perfect example to test our computational protocol.

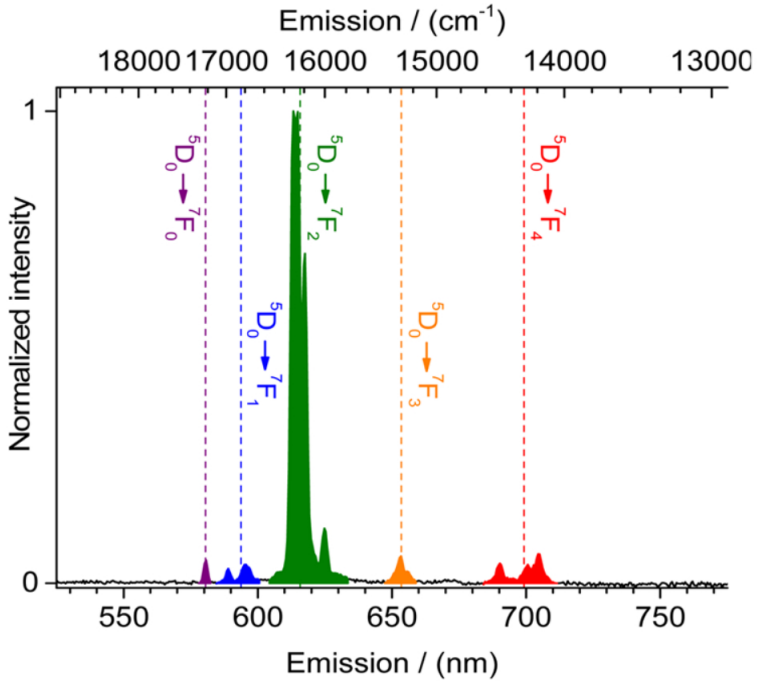

Figure 4.5: Experimental gas-phase emission spectrum of the observed $^5D_0 \rightarrow ^7F_J$ transitions of the nonanuclear europium complex with $J = 0, 1, 2, 3,$ and 4. Reprinted with permission from Ref. [115]. Copyright 2016 American Chemical Society.

One geometry was obtained, which is depicted in Figure 4.6. In this structure one europium atom is located in the center while the other eight europia form a cage around it. The outer lying europium atoms are coordinated by eight oxygens each. In order to further characterize the local coordination of the europium atoms we made use of the shape measure S[89] as described in section 2.6. Note that for the eight-coordinated system the ideal geometries are the trigonal dodecahedron (D_{2d}), the square antiprism (D_{4d}), and the

bicapped trigonal prism (C_{2v}). First I calculated the shape of the coordination sphere of the outer europia around the central europium; this resembles the square antiprism the most with the shape measures $S(D_{4d}) = 5°$, $S(C_{2v}) = 14°$, and $S(D_{2d}) = 16°$. Due to its close to local D_{4d} symmetry the central europium atom will not be contributing to the emission spectrum in this complex. The shape measure analysis of the outer europia however show that the symmetry of their coordination spheres (with eight coordinating oxygens for each europium) are close to the bicapped trigonal prism with the shape measures $S(C_{2v}) \approx 8°$, $S(D_{2d}) \approx 14°$, and $S(D_{4d}) \approx 16°$. Since the distribution of the shape measures differs only slightly for the eight outer europia it is assumed that they all contribute to the emission spectrum equally.[115]

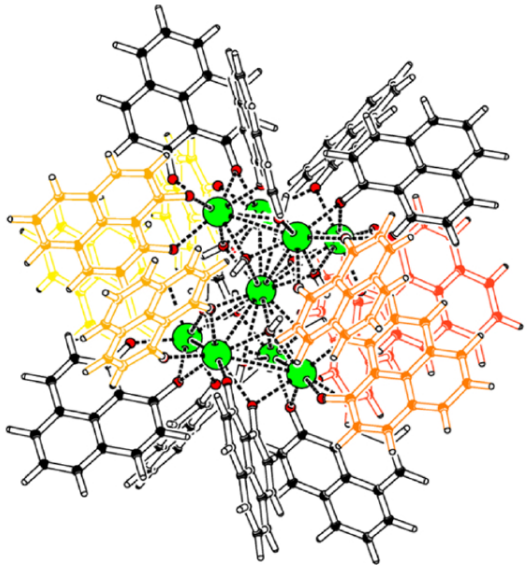

Figure 4.6: Structure of the nonanuclear europium complex at the BP/def2-TZVPP level of theory. Reprinted with permission from Ref. [115]. Copyright 2016 American Chemical Society.

With the geometry at hand one can calculate the charge distribution in the complex, which is needed for the ligand field part of the effective Hamiltonian and to calculate the ligand field splitting. The results of such a calculation are presented in comparison with the experiment in Figure 4.7 (note that the intensities are not calculated and are therefore assumed to be equal for all transitions). One can see that – especially in the low energy region – the agreement between experiment and calculation is quite good as the main features are reproduced. The whole calculated spectrum is however shifted by $\approx 500\,\mathrm{cm}^{-1}$

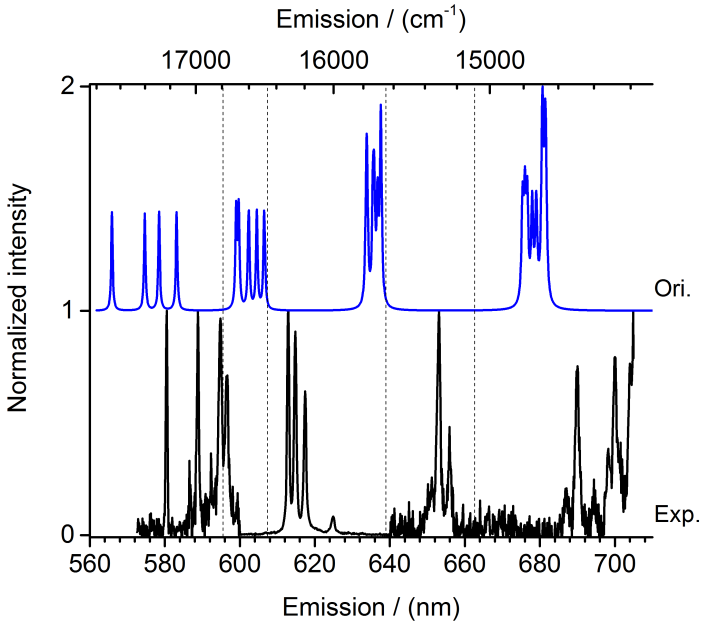

Figure 4.7: Comparison of the experimental (bottom) and calculated (with original parameters; top) luminescence spectrum of the nonanuclear europium complex. Reprinted with permission form Ref. [115]. Copyright 2016 American Chemical Society.

to higher energies. In order to understand and improve on this shift we need to look at the parameters in the effective Hamiltonian.

The Slater integrals and spin–orbit coupling constant used in the effective Hamiltonian are obtained by fitting to experimental results. Traditionally, this is done for lanthanides in crystals, i.e. in the solid state.[116] There is however no guarantee that such parameters are optimal for a gas-phase measurement that we have in our case since the situation in solids is much different to the situation in the gas-phase (e.g. periodicity, packing effects). We can now try to find a new set of parameters that would reproduce the gas-phase data better and would maybe eliminate the aforementioned shift. Since the experimental spectrum of the nonanuclear europium complex is well resolved it is a perfect candidate for an experimental reference.

I used the unambiguous seven lowest experimental transitions that I wanted to fit. The fit was done in a least squares way where I minimized the function R of the form:

$$R = R(F^2, F^4, F^6, \zeta) = \sqrt{\sum_{i=1}^{7} (E_{\mathrm{exp},i} - E_{\mathrm{cal},i})^2}, \tag{4.2}$$

where $E_{\mathrm{exp},i}$, and $E_{\mathrm{cal},i}$ stand for the experimental and calculated transition energies, respectively, and R is a function of Slater integrals F^k and the spin–orbit coupling constant ζ. The function R is nonlinear, very complicated and has many local minima. All of this made Newton–Rhapson or other standard optimization mechanisms inapplicable. Instead I made a scan of this function where I varied the parameters by different amounts and chose the combination that gave the lowest value of R as a starting point for the next step of optimization. In each step the parameters were either increased by a large amount, increased by a small amount, left unchanged, decreased by a small amount, or decreased by a large amount. For each parameter there were therefore five different possible values in each step of optimization. All different combinations of parameters were made which corresponds (for four parameters) to $5^4 = 625$ different sets of parameters in each optimization step. The combination that gave the lowest value of R was chosen as a starting point for the next step of optimizations where the amount of change for parameters was reduced. The total number of seven steps were used in the optimization as shown in Table 4.1.[115]

Table 4.1: The protocol used for optimization of parameters of H_{eff}. See text for further explanation.[115]

Optimization step	1	2	3	4	5	6	7
Change by larger/smaller amount in %	32/16	16/8	8/4	4/2	2/1	1/0.5	0.5/0.25

This was the so-called *unconstrained* optimization because all parameters were varied independently of each other. I also did a *constrained* optimization where I kept the ratios between the Slater integrals constant: $F^4/F^2 = 0.668$ and $F^6/F^2 = 0.495$ which are the recommended values that should be used when the number of experimental values is insufficient to do the unconstrained optimization.[117] The values of the original and optimized (both unconstrained and constrained) parameters for the BP/def2-SVP and BP/def2-TZVPP geometries can be found in Table 4.2. The comparison of the experimental and calculated transition energies is presented in Table 4.3.

From the values presented it is clear that the optimized parameters show a huge improvement over the original ones. The values of the fitting function for the optimized parameters are more than one order of magnitude smaller than those for the original parameters and

Table 4.2: The values of original and optimized parameters of H_{eff}. SVP and TZVPP denote the BP/def2-SVP and BP/def2-TZVPP structures, respectively. See text for further explanation. Data taken from Ref. [115].

		unconstrained		constrained	
values [cm^{-1}]	original parameters	SVP	TZVPP	SVP	TZVPP
F^2	83130	64260	61993	85985	85985
F^4	59271	74286	85903	57438	57438
F^6	42562	32042	27992	42562	42562
ζ	1338	1267	1264	1338	1338
$R = R(F^2, F^4, F^6, \zeta)$	1103[a]	53	68	81	91

[a]Computed for the BP/def2-TZVPP structure.

the absolute values of individual errors for each transition are in all cases (with the exception of $^5D_0 \rightarrow {}^7F_1$ ($m_J = 0$) transition with constrained optimization) lower than $50\,cm^{-1}$, which again is a huge improvement compared to the original parameters where the errors are $\approx 400\,cm^{-1}$. The unconstrained optimized parameters show slightly smaller errors with respect to the experimental values; the advantage of the constrained parameters is that they keep, unlike the unconstrained parameters, the correct labeling of the higher energy states in the calculation. Since, as already stated, already the constrained parameters produce results in much better agreement with the experiment than the original parameters I decided to work with them further.

The luminescence spectrum computed using the constrained optimized parameters is presented in Figure 4.8. It is apparent that the observed shift in the computed spectrum was eliminated and it is now in much better agreement with experiment. This of course is not surprising since the fit was done exactly in the way so that this experimental spectrum is reproduced. Now we have however a new set of parameters that can hopefully be used for gas-phase experiments on europium containing complexes. I will apply this set of parameters on a series of four ligand systems in the next section.

In this section we were concerned with the nonanuclear europium complex where the well resolved experimental spectrum was used to derive a new set of parameters for the effective Hamiltonian, which are more suited for computations on gas-phase complexes. The results so far seem promising.

Table 4.3: Comparison of experimental and calculated transition energies for the nonanuclear europium complex. The values of differences $\Delta_{\text{exp}} = E_{\text{exp}} - E_{\text{cal}}$ are presented for the original and optimized parameters of either unconstrained or constrained optimization. The values of optimization function R are presented as well. All values are given for the BP/def2-TZVPP structure in cm^{-1}. Data taken from Ref. [115].

Transition	Experiment	Δ_{exp} orig./unconst.	Δ_{exp} orig./const.
$^5\text{D}_0 \rightarrow ^7\text{F}_0$	17227	443/1	443/43
$^5\text{D}_0 \rightarrow ^7\text{F}_1 \quad (m_J = -1)$	16984	418/-8	418/12
$^5\text{D}_0 \rightarrow ^7\text{F}_1 \quad (m_J = 0)$	16813	474/47	474/68
$^5\text{D}_0 \rightarrow ^7\text{F}_1 \quad (m_J = 1)$	16763	385/-41	385/-20
$^5\text{D}_0 \rightarrow ^7\text{F}_2 \quad (m_J = -2)$	16316	377/-19	377/-35
$^5\text{D}_0 \rightarrow ^7\text{F}_2 \quad (m_J = -1)$	16266	408/12	408/-4
$^5\text{D}_0 \rightarrow ^7\text{F}_2 \quad (m_J = 0)$	16197	404/8	404/-8
$R = R(F^2, F^4, F^6, \zeta)$		1103/68	1103/91

4.4. Europium Luminescence as a Structural Probe

In this section I will describe the study of a series of four ligand systems of the form $[\text{Eu(PLN)}_4\text{AE}]^+$, where AE = Mg, Ca, or Sr. This was part of a series trying to describe in detail the sensitization process in europium containing complexes. It followed a similar study of the three ligand series $[\text{Eu(PLN)}_3\text{A}]^+$, where A = Li, Na, K, Rb, or Cs.[105] The questions that we wanted to investigate are two:

- Is it possible to transfer the optimized parameters derived for the nonanuclear europium complex (section 4.3) to other systems with different coordinations and still get improved results?

- Can the information about the luminescence of europium in the complex be used as information on the structure and local symmetry of the complex?

To answer these questions both the experimental and the theoretical methods need to be used to get a satisfying answer.

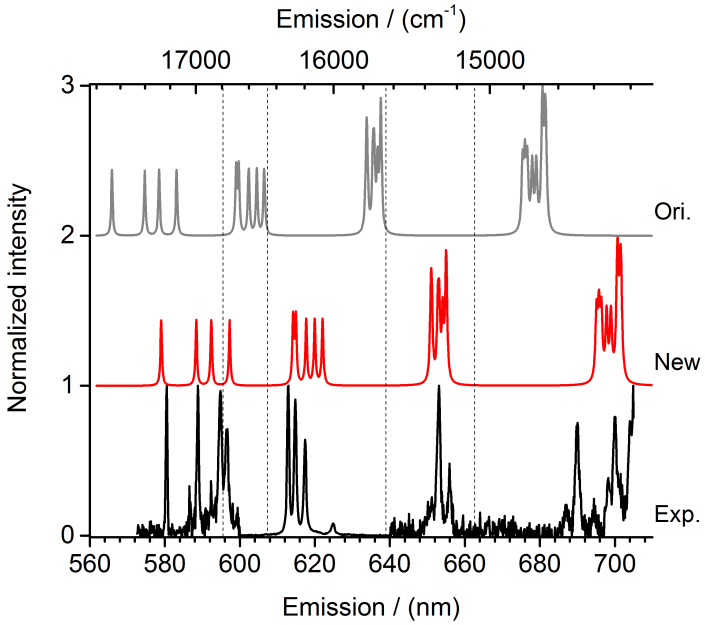

Figure 4.8: Luminescence of the nonanuclear europium complex – comparison of the experimental spectrum (bottom), spectrum calculated with constrained optimized parameters (middle), and spectrum calculated with original parameters (top). Adapted with permission from Ref. [115]. Copyright 2016 American Chemical Society.

4.4.1. Experimental Luminescence Spectra

The hypersensitive splitting of the Eu^{3+} $^5D_0 \rightarrow {}^7F_2$ transition is of interest in this study. This transition should in theory be split into five lines since the $^7F_2$ state splits into five $^7F_2(m_J)$ states with $m_J = -2 \ldots 2$. The experimental setup is well suited for measuring the cations in the gas-phase.[118] With the given resolution of the luminescence measurement the split of the emission spectrum to only two components (higher and lower) was observed; moreover the splitting and the positions of the peaks depend on the alkali earth metal used as documented in Figure 4.9.

The splittings between the high and low component in all different complexes amount to $\approx 130\,\mathrm{cm}^{-1}$. Both components grow in energy with the increasing size of the alkaline earth ion adduct (from Mg to Sr). This trend of splitting into two components and the behavior of the components depending on the alkaline earth atom present is what we want to investigate with the following computations. Since the experiment is done in the gas-phase there is no practical way to determine the structure (which in solid state could be done e.g. using

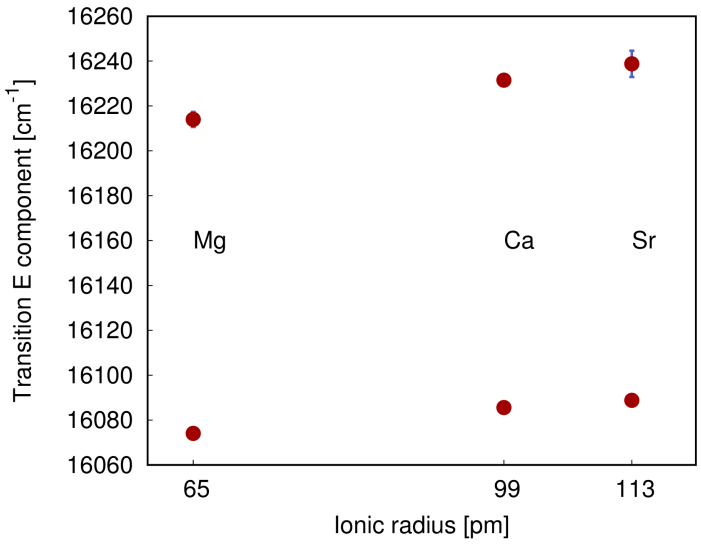

Figure 4.9: Energies of the upper an lower components of the $^5D_0 \rightarrow {}^7F_2$ emission band of the four ligand systems $[Eu(PLN)_4AE]^+$, AE = Mg, Ca, and Sr as a function of the ionic radius of the corresponding alkaline earth ion.[109]

X-ray spectroscopy) and the computation of a structure is the only way to suggest what the structure could look like.

4.4.2. Structural Motifs

I did a geometry optimization very much similar to the one described in section 4.3 that started from a guess given by a semi-empirical PM6-SPARKLE method. Again the optimization was done at the BP/def2-TZVPP level of theory. I found two different types of structures for each four ligand system via this optimization procedure which are depicted in Figure 4.10.

I will call the two binding motifs Set 1 and Set 2 (as already used in Figure 4.10) and even though the motifs might seem similar at first glance they are profoundly different. In Set 1 three PLN ligands act as bridging ligands between the europium and the alkaline earth ion while the last PLN ligand only coordinates the europium ion. In Set 2 however three ligands and the europium ion form a propeller like unit to which the alkaline earth ion is coordinated with the last PLN ligand coordinating only the alkaline earth ion. A similar propeller like unit was already found in the study of the three ligand system.[105] The propeller shows an almost perfect three-fold symmetry and the only major structural

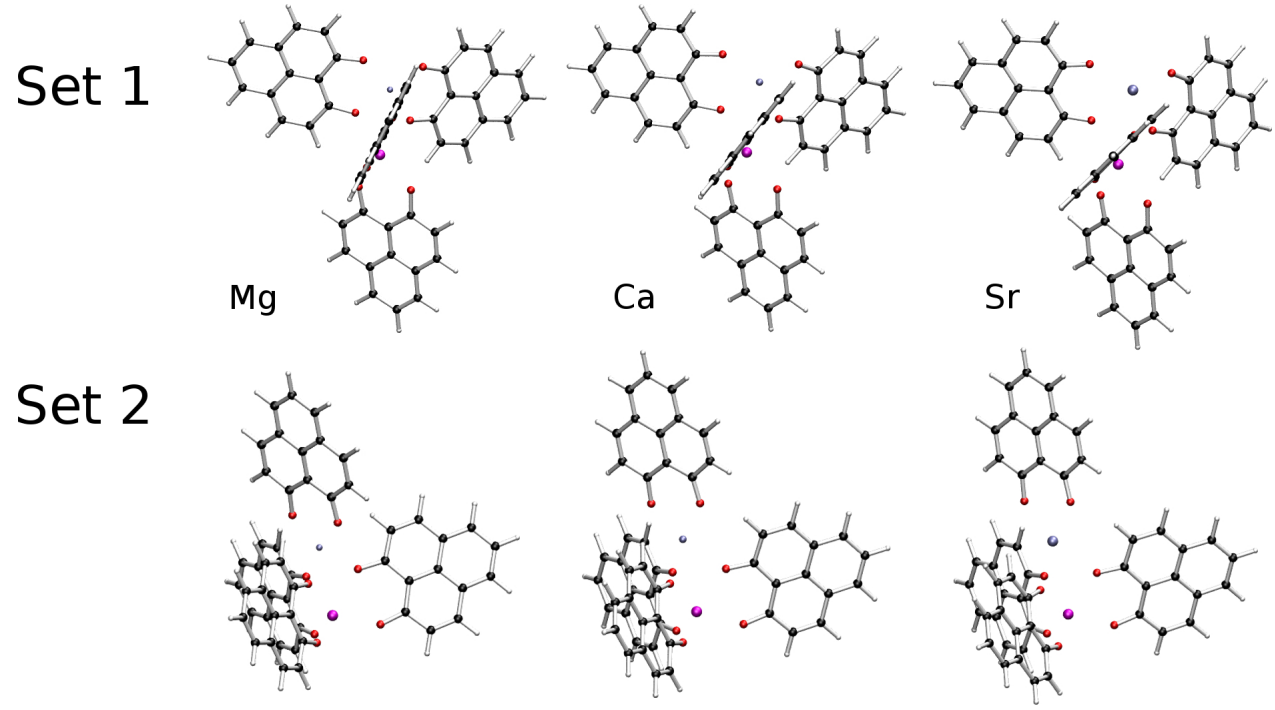

Figure 4.10: Structures computed at the BP/def2-TZVPP level of theory. Two sets with different binding motives were found. Eu in magenta, AE in blue, oxygen atoms in red.[109]

difference in the Set 2 structures is the tilt of the alkaline earth coordinating ligand with respect to the europium-alkaline earth line which is a bit larger in the Mg containing ligand than in the other two ($\approx 14°$ compared to $\approx$ 4–5°).

To further investigate the coordination sphere of the europium ion I again calculated the shape measures S for all presented structures. This time europium is in some sense unsaturated as it is only coordinated by six oxygen atoms. The relevant ideal polyhedra for this coordination are the octahedron (O_h) and the trigonal prism (D_{3h}) the exact geometries of which were taken from the literature.[91] Keeping in mind that lower values of shape measure S for a given geometry means that it is closer to the respective symmetry we may inspect the results summarized in Table 4.4.

We can rationalize the geometries and say that Set 1 geometries rather resemble an octahedron. Even though the difference between the two shape measures in the Mg containing complex is not large at least in the Ca and Sr containing complexes the coordination sphere of the europium ion can be described as a distorted octahedron. The situation is quite different in the Set 2 geometries which are all distorted trigonal prisms. Nevertheless it is

Table 4.4: Calculated shape measures for Set 1 and Set 2 structures of the four ligand systems.[109]

	Set 1		Set 2	
	$S(O_h)[^\circ]$	$S(D_{3h})[^\circ]$	$S(O_h)[^\circ]$	$S(D_{3h})[^\circ]$
Mg	21	27	44	5
Ca	15	34	38	8
Sr	12	37	33	12

interesting to note that even in the Set 2 structures the octahedron motif increases with increasing size of the alkaline earth ion (just like in the Set 1 case).

I also computed the harmonic frequencies to check if all structures are minima on the potential energy surface (which they are) and to get the zero-point energy (ZPE) correction to the electronic energies. Even after the ZPE correction the energies of the complexes do not differ much for different sets. As seen in Table 4.5 they never differ by more than about 10 kJ/mol which is well bellow the expected accuracy of the method used, so we cannot say for sure which one of the two sets should be energetically favorable if any.

Table 4.5: Energies of four ligand complexes at the BP/def2-TZVPP level of theory including the zero-point energy correction.[109] The Set 2 structures are lower in energy in case of Ca and Sr. See the text for further discussion.

Alkaline earth atom	$E_{\mathrm{Set}_2} - E_{\mathrm{Set}_1}$ [kJ/mol]
Mg	8
Ca	-7
Sr	-9

In this subsection I presented two possible geometrical motifs that can be present in the four ligand systems $[Eu(PLN)_4AE]^+$, AE = Mg, Ca, and Sr. Energetically they are equivalent so we need to have a look on how they can predict the (experimentally observed) trends in splitting of the hypersensitive transition in the europium ion.

4.4.3. Computations of Spectra Splitting

The splitting of the $^7F_2$ manifold was again computed using the effective Hamiltonian described in section 2.3.3. The calculated transition energies together with the experimental results are presented in Figure 4.11. Since the current version of the McPHASE program does not provide the calculation of the intensities, they are assumed to be equal for all transitions. The experimental broadening is mimicked using Gaussian functions with the width corresponding to the experimental resolution. The superposition of the Gaussians yields the maxima displayed in Figure 4.11 (b, c).[109]

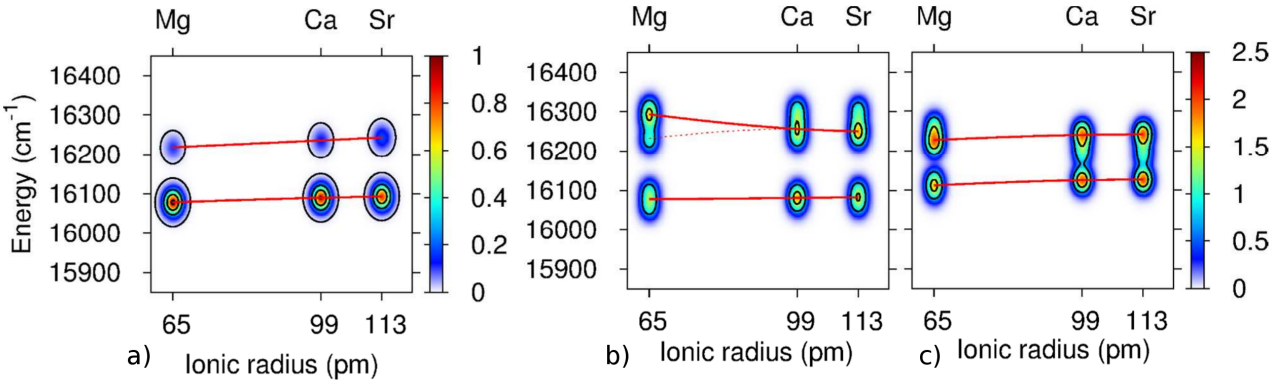

Figure 4.11: Experimental band positions and relative intensities of the $^5D_0 \rightarrow {}^7F_2$ transition in the four ligand systems as a function of ionic radius of the respective alkaline earth ion (a). The computed results for the Set 1 (b) and Set 2 (c) geometries are presented as well. Red lines are used to highlight trends. See text for further explanation.[109]

The first observation we make upon investigating the contour plots of Figure 4.11 is that indeed the optimized parameters of the effective Hamiltonian also work well for the four ligand system. When I used the original parameters the amount of splitting was still the same but shifted (similarly to the case of the computed spectrum of the nonanuclear europium complex in Figure 4.7) to higher energies as it can be seen in Figure 4.12. This is good news since it suggests that the parameters that I optimized for the nonanuclear europium complex can be used for other europium containing complexes in the gas-phase as well. Note that the optimized parameters also improved the ligand field splitting computations in the three ligand system.[105,115]

The second observation is about the two different types of structures. We can see that

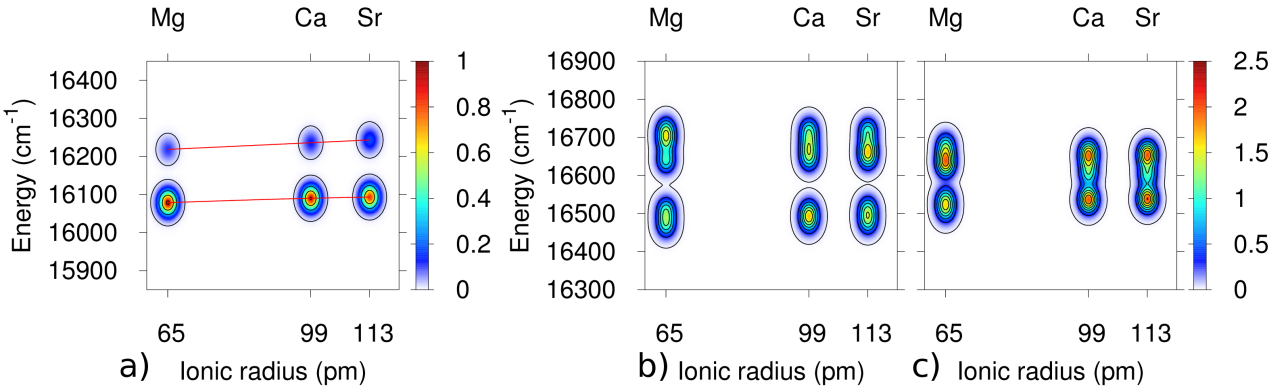

Figure 4.12: Experimental band positions and relative intensities of the $^5D_0 \rightarrow {}^7F_2$ transition in the four ligand systems as a function of ionic radius of the respective alkaline earth ion (a). The computed results for the Set 1 (b) and Set 2 (c) geometries *with the original parameters of* H_{eff} are presented as well. Note the difference in the energy scale compared to Figure 4.11.

they both reproduce the splitting quite well and that they split into two components (low energy and high energy). From the red lines that highlight the trends it is apparent that the structures of Set 2 resemble the experimental splitting more. This would suggest that the Set 2 structures are the ones observed experimentally. Another indirect support for this is the fact that the propeller like unit which is part of the Set 2 structure for all complexes is very similar to the structure computed for the three ligand system.[105] Since both types of complexes are present in the solution before electrospraying and mass selection it is easy to imagine that the Set 2 structure can be formed by direct addition of $AE(PLN)^+$ to the neutral $Eu(PLN)_3$ structure. The energies calculated do not allow to distinguish between the two sets and we cannot exclude the possibility of multiple luminescent conformers.[109] The assignment of the Set 2 structures to the experimental spectra would be supported by a number of indirect hints – the better agreement of the contour spectrum with the experimental one, the presence of the propeller unit found in the three ligand system, and the slightly lower energy in two cases (even though this should be taken with great caution). The only unambiguous way to check the structure would be to calculate also the intensities of the transitions, which is currently not possible. One can however try to improve the computed geometries. The deficiencies of DFT functionals for the calculation of dispersion interactions are well known[119] and it is therefore commonplace to apply corrections for

this that may change the computed structure. The application of such a correction on the four ligand system $[Eu(PLN)_4AE]^+$, AE = Mg, Ca, and Sr is described in the next section.

4.5. Dispersion Effects

Dispersion interactions play an important role in complex structures. Even though they are much weaker than ionic or covalent bonds they have a major influence on e.g. the spatial structure of proteins and other macromolecules. At least some part of dispersion should be therefore always included in calculations in large molecules where e.g. π–π stacking can take place. DFT is generally known to neglect most of the dispersion energy and it is a good idea to try to correct for it and see if the results change much. To do that I chose the very popular and simple D3 correction method[49,50] that was already described in section 2.2.2. Since the D3 correction is parameterized for each functional it is logical to test how much it would change the geometries of the four ligand systems (Set 1 and Set 2) if I add it to the BP functional used to obtained those geometries. The geometries re-optimized with the D3 correction are shown in Figure 4.13.

One immediately notices that while the structures did not change drastically for Set 2 there was an enormous change for Set 1 structures. The new structural motif observed in the Set 1-D3 structures is the π–π stacking of pairs of PLN ligands, which is due to the dispersion interaction. If we now look at the energy difference of these structures (Table 4.6) we can see a clear trend – the Set 1-D3 structures are always lower than Set 2-D3 structures by a considerable amount (at least 34 kJ/mol). This changes the picture completely and the Set 1-D3 structures seem now to be the favorite candidates.

Table 4.6: Energies of four ligand complexes at the BP-D3/def2-TZVPP level of theory including the zero-point energy correction.[120] The Set 1-D3 structures are lower in energy in all cases. See the text for further discussion.

Alkaline earth atom	$E_{\mathrm{Set_2\text{-}D3}} - E_{\mathrm{Set_1\text{-}D3}}$ [kJ/mol]
Mg	34
Ca	45
Sr	53

The structural change in the ligands was however not that pronounced in the oxygen co-

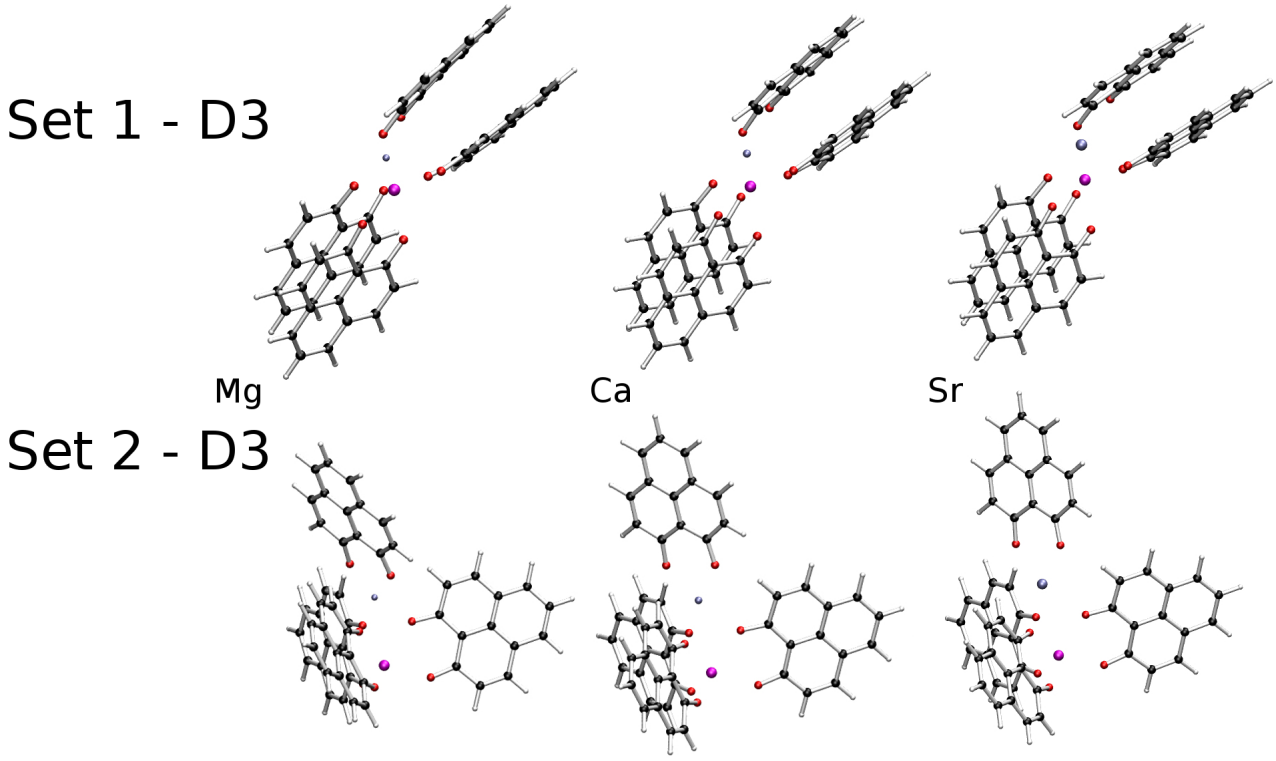

Figure 4.13: Structures computed at the BP-D3/def2-TZVPP level of theory. The structures for Set 1 differ significantly from those obtained from the computations without the D3 correction. Eu in magenta, AE in blue, oxygen atoms in red.[120]

ordination sphere of europium as it is documented by the calculated shape measures for the respective compounds (Table 4.7). They suggest a more uniform distribution in the Set 1-D3 structures as both shape measures, $S(O_h)$ and $S(D_{3h})$, are quite similar for all the structures. The D_{3h} character of the Set 2-D3 structures is less pronounced than in the Set 2 structures.

The results of the computation of the splitting of the hypersensitive transition (Figure 4.14) were surprising. While the splitting in the Set 2-D3 structures did not change significantly compared to the Set 2 structures (which is not surprising since the structures themselves did not change significantly) and still reproduces the experimental splitting fairly well, the splitting computed for the Set 1-D3 structures is in very poor agreement with the experiment. Not only are the energies quite shifted but also a splitting into three bands is predicted for the series of four ligand complexes, which does not agree with experiment.

To further investigate this geometrical effect a model system was constructed. In this model

Table 4.7: Calculated shape measures for Set 1-D3 and Set 2-D3 structures of the four ligand systems.

	Set 1-D3		Set 2-D3	
	$S(O_h)[°]$	$S(D_{3h})[°]$	$S(O_h)[°]$	$S(D_{3h})[°]$
Mg	17	33	37	11
Ca	16	33	36	10
Sr	14	34	31	15

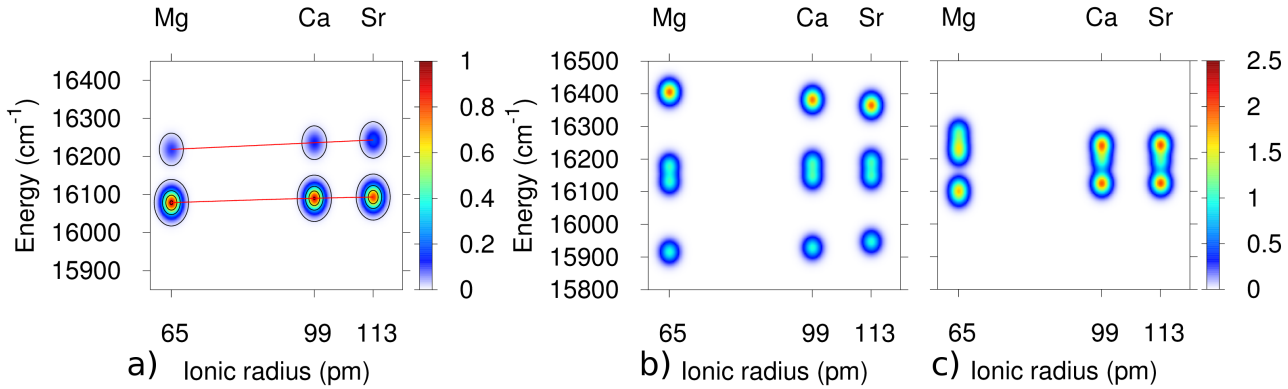

Figure 4.14: Experimental band positions and relative intensities of the $^5D_0 \rightarrow {}^7F_2$ transition in the four ligand systems as a function of ionic radius of the respective alkaline earth ion (a). Computed results for the Set 1-D3 (b) and Set 2-D3 (c) geometries are presented as well.[120]

system the Eu^{3+} ion was replaced with In^{3+}. In^{3+} has a size comparable to Eu^{3+} and its advantage is that it has no unpaired electrons in its shell (compared to Eu^{3+} that has six of them which makes it computationally much more demanding). In the model system BP, BP-D3, and MP2 geometry optimizations were performed with the def2-TZVPP basis set. The resulting geometries were very similar to the geometries of the original four ligand system $[Eu(PLN)_4AE]^+$, AE = Mg, Ca, and Sr in both BP and BP-D3 cases. Moreover the RIMP2 method also yielded a 'stacked' structure very similar to the BP-D3 geometry. This is another result supporting the Set 1-D3 geometries. Auxiliary basis sets for RIMP2 computations were not available for europium therefore the model system was needed. Preliminary results with a large core ECP and auxiliary basis set developed within this thesis (see chapter 6) support the conclusions drawn from the model system computations. While RIMP2 is one of the few feasible post-HF method for the geometry optimization of

the four ligand complexes it should be noted that it is by far not the most accurate method for lanthanide geometry optimizations.[121]

We are now facing two contradicting results. Energetically speaking the Set 1-D3 structures should be the most stable as their energy is the lowest by a significant amount (at least 34 kJ/mol lower than Set 2-D3 structures including the D3 correction). From the ligand field splitting, however, they are the worst when compared to the experiment. Both theoretical approaches – the computation of the electronic energy and the computation of the ligand field splitting – are of course approximative so it is hard to decide clearly on which should be of more value. It is now turn for another experimental approach to shed light on this problem.

4.5.1. Ion Mobility Measurements

In an ion-mobility spectrometry (IMS) experiment the velocity of transport of an ion of interest under the influence of an electric field in a buffer gas (typically helium) is measured. The velocity is proportional to the electric field and a structural parameter for the ion, called cross-section, can be extracted from this measurement. The cross-section depends on the geometry of the ion of interest. The cross-section can also be calculated for a given molecular geometry (obtained from e.g. a DFT geometry optimization) making IMS a very suitable technique to rule out geometries that are improbable.

The common assumption in deriving the expression for the cross-section Ω is that the molecular ion and helium atom are hard spheres resulting in:[122]

$$\Omega = \frac{1}{4\pi} \int_0^{\pi} \mathrm{d}\phi \, \sin(\phi) \int_0^{2\pi} \mathrm{d}\gamma \, \Omega_{\mathrm{dir}}(\phi, \gamma), \tag{4.3}$$

where $\Omega_{\mathrm{dir}}(\phi, \gamma)$ is a directional cross-section which needs to be further approximated. For example the exact hard-spheres scattering (EHSS) model (cf. blue squares in Figure 4.15) expresses the directional cross-section as:

$$\Omega_{\mathrm{dir}}(\phi, \gamma) = \int_{-\infty}^{\infty} \int_{-\infty}^{\infty} [1 - \cos(\chi(\phi, \gamma, y, z))] \mathrm{d}y \mathrm{d}z, \tag{4.4}$$

where $\chi(\phi, \gamma, y, z)$ is the scattering angle of the He atom. For EHSS and other approximative methods the collisional radius R(X–H), which is an empirical fitting parameter, needs to

be known in order to complete the calculation.[122]

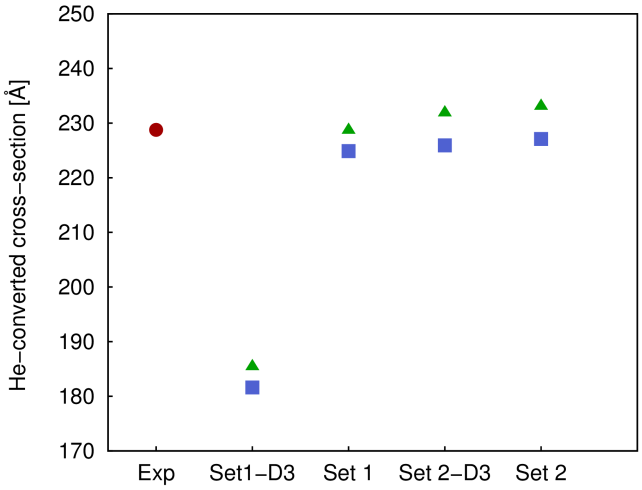

Figure 4.15: Comparison of the experimental cross-section and the cross-section calculated for the theoretically suggested structures of $[Eu(PLN)_4Ca]^+$. The blue squares[122] and the green triangles[123] represent two different methods of calculating the cross-section, the exact hard-spheres scattering (EHSS) model and the trajectory model, respectively. The Set 1-D3 structure can be clearly ruled out based on this measurement.[120]

The comparison of He-converted cross-sections of all up to now suggested geometries (i.e. Set 1, Set 1-D3, Set 2, and Set 2-D3) with the experimental cross-section for the $[Eu(PLN)_4Ca]^+$ complex is presented in Figure 4.15. Note that a very similar picture is obtained for all other alkali earth metal ions as well.

Inspecting the results of the ion mobility measurements we can see that the Set 1-D3 structures can be ruled out with high confidence as they differ from the experimental cross-sections significantly. The other structures however are indistinguishable with the current resolution of the experiment.

This is already a very valuable result. We saw that the Set 1-D3 structures were the lowest in energy (taking the D3 correction into account) but at the same time they had the poorest agreement with experiment in the ligand field splitting computations. Now we have *experimental evidence* that these structures do not occur in the gas-phase measurement itself. I will try to examine the D3 corrected structures in more detail in the next subsection.

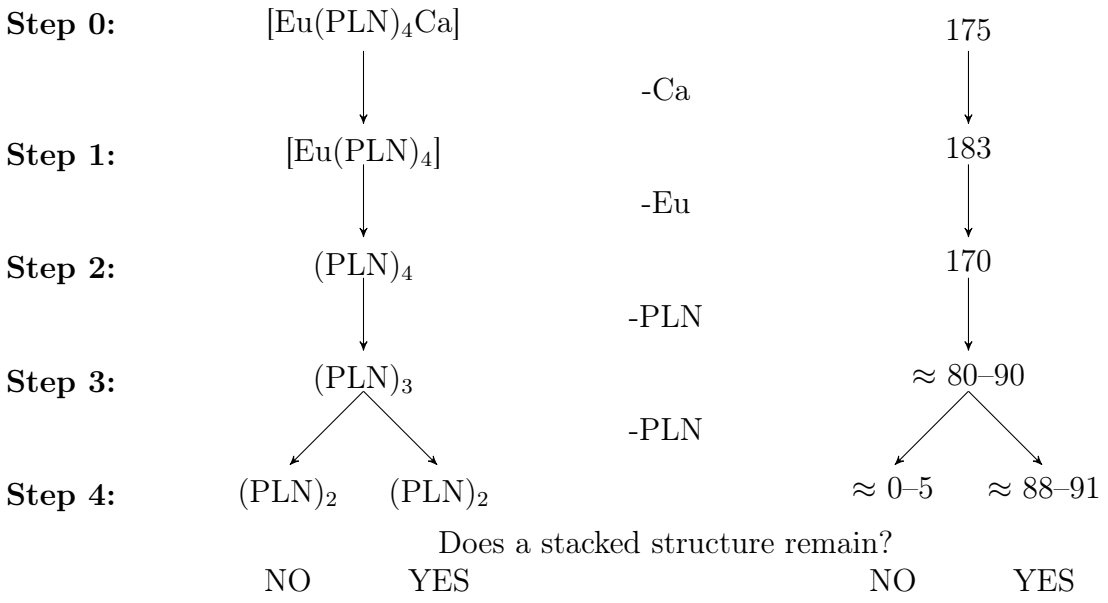

Figure 4.16: The decomposition of the $[Eu(PLN)_4Ca]^+$ complex. The difference D3 correction energies ΔE_{D3} is shown in kJ/mol for the Set 1-D3 and Set 2-D3 structures. The charge is left out in the description as it is not important since the D3 correction only takes into account positions of atoms. Further explanation in the text and graphically in Figure 4.17.

4.5.2. Decomposition of the D3 Energy Corrections

In the previous paragraph structures were presented that were computed at the BP-D3/def2-TZVPP level of theory. They showed some novel binding features compared to the structures computed at the BP/def2-TZVPP level of theory. The most prominent feature was the stacking of the two PLN ligands which was only observed when the D3 correction was employed and was further supported by the MP2 computations on the model system.
To see the importance of this stacking I will do a decomposition of the D3 energy (i.e. only the energy of the geometry dependent dispersion energy correction) in the given four ligand complex. The decomposition for the $[Eu(PLN)_4Ca]^+$ complex is sketched in Figure 4.16.
This figure needs a careful explanation. What we look at is the difference in dispersion corrections between the $[Eu(PLN)_4Ca]^+$ complexes in Set 1-D3 and Set 2-D3 structures, i.e. we look at the difference $\Delta E_{D3} = E_{D3,\text{ Set 1-D3}} - E_{D3,\text{ Set 2-D3}}$. The decomposition can be done in four steps. In the left part of Figure 4.16 the formulas of fragments are presented and in the right part there are the corresponding values of ΔE_{D3} in kJ/mol. In the zeroth step we

only get the D3 energy difference for the full complexes which is 175 kJ/mol. In the first step we remove the AE (in this case Ca) ion and the D3 energy difference changes only a little (to 183 kJ/mol). In the second step the Eu ion is removed and again the D3 energy difference does not change much (to 170 kJ/mol). In the third step however one of the PLN ligands is removed which destroys one of the stacked pairs in the Set 1-D3 structure but has a much smaller effect on the Set 2-D3 structure. The D3 energy difference gets therefore approximately halved to ≈ 80–90 kJ/mol; this range here is due to the fact that the energy depends on the combination of PLN ligands that are removed from the two structures. In the fourth step another PLN ligand is removed and there are two options – either we remove a PLN ligand so that another stacked pair is destroyed in the Set 1-D3 structure in which case there is practically no D3 energy difference (≈ 0–5 kJ/mol) or we remove a different PLN ligand and one stacked pair of ligands still remains in the Set 1-D3 structure in which case the D3 energy difference stays quite high at ≈ 88–91 kJ/mol. To illustrate the decomposition even more clearly it is shown also by means of structures in Figure 4.17. The D3 decomposition shows what we already expected, i.e. the largest portion of the difference in dispersion stems from the stacked pairs of the PLN ligands present in the Set 1-D3 structures. It is therefore crucial to describe the interaction between the two PLN ligands correctly and we can use such a system as a model to test different computational methods.

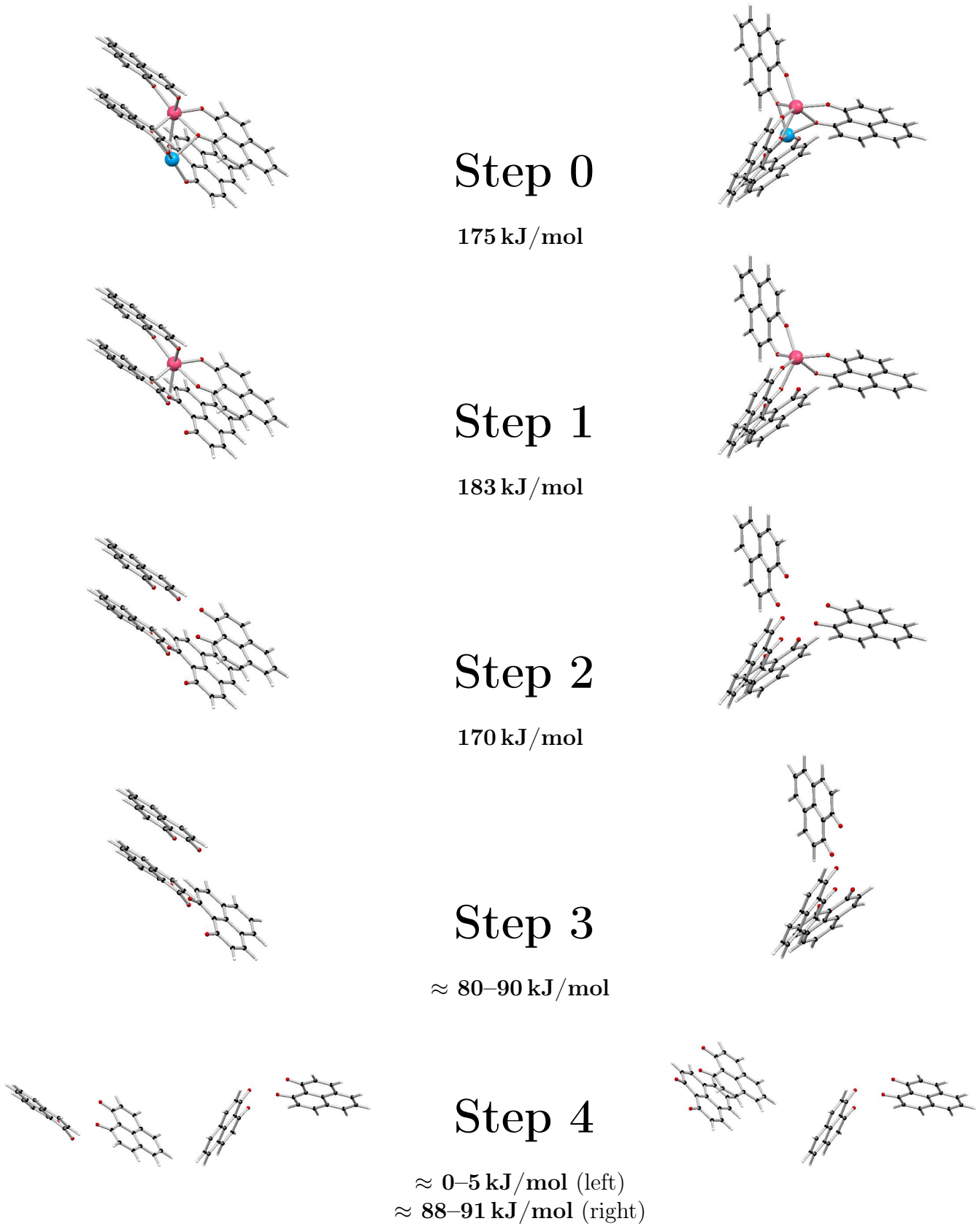

Figure 4.17: Graphical representation of the decomposition of D3 energy contributions. The ΔE_{D_3} difference is computed and shown in each step between the Set 1-D3 (left) and the Set 2-D3 (right) structures. In Step 4 there are two options. Ca in blue, Eu in magenta, oxygen in red. See also text and Figure 4.16.

4.5.3. Benchmark on the Stacked PLN Ligands

In the previous text a decomposition of D3 energy contributions of the proposed structures was done. The conclusion was that the most important interaction to describe the dispersion in the four ligand systems correctly is the interaction between the two stacked PLN ligands. A model structure was therefore proposed, which is depicted in Figure 4.18 that is reasonably small so that more advanced theoretical methods could be tested.

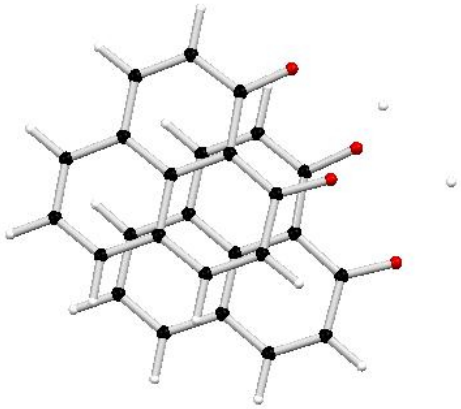

Figure 4.18: Model structure of two PLN ligands to calibrate the amount of dispersion needed to correctly describe the binding in the four ligand complexes. The two protons outside the PLN conjugated systems were added at the positions of Eu^{3+} and Ca^{2+} to make the molecule neutral and compensate for the cations present in the full complex.[120]

The interaction energy of this model structure was computed, i.e. the reaction energy of:

$$(\mathrm{HPLN})_2 \rightleftharpoons 2\,\mathrm{HPLN}, \tag{4.5}$$

which is $\Delta E_{\mathrm{int}} = 2E_{\mathrm{HPLN}} - E_{(\mathrm{HPLN})_2}$. Various DFT functionals with and without the D3 correction, the HF method and some more involved correlated methods were tested and a selection of interesting results is given in Table 4.8 and Figure 4.19.

From the results presented it is clear that the BP functional predicts the stacked structure to be unstable (since $\Delta E_{\mathrm{int}} = 17\,\mathrm{kJ/mol} > 0$) whereas the dispersion corrected BP-D3 approach predicts the same structure to be quite stable (with $\Delta E_{\mathrm{int}} = -81\,\mathrm{kJ/mol} < 0$). This is in line with our previous findings since the Set 1 and Set 1-D3 geometries differ exactly in this ligand stacking. Various functionals give very different interaction energies;

Table 4.8: Interaction energies of the model system of two stacked PLN ligands computed at various levels of theory; values in kJ/mol.[120]

Method	ΔE_{int}	Method	ΔE_{int}
HF	38	M06	-49
BLYP	33	BHLYP-D3	-55
B3LYP	24	HF-D3	-57
BP	17	PBE0-D3	-57
TPSS	14	B3LYP-D3	-63
BHLYP	13	TPSS-D3	-62
PBE0	1	BLYP-D3	-71
PBE	-6	PBE-D3	-74
CCSD-F12	-25	BP-D3	-81
B2PLYP	-26	MP2	-110
best[a]	-27	M06-D3	-111
CCSD(T)	-31		

[a]CCSD(T) + F12 part of CCSD-F12

the D3 correction predicts in all cases the stacking to be much stronger than the respective non D3 counterpart. With the information obtained before in this chapter (especially the ion mobility measurement results) it is to be assumed that the right interaction energy lies somewhere between the values for BP and BP-D3. The MP2 method, the simplest of the correlated post-HF methods, fails spectacularly in this case. The most demanding and accurate calculation we could afford for this model system was a calculation at the CCSD(T)/def2-TZVPP level of theory corrected with the F12 correction for explicit correlation taken from CCSD-F12/def2-TZVPP computations. The interaction energy at this 'best' level of theory was -27 kJ/mol. A cheaper method (preferably a DFT functional) that could reproduce this number for the model system would probably be a good candidate for re-optimization of the geometries of the four ligand systems $[Eu(PLN)_4AE]^+$, AE = Mg, Ca, and Sr. However, most of the methods are inappropriate in this sense and the functional with the closest binding value to the reference, the B2PLYP functional, is currently not implemented for geometry optimizations in TURBOMOLE. We can however compute single point energies at the B2PLYP/def2-TZVPP level of theory for the original structures (Set 1 and Set 2) as it is presented in Table 4.9. The two sets of structures are still very close to each other and no additional conclusions for our structures can be drawn (cf. Table 4.5). Another option would be to scale a given DFT method accordingly, e.g. the

PBE-D3 method with its D3 correction scaled to ≈ 0.5 should also provide results close to our best estimate.

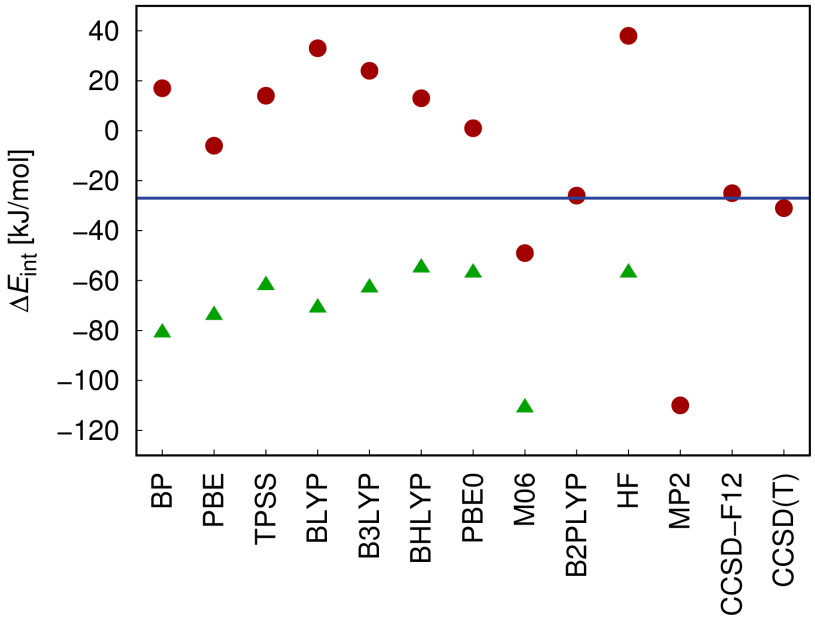

Figure 4.19: Interaction energies of the model system of two stacked PLN ligands computed at various levels of theory.[120] Computations without (red circles) and with the D3 corrections (green triangles) are presented together with the 'best estimate' (blue line) that corresponds to the CCSD(T) computation corrected with the F12 correction for explicit correlation taken from CCSD-F12 computations. All computations were performed with the def2-TZVPP basis set.

The summary of this section is therefore both very complicated in practice and trivial in its essence. One needs to calculate the *correct* amount of dispersion. Neglecting it can result in not finding the right minima on the potential energy surface but overestimating dispersion can have an equally unwanted feature of finding too many artificial *stacked* structures which is arguably even worse. The just presented problem should serve as a memento that generalized recommendations such as "always use a D3 correction with DFT" should be approached with caution if not abandoned altogether.

Table 4.9: Differences of energies $\Delta E = E_{\mathrm{Set}_2} - E_{\mathrm{Set}_1}$ of four ligand complexes including the zero-point energy correction at the BP/def2-TZVPP level of theory. The Set 2 structures are lower in energy in case of Ca and Sr. See the text for further discussion.

Alkaline earth atom	$\Delta E\,[\mathrm{kJ/mol}]^a$	$\Delta E\,[\mathrm{kJ/mol}]^b$
Mg	8	1
Ca	-7	-13
Sr	-9	-11

[a]BP/def2-TZVPP
[a]B2PLYP/def2-TZVPP

4.6. Conclusions

In this chapter I studied complexes that contain (one or more) europium ions. We saw that the methods of computational chemistry can be used to predict geometries and luminescence properties of such complexes. For the nonanuclear europium complex I found a set of gas-phase parameters that can be used in the effective Hamiltonian to predict the energy levels in europium and the transitions and therefore luminescence between them. I showed later that these parameters are transferable to other systems with different coordination as in the four ligand systems. We also witnessed how some information about the local coordination of the europium ion can be extracted from the calculation and how this can be further refined using suitable experimental techniques. In the last part of the chapter I analyzed in detail what is the influence of dispersion on these kind of complexes, why is it important, but also why it should not be overestimated.

The process that I tried to describe primarily in this chapter was the luminescence *of the lanthanide ion*. In the next chapter I will show what happens if the energy transition from the ligand to the metal cannot take place and a phosphorescence of the ligand is observed instead.

5. Phosphorescence in Complexes Containing Lanthanides

In the last chapter I was describing in detail the process of lanthanide (europium) sensitization in a complex with several suitable PLN ligand molecules. What would happen however if the sensitization and therefore the luminescence could not take place for some reason? This is going to be the main topic of this chapter. The reasons for studying these processes are twofold – the first is the general interest in all processes in lanthanide complexes, the second is that the phosphorescence that can take place is a competing process to the lanthanide luminescence described in the previous chapter. Similarly to the last chapter I will start with presenting the compounds and processes that we study and then I will present the results of my computations and compare them to the results of available experiments. But before that I will illustrate the methodology used in this chapter to compute the luminescence spectra of organic molecules. As described in section 2.5 the Franck-Condon factors can be computed that describe the overlap between vibrational wave functions of two states involved in the luminescence. We did some test computations on the TOTA molecule, which is a rigid planar conjugated organic molecule. In Figure 5.1 the experimental luminescence spectrum together with the computed spectrum are presented. Note that the computed spectrum was shifted to match the 0–0 transition of the experimental spectrum. The position of the 0–0 transition depends on the energy separation of the two states involved (S_0 and S_1 in case of TOTA) and will be discussed for the lanthanide containing complexes later in this chapter. Inspecting Figure 5.1 we can see that the main features are reproduced by the computations and the method of computing vibrationally resolved spectra using the Franck-Condon factors seems promising.

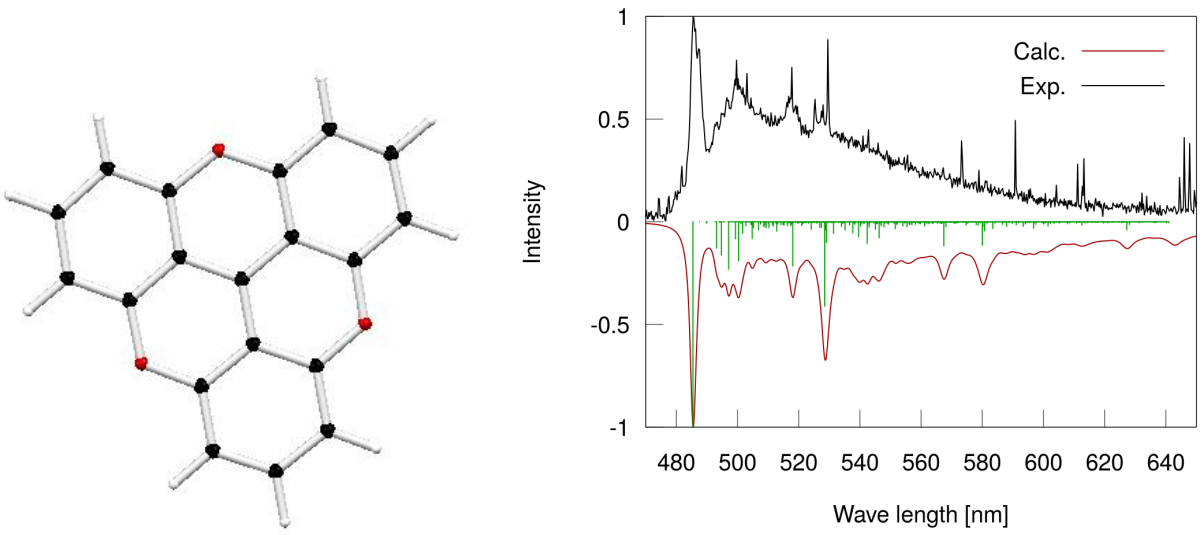

Figure 5.1: TOTA molecule: its structure (left) and experimental and computed fluorescence spectrum (right). Spectra are scaled and shifted. Computations were performed at the B3LYP/def2-SVP level of theory. See text for further explanation.

5.1. Sensitization of Lanthanides

If we want to prevent the sensitization of the lanthanide ion in a complex in principle we want to disable the energy transfer to the metal ion (i.e. process (3) in Figure 4.2). This can be realized in two ways: either by taking a different ligand than PLN (a 'not suitable' ligand, cf. section 4.1.1) or by taking a metal center other than europium. Both of these options will hinder the energy transfer. Since one of the motivations is also to try better understand the processes taking place in the PLN ligand the second option with a different lanthanide ion is of interest. Looking at the Dieke-type diagram that summarizes the experimental results about energy levels in lanthanide Ln^{3+} ions[124,125] one can assume that the gadolinium ion should be a suitable candidate since its first excited state lies at around $32000\,cm^{-1}$ above the T_1 state of PLN. If the sensitization is disabled the complex stays in the T_1 state of PLN and phosphorescence takes place instead. This phosphorescence and the way it depends on the lanthanide atom in the complex will be of interest here.

In this chapter we will study complexes of type $[X(PLN)_2]^+$, where X stands for a lanthanide atom. These represent molecules approximately half the size of the four ligand system. Many of them were studied experimentally[126,127] but here I choose to discuss the two that

have been described the most; namely $[Gd(PLN)_2]^+$ and $[Lu(PLN)_2]^+$.
Experimentally the phosphorescence spectrum in the gas-phase was measured for both of these complexes. The spectra are depicted in Figure 5.2 and one can see that overall they look very similar and the largest difference is in the position of the most intense peak (the 0–0 transition) – the spectrum of $[Lu(PLN)_2]^+$ is shifted by $\approx 135\,cm^{-1}$ to higher energies with respect to the spectrum of $[Gd(PLN)_2]^+$.

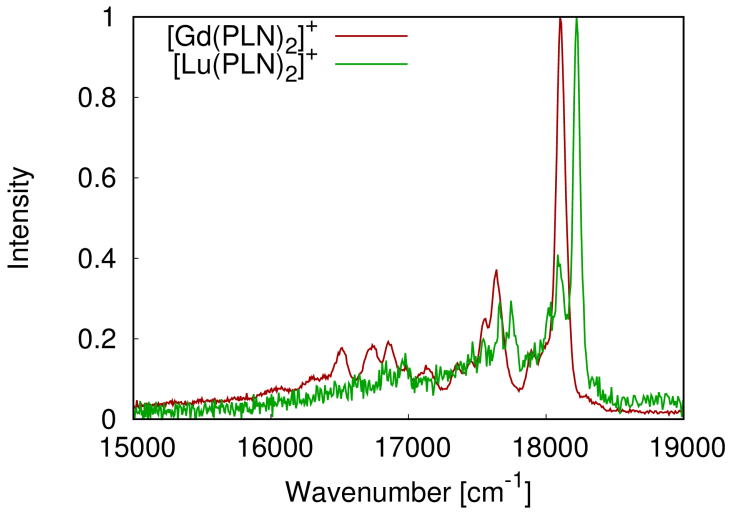

Figure 5.2: Experimental phosphorescence spectra of $[Gd(PLN)_2]^+$ and $[Lu(PLN)_2]^+$.[127] Note that the shape of the two spectra is very similar. They are shifted with respect to each other by $\approx 135\,cm^{-1}$.

5.2. Computed Structures and Symmetry

Since phosphorescence of the PLN ligand is of interest here one needs to calculate the geometry of the complex in two states important for the phosphorescence – the initial T_1 state and the final S_0 ground state. I used again the DFT method with the BP functional and the def2-SVP basis set to optimize the geometry of the complexes. To check the results I also tried the very popular B3LYP functional with the def2-TZVPP basis set. The technical problem I was facing was to obtain the correct state for the complex. The ground state of $[Gd(PLN)_2]^+$ should be an octet since the f-shell of Gd^{III} is exactly half filled. Even though the lowest lying excited state should be mainly localized on the ligands (which is what we

want) it is not clear what the total multiplicity of such a state should be. The situation is less complicated for the $[Lu(PLN)_2]^+$ complex as the f-shell of Lu^{III} is filled completely.
A convenient way to overcome these problems is to make use of the 'large core' effective core potentials (ECPs)[128,129] that are suited specially to represent the X^{3+} ions where X is a lanthanide. Their advantage is that they take all the f-electrons into the effective core potential and make the metal ion effectively closed shell and (as a byproduct) they make sure that the excitation will take place on the ligand. For comparison I also used the 'standard' ECPs with 28 electrons for optimization of the ground state structure. The general ideas of ECPs were described in section 2.3.1 and the peculiarities of different ECPs for lanthanides is described in detail in chapter 6 so I will not discuss them at this point any further.

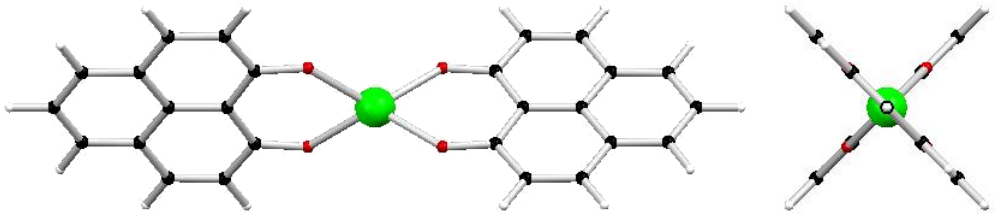

Figure 5.3: Structure of $[Gd(PLN)_2]^+$ computed at the B3LYP/def2-TZVPP level of theory illustrating the D_{2d} symmetry of the complex.

Regardless of the functional (or ECP) used both the ground state S_0 and the T_1 state were found to be of D_{2d} symmetry. This applies for both molecules – $[Gd(PLN)_2]^+$ and $[Lu(PLN)_2]^+$. They only differ in the metal-oxygen distance which is to be expected for different central metals. The illustrative structure of one of the complexes is given in Figure 5.3. After the geometry optimization the computation of harmonic vibrational frequencies was carried out for the S_0 and T_1 structures to check whether they are minima on the potential energy surface and also because the information on vibrations was needed as input for the calculation of the Franck-Condon factors and therefore the phosphorescence spectra as we will see in the next section.

5.3. Phosphorescence Spectra

The phosphorescence of the PLN ligand was modeled by calculating the overlap of the initial and final vibrational wave functions. As already described in section 2.5 the HOTFCHT program package[88] was used to perform these calculations. The computation can be done in two ways using this program. First is the time-independent approach where the Franck-Condon integrals are evaluated and transitions are computed that can be directly connected to respective vibrations of the molecule. This computation however can be very time consuming for large or even medium sized molecules. The time requirement grows even more if we want to calculate the spectrum at some temperature higher than 0 K. The second approach is called time-dependent; it takes into account the dynamics in the final state (S_0 in this case) and makes use of the Fourier transform of the overlap integrals (from energy to time domain hence the name). It is much faster to perform but the assignment of contributions is lost in the process. For our systems $[Gd(PLN)_2]^+$ and $[Lu(PLN)_2]^+$ the time-dependent method can also be used to calculate spectra at higher temperatures.

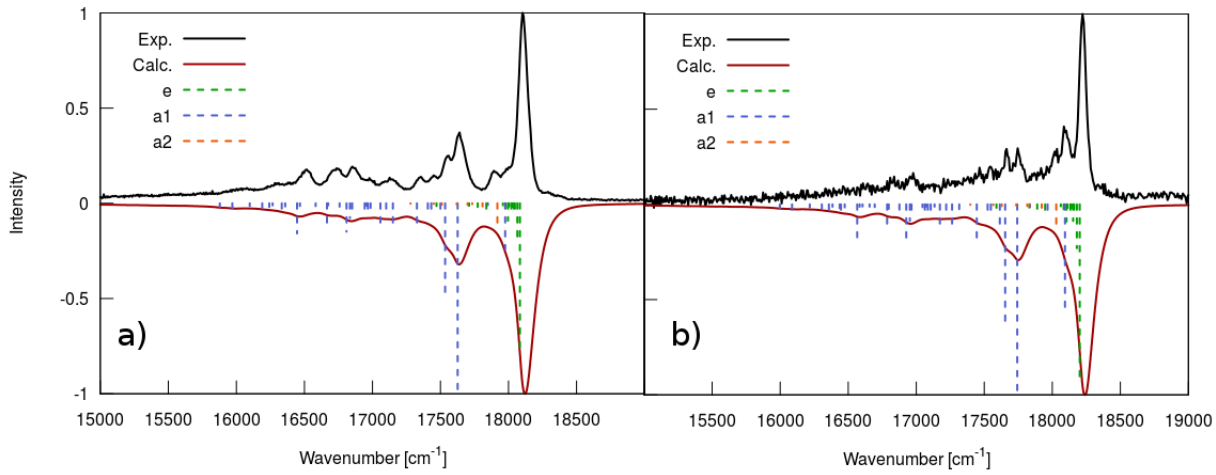

Figure 5.4: The phosphorescence of the PLN ligand in the $[Gd(PLN)_2]^+$ (a) and $[Lu(PLN)_2]^+$ (b) complexes. Experimental data together with the time-dependent and time-independent computations are presented. Computation of geometry and harmonic vibrational frequencies was done at the B3LYP/def2-TZVPP level of theory with the large core ECP. The three most contributing irreducible representations (e, a_1, and a_2) are shown. The computed spectra are shifted to match the 0–0 transition of the experiment (see text for further discussion).

I performed both types of computations, the time-dependent and the time-independent, and their results are presented in Figure 5.4. From the time-dependent computation one can see that the overall shape of the spectrum was reproduced for both complexes. The dominant peak corresponds to the 0–0 transition between the lowest lying vibrational states of the two respective electronic surfaces (T_1 and S_0) and the major contribution comes from the vibration belonging to the e irreducible representation as is provided by the time-independent computation. It seems now that the proposed D_{2d} structures provide a reasonable phosphorescence spectrum and are therefore plausible. The only remaining problem is to determine the position of the most dominant 0–0 transition. The position corresponds to the energy difference between the two electronic states involved in the phosphorescence process (i.e. T_1 and S_0) and its calculation will be discussed in the next section.
Some temperature dependence of the phosphorescence spectrum of $[Gd(PLN)_2]^+$ was investigated as well since the spectrum was recorded at 83 K and also at 293 K. The effect can be simulated in the computation where higher energy vibrational states will be populated for the room temperature spectrum. The results of these calculations are presented in Figure 5.5 but are not satisfactory. While the low temperature spectrum (which was also already presented in Figure 5.4) is reproduced nicely the computed room temperature spectrum does not look like the experimental spectrum at all, featuring an artificial peak at very high energies (the artificial peak is probably an artifact of the Fourier transform). One of the possible explanations is that the assumptions used to justify the calculation (mainly the assumption of harmonicity of the vibrations) are not fulfilled for high temperatures and the calculation using Franck-Condon factors is therefore inadequate.

5.4. Position of the 0–0 Transition

As already mentioned earlier the position of the phosphorescence spectrum on the energy axis depends on the energy difference between the T_1 and S_0 states. It is rather challenging to get the position right and before that I will try to tackle another problem. I will try to compute the difference between the 0–0 transitions in the two different complexes. If we call the corresponding electronic energies of the $[Gd(PLN)_2]^+$ and $[Lu(PLN)_2]^+$ as E_{Gd,T_1}, E_{Gd,S_0}, E_{Lu,T_1}, and E_{Lu,S_0} we can calculate the difference between the 0–0 transitions

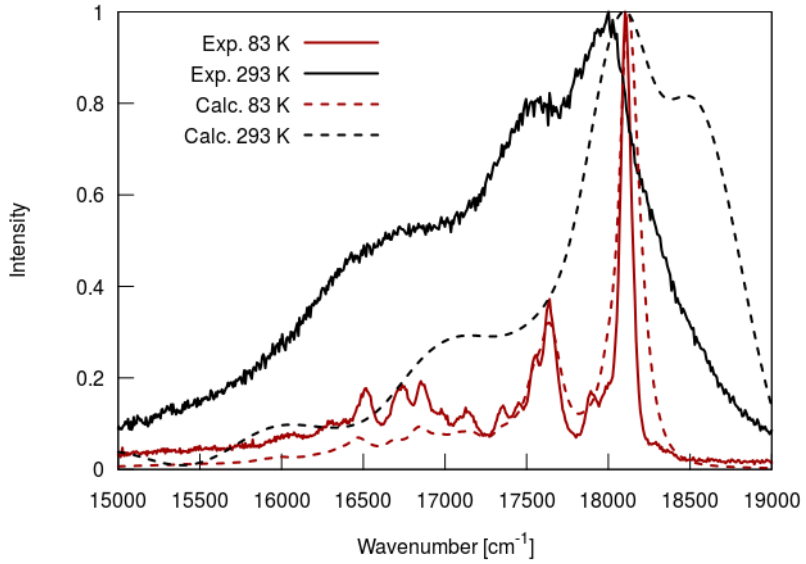

Figure 5.5: Temperature dependence of the phosphorescence spectrum of $[Gd(PLN)_2]^+$. Experimental results are compared to the calculation done at the B3LYP/def2-TZVPP level of theory with the large core ECP.

$\Delta E_{\text{Lu-Gd}}$ and therefore the shift between the spectra in Figure 5.2 as:

$$\Delta E_{\text{Lu-Gd}} = (E_{\text{Lu,T}_1} - E_{\text{Lu,S}_0}) - (E_{\text{Gd,T}_1} - E_{\text{Gd,S}_0}). \tag{5.1}$$

Experimentally this difference is found to be $\approx 135\,\text{cm}^{-1}$. Since the complexes studied here are of the moderate size of 45 atoms I can use many methods to calculate the energy of the S_0 and T_1 states including the more expensive coupled-cluster methods. To be able to use these correlated methods (MP2 and CC with the RI approximation) I had to derive a special set of auxiliary basis sets for the lanthanide atoms (Gd or Lu). The derivation of such a basis set is described in detail in chapter 6. The results of my computations of $\Delta E_{\text{Lu-Gd}}$ are summarized in Table 5.1.

The first thing to note is the fact that all methods with the exception of the HF method predict the right trend, i.e. the transition in $[Lu(PLN)_2]^+$ to be higher in energy than the transition in $[Gd(PLN)_2]^+$. Another interesting observation is that the MP2 method overestimates the difference drastically. The best agreement with the experiment is obtained with the expensive CCSD and CCSD(T) methods even though one could argue that already the values for the BP functional are quite good since they only differ from the experiment

Table 5.1: The difference between the 0–0 transitions of $[Lu(PLN)_2]^+$ and $[Gd(PLN)_2]^+$ denoted as $\Delta E_{\text{Lu-Gd}}$. Computations were done with the def2-TZVPP basis set and the large ECP. The zero-point vibrational energy at the B3LYP/def2-TZVPP level of theory is included (about $-12\,\text{cm}^{-1}$). The RI approximation was used in all computations.

Method	$\Delta E_{\text{Lu-Gd}}\,[\text{cm}^{-1}]$	Method	$\Delta E_{\text{Lu-Gd}}\,[\text{cm}^{-1}]$
Experiment	135	BP[a]	236
B3LYP[a]	304	B3LYP[b]	167
HF[a]	−62	MP2[a]	1200
CCSD[a]	105	CCSD(T)[a]	138

[a] at B3LYP/def2-TZVPP geometry
[b] at BP/def2-SVP geometry

by $\approx 100\,\text{cm}^{-1}$. It is interesting to note the difference between the two geometries at which the B3LYP functional was tested. The agreement with experiment is better for the BP/def2-SVP geometry than for the B3LYP/def2-TZVPP geometry. The difference comes from the $[Gd(PLN)_2]^+$ structure where the 0–0 transitions (without the zero point energy correction) are $20899\,\text{cm}^{-1}$ and $20792\,\text{cm}^{-1}$ for the BP/def2-SVP geometry and B3LYP/def2-TZVPP geometry, respectively. The corresponding energy differences in the $[Lu(PLN)_2]^+$ complex are closer with $21078\,\text{cm}^{-1}$ and $21108\,\text{cm}^{-1}$ for the BP/def2-SVP geometry and B3LYP/def2-TZVPP geometry, respectively.

Now I come back to the original problem of computing the positions of the transitions themselves. The discussion of the results is very similar for the molecules $[Gd(PLN)_2]^+$ and $[Lu(PLN)_2]^+$. The positions of the 0–0 transitions ΔE_{Gd} and ΔE_{Lu} are given by:

$$\Delta E_{\text{Gd}} = E_{\text{Gd,T}_1} - E_{\text{Gd,S}_0}, \tag{5.2}$$

$$\Delta E_{\text{Lu}} = E_{\text{Lu,T}_1} - E_{\text{Lu,S}_0}. \tag{5.3}$$

The experimental values are $18083\,\text{cm}^{-1}$ for $[Gd(PLN)_2]^+$ and $18218\,\text{cm}^{-1}$ for $[Lu(PLN)_2]^+$ (cf. Figure 5.2) which is shown together with the computed values in Table 5.2 and in Table 5.3. It can be seen that none of the methods is in particularly good agreement with the experiment since they are either $\approx 2000\,\text{cm}^{-1}$ too low or $\approx 2000\,\text{cm}^{-1}$ too high in energy. The MP2 method once again shows a particularly bad agreement with the experiment. The

Table 5.2: The position of the 0–0 transition of $[Gd(PLN)_2]^+$ denoted as ΔE_{Gd}. Computations were performed with the def2-TZVPP basis set with the large core ECP. The zero-point vibrational energy at the B3LYP/def2-TZVPP level of theory is included (about $-135\,cm^{-1}$). The RI approximation was used in all computations.

Method	$\Delta E_{Gd}\,[cm^{-1}]$	Method	$\Delta E_{Gd}\,[cm^{-1}]$
Experiment	18083	BP[a]	15880
B3LYP[a]	20657	B3LYP[b]	20765
HF[a]	16053	MP2[a]	36343
CCSD[a]	20532	CCSD(T)[a]	20712

[a] at B3LYP/def2-TZVPP geometry
[b] at BP/def2-SVP geometry

diagnostic parameters in the CCSD and CCSD(T) computations together with the fact that the result does not change much for CCSD and CCSD(T) suggest that the effect of higher excitations should not be of great importance. A possible improvement of such a systematic error we observe could be the inclusion of spin–orbit coupling.

Table 5.3: The position of the 0–0 transition of $[Lu(PLN)_2]^+$ denoted as ΔE_{Lu}. Computations were performed with the def2-TZVPP basis set with the large core ECP. The zero-point vibrational energy at the B3LYP/def2-TZVPP level of theory is included (about $-147\,cm^{-1}$). The RI approximation was used in all computations.

Method	$\Delta E_{Lu}\,[cm^{-1}]$	Method	$\Delta E_{Lu}\,[cm^{-1}]$
Experiment	18218	BP[a]	16116
B3LYP[a]	20961	B3LYP[b]	20931
HF[a]	15991	MP2[a]	37543
CCSD[a]	20638	CCSD(T)[a]	20851

[a] at B3LYP/def2-TZVPP geometry
[b] at BP/def2-SVP geometry

5.5. Phosphorescence Spectra in Neon Matrix

As a final note to this chapter I would like to comment on some other experimental results. Up to this point all the spectra discussed in this chapter were measured in the gas-phase. Alternatively the measurement can also be done at very low temperatures in neon matrices.[126] The advantage of this approach is that the spectra measured have better signal-to-noise ratio. It was shown that the effects of neon matrices to the spectrum itself are minimal.[126]

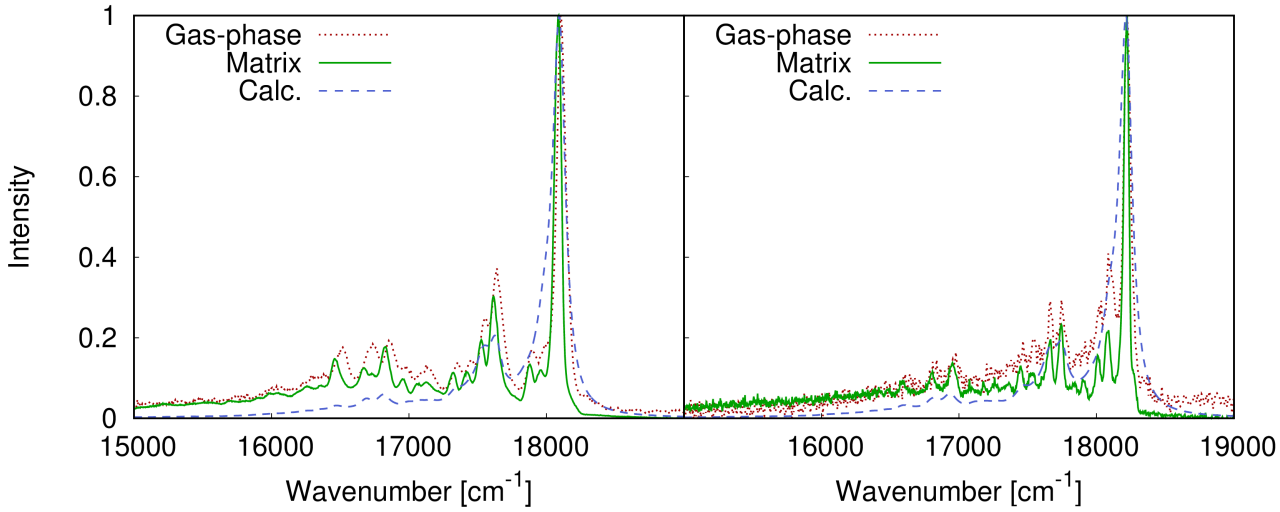

Figure 5.6: Comparison of the gas-phase and matrix measurements of $[Gd(PLN)_2]^+$ (left) and $[Lu(PLN)_2]^+$ (right) and the computations at the B3LYP/def2-TZVPP level of theory with large core ECP. The computed spectra are shifted to match the experimental 0–0 transition.

Figure 5.6 shows a comparison of the gas-phase and matrix measurements of $[Gd(PLN)_2]^+$ and $[Lu(PLN)_2]^+$. We can see that the difference between the two experimental spectra is rather small and that the computation therefore also reasonably reproduces the spectra obtained in the matrix.

6. Auxiliary Basis Sets for Lanthanides

The performance of computer systems has been growing rapidly for the past decades and the speed of its growth is only declining slowly. This means that a calculation which was not feasible two years ago can probably be done now or in the near future with the resources available. One needs to keep in mind that calculations which had to be done at great expenses on large scientific computer systems can now be done (quite literally) by a cell phone (and not particularly 'smart' one). Bearing all this in mind the importance of efficiency in quantum chemical computations can still not be overestimated. While it might not be as important and crucial as in the pioneering ages of quantum chemistry efficient algorithms, useful approximations, and smart implementations still enable us to perform computations on large molecules, for long time scales in molecular dynamics and with high accuracy (or any combination of the three) helping us to understand the structure of the world around us.

When studying atoms and molecules one often needs to make a difficult choice between accuracy and cost. Methods which are considered accurate are often very time consuming and therefore costly while other less accurate methods can be performed significantly faster. A prime example from the first group of methods is the coupled-cluster (CC) theory and the *gold standard of computational chemistry* CCSD(T) method in particular. Despite being very accurate its steep scaling of $\mathcal{O}(\mathcal{N}^7)$ prevents it from being usable on large molecules. In the context of electronic structure theory a good example from the second group of methods would be density functional theory (DFT) with a GGA functional which provides an efficient way to calculate energies, geometries and other properties; its results however are generally not as reliable and often need to be compared with higher-level theory results (e.g. in small or model cases). A broad spectrum of methods is available nowadays to tackle problems of different size with different degrees of accuracy and reliability; nevertheless the desire for a very accurate and at the same time cheap method remains.

One way to approach this problem is to make use of the local properties of electron correlation as mentioned in section 2.4. Another approach is to use the resolution-of-identity (RI) approximation (also called density fitting). As already explained in section 2.4.1 a special set of *auxiliary* basis functions needs to be used to perform the RI calculations. In this chapter I will describe the development and optimization of such auxiliary basis sets for post-HF computations for the lanthanide atoms.

6.1. Effective Core Potentials for Lanthanides

Lanthanides are heavy atoms and contain between 58 and 71 electrons. It is therefore very common to use effective core potentials (ECPs) to describe the behavior of the core electrons. This enables us both to reduce the computational cost of the calculation and to include (to some extent) the relativistic effects in the core region to our computations, which may be significant for these heavy atoms. The detailed description of the core electrons, which usually do not contribute to the chemical bonding significantly, is lost. The core electrons are of course important in some special applications such as calculation of e.g. nuclear magnetic shielding constants or core-electron spectra, Auger electrons, or the intermolecular Coulomb decay. Still if we are interested in optimized geometries ECPs are an accurate and efficient option to use.

I already described ECPs in section 2.3.1 so I will focus on two different types of ECPs for lanthanides that I used in my computations. First is the 28 electron ECP [130] which is the default ECP accompanying the standard def2 basis sets for lanthanides. As its name suggests it replaces 28 electrons by the pseudopotential. This translates to replacing the $1s, 2s, 2p, 3s, 3p$, and $3d$ orbitals with pseudopotentials. It was shown that the $4s$ orbital needs to be included in the valence shell to reproduce the excitation energies correctly [130] and not in the ECP even though (according to the Aufbau principle) it should be lower in energy than $3d$. This small core ECP not only speeds up the calculations (since the number of electrons that need to be treated is almost halved) but more importantly recovers the most important part of the relativistic effects. These basis sets were used in calculations optimizing the auxiliary basis sets described in this chapter.

The second type of ECPs takes advantage of different oxidation states that usually occur in lanthanides. The most common oxidation state in lanthanides is III, less common are

oxidation states II and IV.[66] Since f-electrons typically do not contribute to chemical bonds special large core ECPs were developed that include the whole f-shell of lanthanides. These ECPs are fitted to reproduce the properties of the respective oxidation states.[128,129] They then include different numbers of electrons depending on the atom and oxidation state of interest ranging from 47 (48) for cerium in oxidation state III (II) to 59 (60) for ytterbium in oxidation state III (II). The most important advantage of these ECPs is their efficiency as the absence of f-electrons in the valence shell makes the atoms effectively closed shell. This drastically improves the convergence of the SCF procedure speeding up the whole computation in the process. The main disadvantage is their limited applicability to only molecules with lanthanides in the specific oxidation state (configuration).
In the following text I use the expressions 'small' or 'standard' ECP to refer to the first, 28 electron, type of ECPs and 'large' or 'large core' ECP to refer to the second type of 'oxidation state specific' ECPs.

6.2. Optimization of Auxiliary Basis Sets

Auxiliary basis sets typically contain functions with higher orbital quantum numbers l than the regular basis sets. For example the def2-TZVP basis for europium contains one g-function (i.e. $l = 4$) while the corresponding auxiliary basis set contains one k-function (i.e. $l = 7$). The number of functions in the auxiliary basis set must be changed manually during the optimization process and is determined by the trial and error method.
The optimization was done using the `cbasopt` script which is a part of the `ricc2` module of TURBOMOLE. The main ideas behind the RI approximation have already been explained in section 2.4.1. In the optimization process, however, we do not directly minimize the RI error as defined in equation (2.70) but a related quantity ΔI instead:[18]

$$\begin{aligned} \Delta I &= -\frac{1}{4}\sum_{i,a,j,b}\frac{|\langle ij||ab\rangle - \langle ij||ab\rangle_{\mathrm{RI}}|^2}{\epsilon_i + \epsilon_j - \epsilon_a - \epsilon_b} \\ &= 2\tilde{E} - E_{\mathrm{MP2}} - E_{\mathrm{RIMP2}}, \end{aligned} \tag{6.1}$$

where (cf. equations (2.65) and (2.69))

$$\tilde{E} = \sum_{\sigma_1,\sigma_2} \sum_{i,a\in\sigma_1} \sum_{j,b\in\sigma_2} t_{ij}^{ab}(ia|jb)_{\mathrm{RI}}. \tag{6.2}$$

It can be shown that $\Delta I \geq 0$ and $\Delta I = 0$ if $E_{\mathrm{MP2}} = E_{\mathrm{RIMP2}}$ making ΔI a very convenient property to optimize. The convergence threshold for ΔI was set to 10^{-6} and after the optimization the total RI error ΔRI was calculated for each atom; the desired error ΔRI should be lower than $50\,\mu E_{\mathrm{h}}$. To avoid linear dependencies and assure energy consistent auxiliary basis sets the following condition for ratios of orbital exponents α needs to be satisfied:

$$w_{\min} \leq \alpha_i^l / \alpha_{i+1}^l \leq w_{\max} \tag{6.3}$$

for all exponents α_i with the same orbital quantum numbers l. In my optimization the boundary values were $w_{\min} = 1.8$ and $w_{\max} = 10$. The optimization itself is automatized in the `cbasopt` script but the number and type of basis functions and the fulfillment of condition (6.3) need to be checked manually, which requires a considerable amount of micromanagement.

Since the cost of calculations grows with the growing size of the auxiliary basis set we want to keep the auxiliary basis small. But the RI error should be also smaller for large auxiliary basis sets (as large portion of the orbital basis set space can be spanned). The appropriate size of the auxiliary basis set N_{aux}, which balances the two requirements, is usually somewhere around $N_{\mathrm{aux}} \approx 4 - 5 \times N_{\mathrm{BF}}$ where N_{BF} is the size of the orbital basis set.[101,131] This was also the aimed size of the auxiliary basis sets I was optimizing.

Different orbital basis sets need different auxiliary basis sets and I was optimizing them for four different basis sets of the def2 series – def2-SVP, def2-TZVP, def2-TZVPP, and def2-QZVPP. For simplicity I will omit the prefix def2- from now on but unless stated otherwise the basis sets always belong to the def2- series. The composition of the final optimized auxiliary basis sets is summarized in the Appendix C and the final size of the respective auxiliary basis sets is presented in Table 6.1.

Table 6.1: Size of the auxiliary basis set. The ratio $N_{\mathrm{aux}}/N_{\mathrm{BF}}$ is presented for different basis sets of the def2 series. N_{aux} stands for the number of functions in the auxiliary basis set while N_{BF} stands for the number of functions in the orbital basis set.[132]

Atom	SVP	TZVP	TZVPP	QZVPP
Ce	4.50	4.13	4.21	3.98
Pr	4.50	4.13	4.21	4.07
Nd	4.85	4.42	4.36	4.30
Pm	4.50	4.13	4.21	4.07
Sm	4.50	4.13	4.21	3.98
Eu	4.59	4.20	4.21	4.07
Gd	4.50	4.30	4.36	4.30
Tb	4.50	4.13	4.21	4.07
Dy	4.50	4.13	4.21	4.07
Ho	4.50	4.13	4.21	4.07
Er	4.33	4.00	4.09	4.07
Tm	4.33	4.00	4.10	4.07
Yb	4.33	4.00	4.09	3.98
Lu	5.05	4.27	4.54	4.22

The desired size of $N_{\mathrm{aux}} \approx 4-5\times N_{\mathrm{BF}}$ was obtained for all basis sets with the only exception of the SVP basis set for lutetium which is slightly larger than 5. The ΔRI errors for the lanthanide atoms were smaller than $50\,\mu E_{\mathrm{h}}$ in all cases with the exception of the SVP basis set for erbium where the error was $53\,\mu E_{\mathrm{h}}$. Both our desired size and accuracy of the basis set were achieved. Now we need a convenient set of representative molecules on which we can test our auxiliary basis set.

6.3. Test Set of Molecules

A test set of 49 small molecules used to derive the orbital basis sets of the def2- series[133] was chosen as a starting point for a representative set of molecules containing lanthanides. To account for different oxidation states I added some molecules to this test set; namely molecules of type XF_4, where X stands for a lanthanide to account for the oxidation state

X(IV), molecules of type XF_3 and XCl_3 were added where necessary to account for the most important oxidation state X(III), and the oxidation state X(II) is represented by molecules of type XF_2 or XCl_2 and XO. The covalent molecules XH_2 and dimers X_2 were also added. The first step in construction of such a test set is to obtain geometries of the molecules. These were either taken directly from the original test set[133] or (for the new molecules) calculated at the BP/def2-QZVP level of theory in order to be consistent within the test set. It is crucial to find the correct ground state (i.e. the state with lowest energy) which can be difficult for open shell systems. I used the fractional occupation approach[134] to find such a state for every molecule of the test set. First the calculation with fractional occupations was done at the BP/def2-QZVP level before optimization of the geometry. After the geometries were obtained a separate search for the ground state was performed for all four basis sets (again using the BP functional). If the occupations with the lowest energy would differ for different basis sets the occupation from the largest basis set (i.e. QZVPP) was used for all subsequent calculations. I took advantage of molecular symmetry where possible and I used the RI approximation for the Coulomb part of DFT for all calculations. The computations were performed using grid 5 of TURBOMOLE. With the geometries and electron occupations at hand I could perform the HF calculations that provided me with starting molecular orbitals for the MP2 calculations. There were serious problems in SCF convergence for some molecules and no stable occupation at the BP and/or HF level was obtained. These molecules (many of them were compounds containing terbium) were excluded from the test set. The final test set then contained 103 molecules; namely: $CeCl_3$, CeF, CeF_2, CeF_3, CeF_4, CeH_2, CeO, Dy_2, $DyCl_3$, DyF, DyF_2, DyF_3, DyF_4, DyH_2, DyO, Er_2, $ErCl_2$, $ErCl_3$, ErCl, ErF_3, ErF_4, ErH_2, ErO, Eu_2, EuCl, $EuCl_3$, EuF_2, EuF_3, EuF_4, EuH_2, EuO, Gd_2, $GdCl_3$, GdF, GdF_2, GdF_3, GdF_4, GdH_2, GdO, $HoCl_2$, $HoCl_3$, HoF_3, HoF_4, HoH_2, HoO, Lu_2, Lu_2N, Lu_2O, $LuBr_3$, $LuCl_3$, LuF, LuF_2, LuF_3, LuF_4, LuH_2, LuH_3, LuI_3, LuO, NdCl, $NdCl_3$, NdF_3, NdF_4, NdH_2, NdO, $PmCl_3$, PmF, PmF_2, PmF_3, PmF_4, PmH_2, PmO, Pr_2, PrCl, $PrCl_3$, PrF_2, PrF_3, PrF_4, PrH_2, PrO, $SmCl_3$, SmF, SmF_2, SmF_3, SmF_4, SmH_2, SmO, TbF, TbF_4, TmCl, $TmCl_3$, TmF_2, TmF_3, TmF_4, TmH_2, TmO, Yb_2, YbCl, $YbCl_2$, $YbCl_3$, YbF_3, YbF_4, YbH_2, and YbO.

The list of all molecules as well as the multiplicities (i.e. numbers of unpaired electrons) and symmetries used in the calculations can be found in Appendix D. At this point finally MP2 and RIMP2 computations could be performed to test the auxiliary basis sets.

6.4. Performance of Auxiliary Basis Sets

In this section the performance of the auxiliary basis sets is benchmarked on the molecules from the test set presented in the previous section. Various errors are documented and the performance of the auxiliary basis sets with large core ECPs is tested as well.

6.4.1. Absolute Electronic Energies

The first and most straightforward thing to look at when assessing the performance of auxiliary basis set is to look at the error ΔRI introduced via the RI approximation. It is defined (as already stated by equation (2.70)) as:

$$\Delta\mathrm{RI} = |E_{\mathrm{MP2}} - E_{\mathrm{RIMP2}}|, \tag{6.4}$$

where E_{MP2} and E_{RIMP2} stand for the MP2 energy without and with using the RI approximation, respectively.

We can calculate the error ΔRI per atom for each molecule and each basis set. Then one can conveniently divide the molecules into groups depending on the size of the error, e.g. groups with error smaller than $20\,\mu E_{\mathrm{h}}$, smaller than $40\,\mu E_{\mathrm{h}}$, smaller than $60\,\mu E_{\mathrm{h}}$ and so on and get histograms for each basis set. Such a histogram is presented in Figure 6.1.

It is to be expected from a good basis set that the error gets smaller if the basis set gets larger. This translates into larger portion of molecules being in a group with smaller error. This is exactly what we observe as e.g. the number of molecules with error lower than $20\,\mu E_{\mathrm{h}}$ grows from 49 (48 %) for the SVP basis set to 96 (93 %) for the QZVPP basis set. The only molecule with an error ΔRI per atom consistently larger than $100\,\mu E_{\mathrm{h}}$ is the dysprosium dimer Dy_2, which was therefore excluded from the statistics presented in the following sections.

One can also present the relative RI errors[131] as shown in Table 6.2 where the standard deviation $\Delta_{\mathrm{std}} = \sqrt{\frac{1}{n-1}\sum_{i=1}^{n}(\Delta_i - \bar{\Delta})^2}$, the mean absolute error $|\Delta| = (1/n)\sum_{i=1}^{n}|\Delta_i|$, and the maximum of the absolute error $|\Delta|_{\max} = \max|\Delta_i|$ are calculated from only the *correlation* energies at the MP2 and RIMP2 level of theory, i.e. $\Delta_i = (E^{\mathrm{corr}}_{\mathrm{MP2}} - E^{\mathrm{corr}}_{\mathrm{RIMP2}})/E^{\mathrm{corr}}_{\mathrm{MP2}} \times 100$. The 'worst case' column lists the molecules with the largest relative error for the given basis set. Again it is apparent that the errors get smaller for larger basis sets.

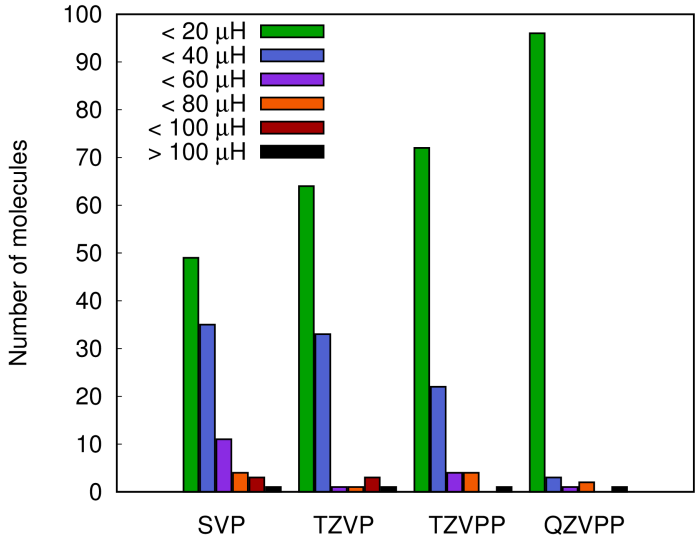

Figure 6.1: Errors due to the RI approximation for different basis sets. The y-axis shows how many molecules have the error ΔRI per atom smaller than given threshold.[132]

Table 6.2: The relative RI errors in %. See the text for further explanation.[132]

Auxiliary basis set	Δ_{std}	$\lvert\Delta\rvert$	$\lvert\Delta_{\text{max}}\rvert$	Worst case
SVP	0.013	0.010	0.057	CeH_2
TZVP	0.011	0.007	0.058	CeH_2
TZVPP	0.007	0.005	0.036	CeH_2
QZVPP	0.004	0.002	0.007	Pr_2

Tables with explicit ΔRI errors for each molecule and basis set can be found in Appendix E.

6.4.2. Atomization Energies

The ΔRI errors illustrate well the performance of the RI approximation. However, more interesting from the chemical point of view are the bond energies or atomization energies. In this section we will see the difference between the atomization energies computed with the proposed auxiliary basis sets and atomization energies computed without the RI approximation.

Given a compound of type X_aY_b and its (theoretical) decomposition to elements

$$X_aY_b \longrightarrow aX + bY,$$

the reaction energy E_r of this reaction is called atomization energy E_at and is defined as

$$E_\mathrm{at} = aE_\mathrm{X} + bE_\mathrm{Y} - E_{\mathrm{X}_a\mathrm{Y}_b}. \tag{6.5}$$

It is consistent to define the difference ΔE_at

$$\Delta E_\mathrm{at} = E_\mathrm{at,MP2} - E_\mathrm{at,RIMP2}, \tag{6.6}$$

where $E_\mathrm{at,MP2}$ and $E_\mathrm{at,RIMP2}$ denote the atomization energy calculated at the MP2 level of theory without and with using the RI approximation, respectively. This difference is a measure of the RI error of atomization energies. We can calculate ΔE_at for each molecule in the test set (note that we have already excluded the dysprosium dimer Dy_2 from the statistics). The values of ΔE_at per atom are presented in Figure 6.2.

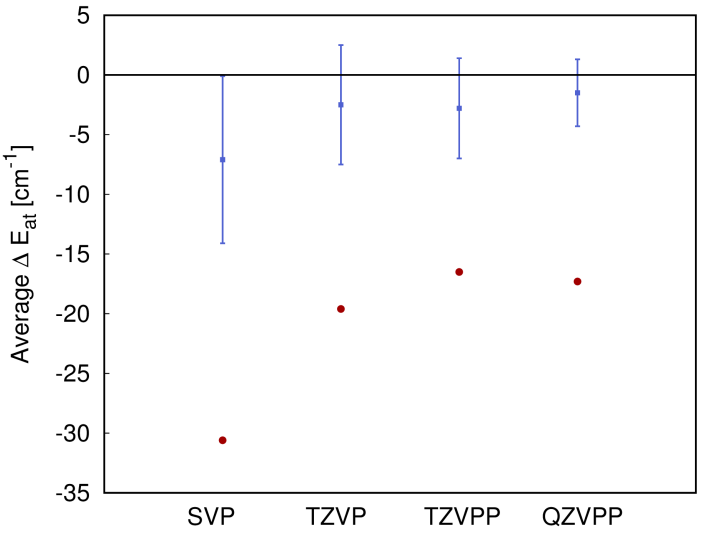

Figure 6.2: Errors of atomization energies (ΔE_at) per atom introduced by the RI approximation at the MP2 level of theory in cm^{-1}. The average errors as well as the standard deviations are presented (blue bars) and so are the maximal errors (red points). The dysprosium dimer Dy_2 was excluded from this graph (see text). The maximal errors correspond to CeO, SmF, SmF, and NdCl for the SVP, TZVP, TZVPP, and QZVPP basis sets, respectively.

The errors are rather small (the values presented are in cm^{-1}) and one can again see that the standard deviation gets smaller as the basis set size grows. It seems that the proposed auxiliary basis sets perform well in calculations of atomization energies as well. The last

open question is if, apart from the standard ECPs, they can also be used with the large ECPs. We will have a look at this problem in the following section.
Tables with explicit ΔE_{at} errors for each molecule and basis set can be found in Appendix F.

6.4.3. Performance with different ECPs

The large core ECPs were derived to describe appropriately the electronic configurations that contribute to the oxidation states (II) and (III) of lanthanides. To test the performance of the auxiliary basis sets with these ECPs appropriate subsets of the molecular test set need to be taken where lanthanides are in the corresponding oxidation state. For the oxidation state (III) the XF_3 and XCl_3 molecules were taken; for the oxidation state (II) XF_2, XCl_2, and XO molecules were taken. For all these molecules the absolute electronic energy was calculated at the MP2 and RIMP2 levels of theory and the error ΔRI was calculated.
In case of the oxidation state (III) all ΔRI errors were smaller than $20\,\mu E_{\mathrm{h}}$ and for the largest QZVPP basis set all ΔRI errors were smaller than $5\,\mu E_{\mathrm{h}}$. For the oxidation state (II) the results were also very good as only for CeO with the small SVP basis the ΔRI error was larger than $20\,\mu E_{\mathrm{h}}$. These very small errors show that the auxiliary basis sets can be used as they are and without modification for calculations with the large core ECPs.
The complete tables with all ΔRI errors in computations with large ECPs can be found in Appendix G.

6.5. Conclusions

The goal of this chapter was to document how an auxiliary basis set for post-HF computations can be developed and tested for a set of atoms (in this case lanthanides). In comparison to the rest of this thesis the development of such a basis set is more of a technical problem and its importance is more difficult to see and therefore the question arises how do these basis sets help us?
The answer is they make calculations possible that would not have been feasible without them. The benefits that are obtained using e.g. the RIMP2 method outweigh the inconvenience of the additional error, which is small anyway as documented in this chapter, that is connected with the RI approximation. MP2 and CC calculations were done using these

auxiliary basis sets on quite large systems already in this thesis that could not have been done otherwise. The results of these calculations helped me further understand the problems I was facing giving some more reliable data. Now they can be routinely used to tackle problems containing lanthanides at higher-levels of theory employing the RI approximation.

7. Summary

In this thesis the optical properties of mono- and multi-nuclear complexes with transition metal or lanthanide centers were studied using various methods of computational chemistry. The complexes containing lanthanides and/or transition metals are of chemical interest for the role they play in catalysis and optical devices. There is a potential for compounds with several metal centers to be usable in complex optical devices used in e.g. photon conversion. The differential many-body expansion was used to define cooperativity between metal centers in covalently bound complexes in a quantifiable and consistent way. Cooperativity is expressed as three- and higher-body contributions to the property in the many-body expansion. This definition was applied to the decomposition of absorption spectra of two complexes – a homotrinuclear complex with three Pd atoms and a homotrinuclear complex with three Rh atoms. The absorption spectra in the complexes were computed using the approximate sTDDFT method.[62] The cooperativity between the metal centers was studied by replacing Pd with Pt in the first complex and by replacing Rh with Ir in the second complex. Strong cooperativity was found in the Pd_3 complex while very small to negligible cooperativity was found in the Rh_3 complex. Furthermore the cooperativity in transition densities was also studied in the Rh_3 complex supporting the results of low cooperativity obtained for the absorption spectrum. It was concluded that the amount of cooperativity is related to the distance between the metal centers as the metals in the Pd_3 complex which were close together showed much larger cooperativity than metal centers in the Rh_3 complex that were further apart. At this point we are in search of a suitable complex with three or more metal centers where cooperativity would be larger than in the case of Rh_3 complex but smaller than in the Pd_3 complex so that meaningful chemical interpretations for cooperativity could be drawn.

Two types of complexes of Eu^{3+} were studied using the DFT optimizations and ligand field computations together with experimental techniques of luminescence spectroscopy and ion

mobility spectroscopy. In these gas-phase studies first the experimentally formed optical transitions of a nonanuclear complex were used to find a new set of parameters for the effective ligand field Hamiltonian.[115] These improved parameters then resulted in better agreement between experimental and computed transitions in gas-phase studies of three and four ligand systems.[105,109] The dependence between luminescence and molecular structure was studied in a series of four ligand systems of type $[Eu(PLN)_4AE]^+$ with AE = Mg, Ca, and Sr. Two types of structures were found that both reproduced the experimental spectrum satisfactorily. The influence of the D3 dispersion correction[49] of DFT on the computed geometries was studied in detail and unphysical stacking of PLN ligands was found for the BP functional when used together with the D3 correction. Our benchmark computations suggest that the B2PLYP functional could be an accurate and efficient method for future investigation of this stacking. To assign the structure of the four ligand series complexes unambiguously further advances are needed on both the experimental and the theoretical side.

To shed light on the competing processes in lanthanide complexes, phosphorescence of the PLN ligand was studied in the $[Gd(PLN)_2]^+$ and the $[Lu(PLN)_2]^+$ complexes. Structures of D_{2d} symmetry were found for both of them for the S_0 and T_1 states. The Franck-Condon spectra were computed and found to be in good agreement with the experimental spectra measured in gas-phase and neon matrices. The shift between the 0–0 transitions of the $[Gd(PLN)_2]^+$ and the $[Lu(PLN)_2]^+$ complexes, which depends on the energy separation of the S_0 and T_1 states, was computed using different DFT functionals and also employing coupled-cluster theory. We reached a reasonable agreement with experiment, however, the discrepancies in individual 0–0 transitions are still large ($\approx 2000\,\mathrm{cm}^{-1}$ even for the CCSD(T) computation with def2-TZVPP basis set). Further computations are needed to explain them.

New auxiliary basis sets needed to be developed for the computations at the CCSD(T) level of theory that were mentioned in the previous paragraph. Auxiliary basis sets for the SVP, TZVP, TZVPP, and QZVPP orbital basis sets of the def2- series were developed for all lanthanide atoms. They were tested using the enlarged test set (103 molecules) of small molecules used to derive the orbital basis set.[133] The benchmark computations showed acceptable errors that were introduced in the RIMP2 energies compared to the full MP2 method for both the absolute electronic energies and the atomization energies of the

molecules in the test set. The developed auxiliary basis sets can be used in combination with both the standard 28 electron ECPs[130] and the large core ECPs[128,129] making computations on the MP2 and coupled-cluster level of theory available for mid-sized molecules containing lanthanide atoms.
Some of the future studies that need to be done were already mentioned – finding the suitable metal complex for chemically useful interpretation of cooperativity, further refinement of experimental and theoretical approaches to the structural study of four ligand systems, and the explanation of disagreement between experimental and computed 0–0 transitions in the $[Gd(PLN)_2]^+$ and the $[Lu(PLN)_2]^+$ complexes. Other scientifically interesting projects include the further study (experimental and theoretical) of a series of $[X(PLN)_2]^+$ complexes where X stands for any lanthanide. The study of energy transfer from the ligand to the metal center is also of interest especially with respect to the design of possible photon conversion devices.

Most of the projects presented in this thesis show the need for a combined effort of experiment and theory. It is clear that future research as indicated above has to follow the same strategy in order to contribute to a better understanding of the optical properties of transition metal and lanthanide containing complexes.

Bibliography

[1] Fordham, S.; Wang, X.; Bosch, M. and Zhou, H.-C., In *Lanthanide Metal-Organic Frameworks*, Cheng, P., Ed., Springer Berlin Heidelberg, Berlin, Heidelberg, 2015; pages 1–27.

[2] Cui, Y.; Yue, Y.; Qian, G. and Chen, B., *Chem. Rev.*, 2012, **112**(2), 1126–1162.

[3] Ren, Y.; Liang, J.; Lu, J.; Cai, B.; Shi, D.; Qi, C.; Jiang, H.; Chen, J. and Zheng, D., *Eur. J. Inorg. Chem.*, 2011, **2011**(28), 4369–4376.

[4] Díez-González, S.; Marion, N. and Nolan, S. P., *Chem. Rev.*, 2009, **109**(8), 3612–3676.

[5] Zhong, C. and Shi, X., *Eur. J. Org. Chem.*, 2010, **2010**(16), 2999–3025.

[6] *Nat. Chem. Biol.*, 2008, **4**(8), 433–433.

[7] Richard, R. M.; Lao, K. U. and Herbert, J. M., *Acc. Chem. Res.*, 2014, **47**(9), 2828–2836.

[8] Kido, J.; Nagai, K. and Ohashi, Y., *Chem. Lett.*, 1990, **19**(4), 657–660.

[9] Kido, J.; Hayase, H.; Hongawa, K.; Nagai, K. and Okuyama, K., *Appl. Phys. Lett.*, 1994, **65**(17), 2124–2126.

[10] Kido, J. and Okamoto, Y., *Chem. Rev.*, 2002, **102**(6), 2357–2368.

[11] Kuriki, K.; Koike, Y. and Okamoto, Y., *Chem. Rev.*, 2002, **102**(6), 2347–2356.

[12] Oh, D.; Song, N. and Kim, J.-J., *Proc. SPIE*, 2001, **4282**, 1–8.

[13] Fang, J.; You, H.; Chen, J.; Lin, J. and Ma, D., *Inorg. Chem.*, 2006, **45**(9), 3701–3704.

[14] Han, S.; Deng, R.; Xie, X. and Liu, X., *Angew. Chem. Int. Ed.*, 2014, **53**(44), 11702–11715.

[15] DaCosta, M. V.; Doughan, S.; Han, Y. and Krull, U. J., *Anal. Chim. Acta*, 2014, **832**, 1–33.

[16] Yu, D.-C.; Martin-Rodriguez, R.; Zhang, Q.-Y.; Meijerink, A. and Rabouw, F. T., *Light Sci Appl*, 2015, **4**, e344.

[17] Møller, C. and Plesset, M. S., *Phys. Rev.*, 1934, **46**, 618–622.

[18] Weigend, F.; Häser, M.; Patzelt, H. and Ahlrichs, R., *Chem Phys Lett*, 1998, **294**(1–3), 143–152.

[19] Cramer, C. J., *Essentials of Computational Chemistry: Theories and Models*, Wiley, Chichester, 2004.

[20] Szabo, A. and Ostlund, N. S., *Modern quantum chemistry: introduction to advanced electronic structure theory*, McGraw-Hill, New York, 1989.

[21] Koch, W. and Holthausen, M. C., *A Chemist's Guide to Density Functional Theory*, Wiley, Weinheim, 2000.

[22] Reine, S. and Saue, T., *European Summerschool in Quantum Chemistry 2015*, 2015.

[23] Born, M. and Oppenheimer, R., *Ann. Phys.*, 1927, **389**(20), 457–484.

[24] Almlöf, J.; Ahlrichs, R. and Klopper, W. In *European Summerschool in Quantum Chemistry 2015*, Reine, S. and Saue, T., Eds.; 2015; chapter 4.

[25] Raghavachari, K.; Trucks, G. W.; Pople, J. A. and Head-Gordon, M., *Chem. Phys. Lett.*, 1989, **157**(6), 479–483.

[26] Cremer, D., *WIREs Comput. Mol. Sci.*, 2011, **1**(4), 509–530.

[27] Binkley, J. S. and Pople, J. A., *Int. J. Quantum Chem.*, 1975, **9**(2), 229–236.

[28] Čížek, J., *J. Chem. Phys.*, 1966, **45**(11), 4256–4266.

[29] Taylor, P. R. In *European Summerschool in Quantum Chemistry 2015*, Reine, S. and Saue, T., Eds.; 2015; chapter 6.

[30] Köhn, A., *Analytische Gradienten elektronisch angeregter Zustände und Behandlung offenschaliger Systeme im Rahmen der Coupled-Cluster-Methode RI-CC2*, Cuvillier Verlag, Göttingen, 2003.

[31] Purvis, G. D. and Bartlett, R. J., *J. Chem. Phys.*, 1982, **76**(4), 1910–1918.

[32] Ahlrichs, R.; Bär, M.; Häser, M.; Horn, H. and Kölmel, C., *Chem. Phys. Lett.*, 1989, **162**, 165–169.

[33] TURBOMOLE V7.0, a development of University of Karlsruhe and Forschungszentrum Karlsruhe GmbH, 1989-2007, TURBOMOLE GmbH, since 2007; available from `http://www.turbomole.com`., 2015.

[34] Furche, F.; Ahlrichs, R.; Hättig, C.; Klopper, W.; Sierka, M. and Weigend, F., *WIREs Comput. Mol. Sci.*, 2014, **4**(2), 91–100.

[35] Becke, A. D., *J. Chem. Phys.*, 2014, **140**(18), 18A301.

[36] Hohenberg, P. and Kohn, W., *Phys. Rev.*, 1964, **136**, B864–B871.

[37] Tozer, D. J. In *European Summerschool in Quantum Chemistry 2015*, Reine, S. and Saue, T., Eds.; 2015; chapter 10.

[38] Kohn, W. and Sham, L. J., *Phys. Rev.*, 1965, **140**, A1133–A1138.

[39] Ullrich, C., *Time-Dependent Density-Functional Theory: Concepts and Applications*, Oxford University Press, New York, 2012.

[40] Perdew, J. P.; Ruzsinszky, A.; Constantin, L. A.; Sun, J. and Csonka, G. I., *J. Chem. Theory Comput.*, 2009, **5**(4), 902–908.

[41] Becke, A. D., *Phys. Rev. A*, 1988, **38**, 3098–3100.

[42] Vosko, S. H.; Wilk, L. and Nusair, M., *Can. J. Phys.*, 1980, **58**(8), 1200–1211.

[43] Perdew, J. P., *Phys. Rev. B*, 1986, **33**, 8822–8824.

[44] Becke, A. D., *J. Chem. Phys.*, 1993, **98**, 5648–5652.

[45] Harris, J., *Phys. Rev. A*, 1984, **29**, 1648–1659.

[46] Lee, C.; Yang, W. and Parr, R. G., *Phys. Rev. B*, 1988, **37**, 785–789.

[47] Grimme, S., *J. Chem. Phys.*, 2006, **124**(3), 034108.

[48] Grimme, S., *J. Comput. Chem.*, 2004, **25**(12), 1463–1473.

[49] Grimme, S.; Antony, J.; Ehrlich, S. and Krieg, H., *J. Chem. Phys.*, 2010, **132**(15), 154104.

[50] Grimme, S.; Ehrlich, S. and Goerigk, L., *J. Comput. Chem.*, 2011, **32**(7), 1456–1465.

[51] Runge, E. and Gross, E. K. U., *Phys. Rev. Lett.*, 1984, **52**, 997–1000.

[52] Casida, M. E., *J. Mol. Struct.- THEOCHEM*, 2009, **914**(1–3), 3–18.

[53] Petersilka, M.; Gossmann, U. J. and Gross, E. K. U., *Phys. Rev. Lett.*, 1996, **76**, 1212–1215.

[54] Hirata, S. and Head-Gordon, M., *Chem. Phys. Lett.*, 1999, **314**(3–4), 291–299.

[55] Wiberg, K. B.; Stratmann, R. and Frisch, M. J., *Chem. Phys. Lett.*, 1998, **297**(1–2), 60–64.

[56] Tozer, D. J.; Amos, R. D.; Handy, N. C.; Roos, B. O. and Serrano-Andrés, L., *Mol. Phys.*, 1999, **97**(7), 859–868.

[57] Yanai, T.; Tew, D. P. and Handy, N. C., *Chem. Phys. Lett.*, 2004, **393**(1–3), 51–57.

[58] Peach, M. J. G.; Benfield, P.; Helgaker, T. and Tozer, D. J., *J. Chem. Phys.*, 2008, **128**(4), 044118.

[59] Christiansen, O.; Koch, H. and Jørgensen, P., *Chem. Phys. Lett.*, 1995, **243**(5), 409–418.

[60] Grimme, S., *J. Chem. Phys.*, 2013, **138**, 244104.

[61] Löwdin, P.-O., *J. Chem. Phys.*, 1950, **18**(3), 365–375.

[62] Bannwarth, C. and Grimme, S., *Comput. Theor. Chem.*, 2014, **1040–1041**, 45–53.

[63] Pyykkö, P., *Chem. Rev.*, 1988, **88**(3), 563–594.

[64] Pyykkö, P., *Annu. Rev. Phys. Chem.*, 2012, **63**(1), 45–64.

[65] Dolg, M. and Cao, X., *Chem. Rev.*, 2012, **112**(1), 403–480.

[66] Hehlen, M. P.; Brik, M. G. and Krämer, K. W., *J. Lumin.*, 2013, **136**, 221–239.

[67] Condon, E. U. and Shortley, G. H., *The Theory of Atomic Spectra*, The University Press, Cambridge, 1963.

[68] Holzer, C.; Wernbacher, A. M.; Senekowitsch, J. M.; Gatterer, K. and Kelterer, A.-M., *J. Phys. Chem. A*, 2014, **118**(49), 11499–11511.

[69] Racah, G., *Phys. Rev.*, 1942, **61**, 186–197.

[70] Racah, G., *Phys. Rev.*, 1942, **62**, 438–462.

[71] Racah, G., *Phys. Rev.*, 1943, **63**, 367–382.

[72] Racah, G., *Phys. Rev.*, 1949, **76**, 1352–1365.

[73] Elliott, J. P.; Judd, B. R. and Runciman, W. A., *Proc. R. Soc. London, Ser. A*, 1957, **240**(1223), 509–523.

[74] Nielsen, C. W. and Koster, G. F., *Spectroscopic Coefficients for the p, d, and f Configurations*, The MIT Press, Cambridge, 1963.

[75] Stevens, K. W. H., *Proc. Phys. Soc. , Sect A*, 1952, **65**(3), 209.

[76] Rotter, M.; Le, M. D.; Boothroyd, A. T. and Blanco, J. A., *J. Phys.: Condens. Matter*, 2012, **24**(21), 213201.

[77] Pulay, P. and Saebø, S., *Theor. Chim. Acta*, 1986, **69**(5), 357–368.

[78] Schütz, M. and Werner, H.-J., *J. Chem. Phys.*, 2001, **114**(2), 661–681.

[79] Li, S.; Shen, J.; Li, W. and Jiang, Y., *J. Chem. Phys.*, 2006, **125**(7), 074109.

[80] Kristensen, K.; Ziółkowski, M.; Jansík, B.; Kjærgaard, T. and Jørgensen, P., *J. Chem. Theory Comput.*, 2011, **7**(6), 1677–1694.

[81] Pinski, P.; Riplinger, C.; Valeev, E. F. and Neese, F., *J. Chem. Phys.*, 2015, **143**(3), 034108.

[82] Friedrich, J., *J. Chem. Theory Comput.*, 2015, **11**(8), 3596–3609.

[83] Vahtras, O.; Almlöf, J. and Feyereisen, M., *Chem. Phys. Lett.*, 1993, **213**(5), 514–518.

[84] Schinke, R., *Photodissociation Dynamics*, Cambridge University Press, Cambridge, 1993.

[85] Franck, J. and Dymond, E. G., *Trans. Faraday Soc.*, 1926, **21**, 536–542.

[86] Condon, E., *Phys. Rev.*, 1926, **28**, 1182–1201.

[87] Atkins, P. W. and S., F. R., *Molecular Quantum Mechanics*, Oxford University Press, New York, 1997.

[88] Berger, R.; Fischer, C. and Klessinger, M., *J. Phys. Chem. A*, 1998, **102**(36), 7157–7167.

[89] Xu, J.; Radkov, E.; Ziegler, M. and Raymond, K. N., *Inorg. Chem.*, 2000, **39**(18), 4156–4164.

[90] Kepert, D. L. In *Progr. in Inorg. Chem., Vol. 24*, Lippard, S. J., Ed.; Wiley, New York, 1978; chapter 4.

[91] Muetterties, E. L. and Guggenberger, L. J., *J. Am. Chem. Soc.*, 1974, **96**(6), 1748–1756.

[92] van Wüllen, C., *Mol. Phys.*, 2013, **111**(16-17), 2392–2397.

[93] Taghizadeh Ghoochany, L.; Kerner, C.; Farsadpour, S.; Menges, F.; Sun, Y.; Niedner-Schatteburg, G. and Thiel, W. R., *Eur. J. Inorg. Chem.*, 2013, **2013**(24), 4305–4317.

[94] Styra, S.; González-Gallardo, S.; Armbruster, F.; Oña-Burgos, P.; Moos, E.; Vonderach, M.; Weis, P.; Hampe, O.; Grün, A.; Schmitt, Y.; Gerhards, M.; Menges, F.; Gaffga, M.; Niedner-Schatteburg, G. and Breher, F., *Chem. Eur. J.*, 2013, **19**(26), 8436–8446.

[95] Nelson, D. L.; Cox, M. M. and Lehninger, A. L., *Lehninger principles of biochemistry*, Freeman, New York, 2013.

[96] Voet, D. and Voet, J. G., *Biochemistry*, Wiley, New York, 2004.

[97] Muck-Lichtenfeld, C. and Grimme, S., *Dalton Trans.*, 2012, **41**, 9111–9118.

[98] Klopper, W.; Quack, M. and Suhm, M. A., *Mol. Phys.*, 1998, **94**(1), 105–119.

[99] Schmitt, Y.; Chevalier, K.; Rupp, F.; Becherer, M.; Grun, A.; Rijs, A. M.; Walz, F.; Breher, F.; Diller, R.; Gerhards, M. and Klopper, W., *Phys. Chem. Chem. Phys.*, 2014, **16**, 8332–8338.

[100] Zimmer, M.; Rupp, F.; Singer, P.; Walz, F.; Breher, F.; Klopper, W.; Diller, R. and Gerhards, M., *Phys. Chem. Chem. Phys.*, 2015, **17**, 14138–14144.

[101] Weigend, F.; Häser, M.; Patzelt, H. and Ahlrichs, R., *Chem. Phys. Lett.*, 1998, **294**, 143–152.

[102] Weigend, F. and Ahlrichs, R., *Phys. Chem. Chem. Phys.*, 2005, **7**, 3297–3305.

[103] Chmela, J.; Harding, M. E.; Matioszek, D.; Anson, C. E.; Breher, F. and Klopper, W., *ChemPhysChem*, 2016, **17**(1), 37–45.

[104] Martin, R. L., *J. Chem. Phys.*, 2003, **118**(11), 4775–4777.

[105] Greisch, J.-F.; Harding, M. E.; Schäfer, B.; Rotter, M.; Ruben, M.; Klopper, W.; Kappes, M. M. and Schooss, D., *J. Phys. Chem. A*, 2014, **118**, 94–102.

[106] DeShazer, L. G. and Dieke, G. H., *J. Chem. Phys.*, 1963, **38**(9), 2190–2199.

[107] Deun, R. V.; Nockemann, P.; Fias, P.; Hecke, K. V.; Meervelt, L. V. and Binnemans, K., *Chem. Commun.*, 2005, pages 590–592.

[108] Greisch, J.-F.; Harding, M. E.; Schäfer, B.; Ruben, M.; Klopper, W.; Kappes, M. M. and Schooss, D., *J. Phys. Chem. Lett.*, 2014, **5**, 1727–1731.

[109] Greisch, J.-F.; Chmela, J.; Harding, M. E.; Wunderlich, D.; Schäfer, B.; Ruben, M.; Klopper, W.; Schooss, D. and Kappes, M. M., *Phys. Chem. Chem. Phys.*, submitted.

[110] Freire, R. O. and Simas, A. M., *J. Chem. Theory Comput.*, 2010, **6**(7), 2019–2023.

[111] Von Arnim, M. and Ahlrichs, R., *J. Comput. Chem.*, 1998, **19**(15), 1746–1757.

[112] van Wüllen, C., *J. Comput. Chem.*, 2011, **32**(6), 1195–1201.

[113] Wiberg, K. B. and Rablen, P. R., *J. Comput. Chem.*, 1993, **14**(12), 1504–1518.

[114] Reed, A. E.; Weinstock, R. B. and Weinhold, F., *J. Chem. Phys.*, 1985, **83**(2), 735–746.

[115] Greisch, J.-F.; Chmela, J.; Harding, M. E.; Klopper, W.; Kappes, M. M. and Schooss, D., *Inorg. Chem.*, 2016, **55**(7), 3316–3323.

[116] Carnall, W. T.; Goodman, G. L.; Rajnak, K. and Rana, R. S., *J. Chem. Phys.*, 1989, **90**(7), 3443–3457.

[117] Binnemans, K., *Coord. Chem. Rev.*, 2015, **295**, 1–45.

[118] Kordel, M.; Schooss, D.; Neiss, C.; Walter, L. and Kappes, M. M., *J. Phys. Chem. A*, 2010, **114**(17), 5509–5514.

[119] Kristyán, S. and Pulay, P., *Chem. Phys. Lett.*, 1994, **229**(3), 175–180.

[120] Chmela, J.; Greisch, J.-F.; Klopper, W. and Harding, M. E., *manuscript in preparation.*

[121] Maron, L. and Eisenstein, O., *J. Phys. Chem. A*, 2000, **104**(30), 7140–7143.

[122] Siu, C.-K.; Guo, Y.; Saminathan, I. S.; Hopkinson, A. C. and Siu, K. W. M., *J. Phys. Chem. B*, 2010, **114**(2), 1204–1212.

[123] Campuzano, I.; Bush, M. F.; Robinson, C. V.; Beaumont, C.; Richardson, K.; Kim, H. and Kim, H. I., *Anal. Chem.*, 2012, **84**(2), 1026–1033.

[124] Dieke, G. H. and Crosswhite, H. M., *Appl. Opt.*, 1963, **2**(7), 675–686.

[125] Peijzel, P.; Meijerink, A.; Wegh, R.; Reid, M. and Burdick, G., *J. Solid State Chem.*, 2005, **178**(2), 448–453.

[126] Kern, B.; Greisch, J.-F.; Strelnikov, D.; Weis, P.; Böttcher, A.; Ruben, M.; Schäfer, B.; Schooss, D. and Kappes, M. M., *Anal. Chem.*, 2015, **87**(23), 11901–11906.

[127] Waldt, E.; Greisch, J.-F.; Chmela, J.; Harding, M. E.; Klopper, W. and Schooss, D., *manuscript in preparation.*

[128] Dolg, M.; Stoll, H.; Savin, A. and Preuss, H., *Theor. Chim. Acta*, 1989, **75**(3), 173–194.

[129] Dolg, M.; Stoll, H. and Preuss, H., *Theor. Chim. Acta*, 1993, **85**(6), 441–450.

[130] Dolg, M.; Stoll, H. and Preuss, H., *J. Chem. Phys.*, 1989, **90**(3), 1730–1734.

[131] Hellweg, A.; Hättig, C.; Höfener, S. and Klopper, W., *Theor. Chem. Acc.*, 2007, **117**(4), 587–597.

[132] Chmela, J. and Harding, M. E., *manuscript in preparation.*

[133] Gulde, R.; Pollak, P. and Weigend, F., *J. Chem. Theory Comput.*, 2012, **8**(11), 4062–4068.

[134] Nava, P.; Sierka, M. and Ahlrichs, R., *Phys. Chem. Chem. Phys.*, 2003, **5**, 3372–3381.

A. Notations for Integrals

It was called an "unfortunate fact of life" [20] that there exist different notations for electronic integrals. Also in this thesis different notations are used. [24]

In the Dirac (*bra-ket*, physicist) notation we write (for spin–orbitals $\varphi_p, \varphi_q, \varphi_r, \varphi_s$ and a general operator $\hat{A}$):

$$\langle p|q\rangle \equiv \langle \varphi_p|\varphi_q\rangle \equiv \int \varphi_p^*(\mathbf{x})\varphi_q(\mathbf{x})\,\mathrm{d}\mathbf{x}, \tag{A.1}$$

$$\langle p|\hat{A}|q\rangle \equiv \langle \varphi_p|\hat{A}|\varphi_q\rangle \equiv \int \varphi_p^*(\mathbf{x})\hat{A}\varphi_q(\mathbf{x})\,\mathrm{d}\mathbf{x}, \tag{A.2}$$

$$\langle pr|\hat{A}|qs\rangle \equiv \langle \varphi_p\varphi_r|\hat{A}|\varphi_q\varphi_s\rangle \equiv \iint \varphi_p^*(\mathbf{x})\varphi_r^*(\mathbf{y})\hat{A}\varphi_q(\mathbf{x})\varphi_s(\mathbf{y})\,\mathrm{d}\mathbf{x}\,\mathrm{d}\mathbf{y}. \tag{A.3}$$

For a special case of repulsion integral where $\hat{A} = \frac{1}{r_{12}}$ we write:

$$\left\langle pr \left| \frac{1}{r_{12}} \right| qs \right\rangle \equiv \langle pr|qs\rangle. \tag{A.4}$$

It is also common to use the following shorthanded notation:

$$\langle pr||qs\rangle \equiv \langle pr|qs\rangle - \langle pr|sq\rangle. \tag{A.5}$$

For integrals over spatial orbitals $(\psi_p, \psi_q, \psi_r, \psi_s)$ the following convention is used:

$$(p|\hat{A}|q) \equiv \int \psi_p^*(\mathbf{r})\hat{A}\psi_q(\mathbf{r})\,\mathrm{d}\mathbf{r}, \tag{A.6}$$

$$(pq|rs) \equiv (\psi_p\psi_q|\psi_r\psi_s) \equiv \iint \psi_p^*(\mathbf{r}_1)\psi_q(\mathbf{r}_1)\frac{1}{r_{12}}\psi_r^*(\mathbf{r}_2)\psi_s(\mathbf{r}_2)\,\mathrm{d}\mathbf{r}_1\,\mathrm{d}\mathbf{r}_2. \tag{A.7}$$

From the above definitions it follows that e.g. $\langle pq|rs\rangle = (pr|qs)$ if the spin functions satisfy $\sigma_p = \sigma_r \wedge \sigma_q = \sigma_s$ and zero otherwise.

B. List of Alternative Ligands

The full list of structures considered as alternative ligands for the Eu^{3+} complexes is presented here.

Number	Name
1	9-hydroxy-1H-phenalen-1-one
2	quinoline-8-ol
3	3-oxo-1H-phenalene-2-formic acid
4	5-amino-9-hydroxy-1H-phenalen-1-one
5	9-amino-1H-phenalen-1-one
6	9-hydroxy-5-phenyl-1H-phenalen-1-one
7	9-hydroxy-5-(naphthalen-1-yl)-1H-phenalen-1-one
8	9-hydroxy-5-(phenylethynyl)-1H-phenalen-1-one
9	5-bromo-9-hydroxy-1H-phenalen-1-one
10	5-chloro-9-hydroxy-1H-phenalen-1-one
11	5-fluoro-9-hydroxy-1H-phenalen-1-one
12	9-hydroxy-5-iodo-1H-phenalen-1-one
13	9-hydroxy-5-methyl-1H-phenalen-1-one
14	9-hydroxy-2-methyl-1H-phenalen-1-one
15	9-hydroxy-5-nitro-1H-phenalen-1-one
16	5-(phenylsulphanyl)-9-hydroxy-1H-phenalen-1-one
17	9-amino-1H-phenalen-1-imin
18	5-(phenylsulphanyl)-9-amino-1H-phenalen-1-imin
19	tropolone
20	5,8-dihydroxy-naphthalene-1,4-dione
21	5-hydroxy-naphthalene-1,4-dione
22	5-hydroxy-4-azaphenanthrene
23	6'-hydroxy-2-azabiphenyl
24	2-hydroxypyridine
25	8-hydroxy-1-azanaphthaleneoxide
26	1-hydroxyanthraquinone
27	1,8-diazanaphthaleneoxide
28	2,2'-diazabiphenyloxide

29	1,2-diazacyclopentadienyl-2-azabenzeneoxide
30	1,3-dihydroxy-N-methyl-10-azaanthracen-9-one
31	1-hydroxy-N-methyl-10-azaanthracen-9-one
32	1-hydroxy-N,3-dimethyl-10-azaanthracen-9-one
33	1,8-dihydroxy-10-oxaanthracen-9-one
34	1-hydroxy-10-oxaanthracen-9-one
35	dithranol
36	6-hydroxy-7H-benzo[de]anthracen-7-one

C. Auxiliary Basis Sets – Composition

The explicit composition of the auxiliary basis sets (i.e. the number of functions with different orbital quantum numbers l) is presented in the following table.

Atom	Type of basis set	Composition
Ce	SVP	11s11p10d9f8g5h4i1k
	TZVP	12s12p11d9f8g6h5i1k
	TZVPP	12s12p11d9f8g6h5i4k
	QZVPP	13s13p12d10f9g7h6i5k4l
Pr	SVP	11s11p10d9f8g5h4i1k
	TZVP	12p11d9f8g6h5i1k
	TZVPP	12s12p11d9f8g6h5i4k
	QZVPP	13s13p12d10f9g7h6i5k4l
Nd	SVP	11s11p10d10f9g5h4i1k
	TZVP	12s12p11d10f9g7h5i1k
	TZVPP	12s12p11d10f9g6h5i4k
	QZVPP	13s13p13d11f10g8h6i5k4l
Pm	SVP	11s11p10d9f8g5h4i1k
	TZVP	12s12p11d9f8g6h5i1k
	TZVPP	12s12p11d9f8g6h5i4k
	QZVPP	13s13p12d10f9g7h6i5k4l
Sm	SVP	11s11p10d9f8g5h4i1k
	TZVP	12s12p11d9f8g6h5i1k
	TZVPP	12s12p11d9f8g6h5i4k
	QZVPP	13s13p12d10f9g7h6i5k4l
Eu	SVP	11s11p10d10f8g5h4i1k
	TZVP	12s12p11d10f8g6h5i1k
	TZVPP	12s12p11d9f8g6h5i4k
	QZVPP	13s13p12d10f9g7h6i5k4l
Gd	SVP	11s11p10d9f8g5h4i1k
	TZVP	12s12p11d10f9g6h5i1k
	TZVPP	12s12p11d10f9g6h5i4k

	QZVPP	13s13p13d11f10g8h6i5k4l
Tb	SVP	11s11p10d9f8g5h4i1k
	TZVP	12s12p11d9f8g6h5i1k
	TZVPP	12s12p11d9f8g6h5i4k
	QZVPP	13s13p12d10f9g7h6i5k4l
Dy	SVP	11s11p10d9f8g5h4i1k
	TZVP	12s12p11d9f8g6h5i1k
	TZVPP	12s12p11d9f8g6h5i4k
	QZVPP	13s13p12d10f9g7h6i5k4l
Ho	SVP	11s11p10d9f8g5h4i1k
	TZVP	12s12p11d9f8g6h5i1k
	TZVPP	12s12p11d9f8g6h5i4k
	QZVPP	13s13p12d10f9g7h6i5k4l
Er	SVP	11s11p10d9f8g5h4i1k
	TZVP	12s12p11d9f8g6h5i1k
	TZVPP	12s12p11d9f8g6h5i4k
	QZVPP	13s13p12d10f9g7h6i5k4l
Tm	SVP	11s11p10d9f8g5h4i1k
	TZVP	12s12p11d9f8g6h5i1k
	TZVPP	13s12p11d9f8g6h5i4k
	QZVPP	13s13p12d10f9g7h6i5k4l
Yb	SVP	11s11p10d9f8g5h4i1k
	TZVP	12s12p11d9f8g6h5i1k
	TZVPP	12s12p11d9f8g6h5i4k
	QZVPP	13s13p12d10f9g7h6i5k4l
Lu	SVP	11s11p11d10f8g8h5i1k
	TZVP	11s10p10d10f9g8h5i1k
	TZVPP	13s11p11d11f11g7h6i3k
	QZVPP	13s13p13d11f10g7h6i5k4l

D. Auxiliary Basis Sets – Molecular Test Set

Description of molecules in the test set is given in the following table.

Molecule	# unpaired electrons	Symmetry	Part of the test set of Ref. [133]?
$CeCl_3$	1	C_{3v}	no
CeF	1	C_{6v}	yes
CeF_2	2	C_{2v}	no
CeF_3	1	C_1	yes
CeF_4	0	T_d	no
CeH_2	2	C_{2v}	yes
CeO	2	C_{6v}	yes
Dy_2	12	C_1	no
$DyCl_3$	5	C_1	yes
DyF	5	C_{2v}	yes
DyF_2	6	C_{2v}	yes
DyF_3	5	C_1	no
DyF_4	6	C_1	no
DyH_2	4	C_1	no
DyO	6	C_1	no
Er_2	4	D_{6h}	no
ErCl	3	C_1	no
$ErCl_2$	2	C_{2v}	yes
$ErCl_3$	3	C_{3v}	no
ErF_3	1	C_1	yes
ErF_4	4	C_1	no
ErH_2	2	C_1	no
ErO	2	C_1	no
Eu_2	14	D_{6h}	yes
EuCl	8	C_{6v}	yes
$EuCl_3$	0	C_{3v}	no

EuF_2	7	C_{2v}	yes
EuF_3	0	C_s	no
EuF_4	1	T_d	no
EuH_2	7	C_{2v}	yes
EuO	7	C_{6v}	no
Gd_2	16	D_{6h}	yes
$GdCl_3$	7	C_{3v}	no
GdF	7	C_{6v}	yes
GdF_2	6	C_{2v}	yes
GdF_3	7	C_{3v}	yes
GdF_4	6	C_1	no
GdH_2	8	C_{2v}	yes
GdO	6	C_1	no
$HoCl_2$	3	C_{2v}	no
$HoCl_3$	4	C_1	no
HoF_3	4	C_s	yes
HoF_4	5	T_d	no
HoH_2	3	C_{2v}	no
HoO	5	C_{6v}	yes
Lu_2	2	D_{6h}	yes
Lu_2N	1	C_{2v}	yes
Lu_2O	0	C_{2v}	yes
$LuBr_3$	0	D_{3h}	yes
$LuCl_3$	0	D_{3h}	yes
LuF	0	C_{6v}	yes
LuF_2	1	C_{2v}	yes
LuF_3	0	C_{3v}	yes
LuF_4	1	T_d	no
LuH_2	1	C_{2v}	no
LuH_3	0	C_{3v}	yes
LuI_3	0	C_{3v}	yes
LuO	1	C_{6v}	no
NdCl	3	C_{6v}	yes
$NdCl_3$	2	C_{3v}	no
NdF_3	1	C_s	yes
NdF_4	1	T_d	no
NdH_2	4	C_{2v}	yes
NdO	4	C_{6v}	yes
$PmCl_3$	4	C_{3v}	no

PmF	4	C_{2v}	yes
PmF_2	5	C_{2v}	no
PmF_3	4	C_s	no
PmF_4	3	T_d	no
PmH_2	5	C_{2v}	yes
PmO	5	C_{2v}	yes
Pr_2	4	D_{6h}	no
PrCl	4	C_{2v}	yes
$PrCl_3$	2	C_1	no
PrF_2	3	C_1	no
PrF_3	0	C_s	yes
PrF_4	1	T_d	no
PrH_2	3	C_{2v}	yes
PrO	3	C_1	no
$SmCl_3$	1	C_{3v}	yes
SmF	7	C_{2v}	yes
SmF_2	6	C_{2v}	no
SmF_3	5	C_s	no
SmF_4	4	T_d	no
SmH_2	6	C_{2v}	yes
SmO	6	C_1	no
TbF	6	C_{6v}	yes
TbF_4	7	T_d	no
TmCl	2	C_{6v}	yes
$TmCl_3$	2	C_{3v}	no
TmF_2	1	C_{2v}	yes
TmF_3	2	C_1	no
TmF_4	3	T_d	no
TmH_2	1	C_{2v}	no
TmO	1	C_1	no
Yb_2	0	D_{6h}	yes
YbCl	1	C_{6v}	yes
$YbCl_2$	0	C_{2v}	no
$YbCl_3$	1	C_1	no
YbF_3	5	C_1	no
YbF_4	3	T_d	no
YbH_2	0	C_{2v}	yes
YbO	0	C_{6v}	no

E. Auxiliary Basis Sets – Individual ΔRI errors

Individual ΔRI errors in μE_h per atom for molecules in the test set are presented in the following table.

Molecule	def2-SVP	def2-TZVP	def2-TZVPP	def2-QZVPP
$CeCl_3$	55.81	5.58	21.27	1.43
CeF	62.51	29.38	39.95	3.93
CeF_2	21.93	18.51	19.68	1.05
CeF_3	21.64	16.84	20.27	0.82
CeF_4	28.18	18.41	24.75	0.94
CeH_2	66.93	70.44	46.04	6.47
CeO	99.60	33.86	53.21	10.32
Dy_2	160.21	277.80	250.31	169.86
$DyCl_3$	21.22	5.39	7.67	7.43
DyF	41.71	14.01	2.85	5.77
DyF_2	14.59	10.83	11.53	4.27
DyF_3	10.23	8.86	8.90	3.28
DyF_4	14.98	6.91	7.59	3.87
DyH_2	39.27	37.96	10.74	12.25
DyO	3.89	9.70	10.79	7.10
Er_2	20.30	22.69	26.77	0.09
ErCl	28.42	10.20	19.59	2.99
$ErCl_2$	29.37	0.86	16.29	0.07
$ErCl_3$	32.97	1.56	13.31	2.68
ErF_3	1.75	12.64	13.17	0.51
ErF_4	1.29	12.28	12.63	0.04
ErH_2	21.26	25.37	5.02	3.87
ErO	17.31	20.83	20.76	3.35
Eu_2	29.79	26.87	0.63	5.48
EuCl	83.85	90.92	68.32	30.44

$EuCl_3$	29.27	0.41	3.09	2.48
EuF_2	11.47	24.21	8.03	3.32
EuF_3	13.04	5.94	2.39	1.70
EuF_4	3.75	22.66	16.77	0.34
EuH_2	11.14	23.20	24.44	5.94
EuO	34.30	34.59	10.56	6.39
Gd_2	86.72	82.00	48.04	34.21
$GdCl_3$	35.64	5.27	8.10	0.93
GdF	6.59	12.07	1.90	2.01
GdF_2	12.62	16.73	8.02	3.13
GdF_3	1.64	15.69	8.88	2.43
GdF_4	0.74	13.94	8.19	2.33
GdH_2	17.71	21.03	12.34	2.19
GdO	25.56	18.04	4.54	5.06
$HoCl_2$	27.53	3.24	12.60	2.51
$HoCl_3$	32.75	2.24	11.70	3.00
HoF_3	1.06	14.34	11.39	0.34
HoF_4	2.34	17.75	15.04	1.04
HoH_2	17.69	32.16	19.87	6.93
HoO	30.86	32.21	21.09	1.61
Lu_2	46.48	51.03	74.47	79.05
Lu_2N	33.84	22.72	27.29	14.50
Lu_2O	1.28	10.69	9.12	2.55
$LuBr_3$	13.59	23.62	26.19	8.81
$LuCl_3$	28.31	3.60	9.97	3.03
LuF	4.93	11.23	15.94	9.67
LuF_2	2.92	15.88	15.84	7.59
LuF_3	1.57	13.26	12.61	5.40
LuF_4	12.22	27.38	27.22	4.74
LuH_2	9.12	1.99	5.37	4.33
LuH_3	25.74	12.60	0.12	3.45
LuI_3	33.54	0.70	4.16	8.88
LuO	5.63	18.32	17.85	11.53
NdCl	61.36	26.88	60.21	72.40
$NdCl_3$	29.87	2.19	6.05	0.02
NdF_3	0.12	8.84	7.64	1.53
NdF_4	16.31	24.09	20.88	2.36
NdH_2	3.74	17.39	11.35	4.57
NdO	67.53	20.54	9.11	8.13

$PmCl_3$	34.72	3.92	10.14	1.55
PmF	8.23	20.16	11.08	2.40
PmF_2	2.30	23.47	10.89	1.07
PmF_3	2.06	16.43	9.65	0.10
PmF_4	2.80	15.79	10.25	0.59
PmH_2	19.92	32.38	14.40	5.93
PmO	35.57	32.30	11.60	2.79
Pr_2	23.64	1.85	18.70	28.35
PrCl	58.98	32.58	38.99	19.44
$PrCl_3$	47.02	3.10	22.79	1.00
PrF_2	12.65	15.57	22.60	1.19
PrF_3	6.02	11.43	18.53	1.39
PrF_4	20.14	15.84	24.70	0.87
PrH_2	8.05	23.48	0.05	5.30
PrO	36.61	13.92	23.66	0.88
$SmCl_3$	33.14	1.17	8.81	2.28
SmF	50.92	90.00	65.39	53.71
SmF_2	10.18	24.11	11.85	1.91
SmF_3	0.76	17.07	9.68	0.75
SmF_4	7.48	18.91	9.39	0.72
SmH_2	30.52	20.11	6.52	0.49
SmO	30.74	26.07	11.97	2.98
TbF	47.30	10.07	22.32	10.00
TbF_4	17.02	4.74	1.94	2.15
TmCl	40.51	10.95	19.04	7.26
$TmCl_3$	40.14	1.82	13.03	0.81
TmF_2	8.68	17.28	15.63	4.77
TmF_3	5.13	11.79	12.24	2.13
TmF_4	6.19	10.88	10.70	0.77
TmH_2	17.54	38.59	20.70	1.01
TmO	28.31	19.55	20.13	6.59
Yb_2	43.75	37.07	41.45	16.82
YbCl	40.52	12.33	19.50	6.43
$YbCl_2$	35.89	1.09	14.73	2.08
$YbCl_3$	38.01	2.25	9.87	0.76
YbF_3	4.25	12.14	9.62	2.66
YbF_4	14.50	13.95	8.42	0.75
YbH_2	16.94	38.29	21.31	1.40
YbO	27.28	20.37	22.77	6.82

F. Auxiliary Basis Sets – Atomization Energies

Individual RI errors in the atomization energies ΔE_{at} in cm^{-1} per atom for molecules in the test set are presented in the following table.

Molecule	def2-SVP	def2-TZVP	def2-TZVPP	def2-QZVPP
$CeCl_3$	-14	-5	-6	-2
CeF	-22	-8	-12	-4
CeF_2	-14	-5	-7	-2
CeF_3	-15	-4	-6	-2
CeF_4	-17	-5	-7	-2
CeH_2	14	15	8	0
CeO	-31	-9	-16	-5
Dy_2	-36	-60	-56	-43
$DyCl_3$	-5	-2	-2	-1
DyF	2	-3	0	-2
DyF_2	-5	-2	-3	-1
DyF_3	-7	-2	-3	-1
DyF_4	-7	-2	-2	-1
DyH_2	8	9	2	1
DyO	-7	-2	-4	-1
Er_2	-3	-4	-2	0
ErCl	-6	-4	-3	-1
$ErCl_2$	-6	-3	-2	-1
$ErCl_3$	-7	-3	-2	0
ErF_3	-9	-3	-2	-1
ErF_4	-10	-3	-2	-1
ErH_2	5	6	2	1
ErO	-10	-5	-4	-1
Eu_2	2	1	0	0
EuCl	-14	-19	-15	-8

$EuCl_3$	-5	-2	1	0
EuF_2	-8	-3	-2	-1
EuF_3	-4	0	0	0
EuF_4	-9	-4	-4	-1
EuH_2	5	7	5	1
EuO	-10	-5	-3	-2
Gd_2	-13	-15	-13	-7
$GdCl_3$	-7	-4	-3	-1
GdF	-2	-1	-1	-1
GdF_2	-9	-3	-3	-1
GdF_3	-8	-3	-3	-1
GdF_4	-9	-3	-3	-1
GdH_2	6	6	2	1
GdO	-10	-3	-3	-1
$HoCl_2$	-6	-2	-2	-1
$HoCl_3$	-7	-3	-2	-1
HoF_3	-9	-2	-2	-1
HoF_4	-9	-3	-3	-1
HoH_2	5	9	5	1
HoO	-13	-5	-4	-2
Lu_2	-6	-7	-9	-12
Lu_2N	-7	-2	-1	0
Lu_2O	-2	0	2	3
$LuBr_3$	-2	-2	-1	0
$LuCl_3$	-6	-3	0	0
LuF	-5	0	0	0
LuF_2	-8	-2	-1	0
LuF_3	-8	-2	-1	0
LuF_4	-12	-5	-5	0
LuH_2	3	2	1	1
LuH_3	8	5	4	2
LuI_3	-3	-1	-1	0
LuO	-6	-2	-1	0
NdCl	-11	-8	-13	-17
$NdCl_3$	-6	-3	-1	-1
NdF_3	-8	-2	-2	-1
NdF_4	-13	-5	-5	-1
NdH_2	3	4	3	0
NdO	-19	-5	-2	-3

$PmCl_3$	-8	-5	-3	-2
PmF	-9	-5	-4	-3
PmF_2	-9	-6	-4	-2
PmF_3	-10	-4	-3	-2
PmF_4	-11	-4	-3	-2
PmH_2	4	7	2	0
PmO	-15	-9	-5	-3
Pr_2	-10	-3	-8	1
PrCl	-15	-11	-11	-7
$PrCl_3$	-12	-5	-6	-2
PrF_2	-13	-4	-7	-2
PrF_3	-12	-3	-5	-1
PrF_4	-15	-4	-7	-2
PrH_2	0	4	-1	-1
PrO	-17	-5	-8	-2
$SmCl_3$	-8	-3	-3	-1
SmF	-17	-20	-17	-14
SmF_2	-10	-5	-4	-2
SmF_3	-9	-4	-3	-2
SmF_4	-11	-4	-3	-1
SmH_2	7	5	0	-1
SmO	-13	-6	-5	-3
TbF	4	-3	2	-2
TbF_4	-6	-2	-2	-2
TmCl	-7	-4	-3	-2
$TmCl_3$	-8	-3	-2	0
TmF_2	-9	-4	-3	-1
TmF_3	-9	-3	-2	-1
TmF_4	-10	-2	-2	0
TmH_2	5	9	5	0
TmO	-11	-5	-4	-1
Yb_2	-4	-5	-4	-2
YbCl	-7	-3	-2	-1
$YbCl_2$	-7	-2	-2	-1
$YbCl_3$	-8	-2	-1	0
YbF_3	-9	-2	-1	-1
YbF_4	-12	-3	-1	0
YbH_2	5	10	6	1
YbO	-10	-3	-3	-1

G. Auxiliary Basis Sets – Performance with Large ECPs

Individual ΔRI errors in μE_h per atom for large core ECPs of type X(III) are presented in the following table. Note that the computation for $LuCl_3$ was done in C_{3v} symmetry.

Molecule	def2-SVP	def2-TZVP	def2-TZVPP	def2-QZVPP
$CeCl_3$	2.19	8.88	2.19	3.30
CeF_3	7.12	9.23	8.01	2.28
$DyCl_3$	9.32	7.47	1.10	2.45
DyF_3	1.49	10.83	10.74	2.34
$ErCl_3$	1.29	8.94	1.35	3.15
ErF_3	1.95	10.22	10.28	2.41
$EuCl_3$	0.10	6.99	2.33	3.11
EuF_3	0.26	10.03	11.89	2.45
$GdCl_3$	3.31	6.39	1.86	2.03
GdF_3	0.59	8.66	8.72	1.54
$HoCl_3$	9.80	6.71	0.74	2.46
HoF_3	1.36	9.92	10.54	2.33
$LuCl_3$	2.06	6.78	3.13	1.73
LuF_3	1.71	10.03	9.66	1.89
$NdCl_3$	1.12	7.22	2.31	2.13
NdF_3	1.95	9.95	9.89	1.85
$PmCl_3$	0.48	9.66	2.62	3.53
PmF_3	0.20	10.58	11.33	2.48
$PrCl_3$	11.61	7.46	1.31	2.21
PrF_3	3.97	9.80	8.39	2.37
$SmCl_3$	0.76	9.32	2.08	3.36
SmF_3	1.84	10.98	11.58	2.52
$TmCl_3$	1.15	8.72	0.64	2.99
TmF_3	1.55	10.49	10.26	2.30
$YbCl_3$	10.73	7.53	2.37	2.10

YbF_3	0.21	10.61	10.54	2.28

Individual ΔRI errors in μE_h per atom for large core ECPs of type X(II) are presented in the following table.

Molecule	def2-SVP	def2-TZVP	def2-TZVPP	def2-QZVPP
CeF_2	3.02	6.20	6.25	1.50
CeO	29.71	5.32	3.05	12.14
DyF_2	0.80	4.04	3.91	0.91
DyO	7.43	1.16	3.92	12.57
$ErCl_2$	1.90	6.13	1.47	1.98
ErO	1.41	1.64	0.12	12.42
EuF_2	1.53	4.64	5.02	0.94
EuO	0.59	0.36	7.65	8.75
GdF_2	1.62	4.35	4.24	0.77
GdO	7.95	0.03	0.65	3.77
$HoCl_2$	2.29	5.76	1.44	2.08
HoO	4.98	3.36	4.86	12.94
NdO	4.33	4.63	1.48	4.09
PmF_2	2.49	4.93	5.02	1.01
PmO	7.52	2.51	3.97	10.71
PrF_2	2.80	5.72	5.64	1.32
PrO	17.76	4.76	6.72	11.19
SmF_2	1.36	4.43	4.53	0.89
SmO	3.95	1.13	2.68	9.47
TmF_2	0.47	3.81	3.63	0.77
TmO	1.57	3.56	1.77	9.96
$YbCl_2$	1.56	5.97	1.06	1.86
YbO	5.60	3.55	1.83	9.95

List of Publications

2016 J.-F. Greisch, **J. Chmela**, M. E. Harding, W. Klopper, M. M. Kappes, and D. Schooss, *Inorg. Chem.* 55 (2016) 3316.

2016 **J. Chmela**, M. E. Harding, D. Matioszek, C. E. Anson, F. Breher, and W. Klopper, *ChemPhysChem*, 17 (2016) 37.

2012 D. Hollas, O. Svoboda, **J. Chmela**, and P. Slavíček, *Chem. Listy* 106 (2012) 936.

Acknowledgments

There are many people that have helped me on my way to finishing this thesis and I would like to thank them.
First of all I would like to thank Wim Klopper for giving me the opportunity to do my PhD under his guidance. I thank for the trust he gave me and for always having time for me when I had questions.
I thank Florian Weigend not only for many fun Kicker games but also for agreeing to being Korreferent of this thesis.
I would like to express my immense gratitude to Michael Harding who was an excellent supervisor to me, from whom I have learned much, who was always ready to help me with any problems I had, and whose many helpful suggestions improved this thesis greatly. Also thank you for never letting me feel stupid (even when, objectively, some of my questions were stupid at some point).
I would like to thank Jean-François Greisch for unproblematic collaboration and insight he gave me into the experimental part of our common work.
I would also like to thank my colleagues for creating a friendly and relaxed atmosphere in the working group. I would like to thank specifically (in Paweł's words) the 'Kickersquad' – Patrik Pollak, Sandra Ahnen, Qiang Li, Peter Limacher, and Paweł Panek for many great times we spent together doing 'Sport'.
I would like to thank my officemates for a nice atmosphere in the office – to Katharina Krause for being very helpful with many things of scientific and everyday life and for helping me settle down in a new country, and to Johannes Heuser for always reminding me what is (and what is not) important in life.
I would also like to thank Lies Broeckaert for being an understanding and patient flatmate and friend.
A big thanks belongs to Daniel Hollas for his thorough reading and insightful comments and suggestions to this thesis.
At this point I would also like to thank my former teachers that have helped me through the

years. Of many of them I would like to explicitly thank Jana Kudrnová and Petr Slavíček. Their enthusiasm inspired me to study chemistry and theoretical chemistry, respectively.
I also want to thank all my friends for support and especially my homies – Jan Chalupa, Radek Drápela, Martin Hodula, Ondřej Hora, Jakub Koktan, Vít Michel, and Jan Šimeček. It has been a long time since we graduated from high school and I am happy to still be included in the group even when I live abroad.
I thank my parents and my sister as well as all the rest of my family. They have always supported me and they have always had faith in me. I could not be where I am now without them.
Finally I would like to thank Kristina Geistert. Thank you for your constant support. Thank you for being the person that you are. *Hanta-tyë, Undómiel.*

Thank you.